

marine technology SOCIETY **Journal**

The International, Interdisciplinary Society Devoted to Ocean and Marine Engineering, Science, and Policy

Volume 50 Number 2 March/April 2016

General Issue



Featuring Expanded Papers from OCEANS '15 MTS/IEEE Conference

Marine Technology Society Officers

BOARD OF DIRECTORS

President
Ray Toll
Old Dominion University
President-elect
Donna Kocak
HARRIS Corporation
Immediate Past President
Drew Michel
ROV Technologies, Inc.
VP—Section Affairs
Doug Wilson
Caribbean Wind LLC
VP—Education and Research
Liesl Hotaling
COSEE
VP—Industry and Technology
Dr. Andrew M. Clark, P.E.
CypSeisNet, Inc.
VP—Publications
Dr. Erika Montague
OceanGate, Inc.
Treasurer and VP—Budget and Finance
Mike Pinto
MBARI (Ret.)
VP—Government and Public Affairs
Justin Manley
Teledyne Benthos

SECTIONS

Canadian Maritime
Vacant
Florida
Erica Moulton
St. Pete Makers
Great Lakes
Hans Van Sumeren
Northwestern Michigan College
Gulf Coast
John Cousins
General Dynamics Information Technology
Hampton Roads
Jim Haluska
Old Dominion University
Hawaii
Alan Hilton
Center of Excellence for Research in
Ocean Sciences (CEROS)
Houston
Terry Dahlke
Geospace Offshore
India
Dr.R.Venkatesan
National Institute of Ocean Technology
Japan
Hideyuki Suzuki
University of Tokyo
Monterey Bay
Jill Zande
MATE Center
New England
Rhonda Moniz
SeaBotix
Norway
TBD
Newfoundland and Labrador
Darrell O'Neill
Dept. of Innovation, Trade, and Rural Development
Oregon
Jeremy Childress
Oregon State University
College of Oceanic & Atmospheric Sciences
Puget Sound
Fritz Stahr
University of Washington
San Diego
Alan Kenny
Teledyne RD Instruments

South Korea
Prof. B.G. Lee
Maritime & Ocean Engineering Research Inst.
(MOERI/KORDI)
Washington, D.C.
Jake Sabin
Kongsberg

PROFESSIONAL COMMITTEES

Industry and Technology
Buoy Technology
Rick Cole
RDSEA International, Inc.
Cables and Connectors
Jennifer Snyder
SAIC
Deepwater Field Development Technology
Dr. Benton Baugh
Radoil, Inc.
Diving
Michael Lombardi
Ocean Opportunity
Michael Max
Hydrate Energy International LLC
Dynamic Positioning
Pete Fougerie
Portsmouth, NH
Manned Underwater Vehicles
William Kohnen
HYDROSPACE Group
Moorings
Jack Rowley
SAIC
Oceanographic Instrumentation
Dr. Carol Janzen
Sea-Bird Electronics, Inc.
Offshore Structures
Dr. Peter W. Marshall
MHP Systems Engineering
Remotely Operated Vehicles
Chuck Richards
C.A. Richards and Associates, Inc.
Ropes and Tension Members
Evan Zimmerman
Delmar Systems, Inc.
Seafloor Engineering
Craig Etka
Scorpio Ventures, LLC
Underwater Imaging
Dr. Fraser Dalgleish
Harbor Branch Oceanographic Institute
Unmanned Maritime Vehicles
Rafael Mandujano
Vehicle Control Technologies, Inc.

Education and Research
Marine Archaeology
Dr. Stephen Wood
Florida Institute of Technology
Marine Education
Erica Moulton
MATE Center
Marine Geodetic Information Systems
Dave Zilkoski
NOAA
Marine Materials
Dr. R. Venkatesan
National Institute of Ocean Technology
Ocean Exploration
Erika Montague
OceanGate, Inc.
Physical Oceanography/Meteorology
Dr. Richard L. Crout
Naval Research Laboratory
Remote Sensing
Ryan Vandermeulen
University of Southern Mississippi

Government and Public Affairs

Arctic Technology
Basel Abdalla
Wood Group Kenny
Marine Law and Policy
Bill Glenn
Royston Rayzor Vickery & Williams LLP
Marine Mineral Resources
Alex Barnard
Marine Security
Dallas Meggitt
Sound & Sea Technology
Ocean Economic Potential
Vacant
Ocean Observing Systems
Vembu Subramanian
SECOORA
Ian Walsh
WET Labs
Ocean Pollution
Ryan Morton
Anadarko Petroleum
Renewable Energy
Maggie L. Merrill
Marine Marketing Services and New England
MREC at UMass Dartmouth
Kenneth Baldwin
University of New Hampshire

STUDENT SECTIONS

Alpena Community College
Arizona State University
College of William & Mary
Dalhousie University
Duke University
Florida Atlantic University
Florida Institute of Technology
Long Beach City College
Marine Institute of Newfoundland and Labrador
Massachusetts Institute of Technology
Memorial University (MUN)
Monterey Peninsula College/Hartnell College
North Carolina State University
Oregon State University
Rutgers University
Stockton University
Texas A&M University—College Station
Texas A&M—Corpus Christi
Texas A&M University—Galveston
United States Naval Academy
University of Florida
University of Hawaii
University of Houston
University of North Carolina—Charlotte
University of Puerto Rico, Mayagüez
University of Southern Mississippi
University of Washington
Webb Institute

HONORARY MEMBERS (†deceased)

†Robert B. Abel
†Charles H. Bussmann
†John C. Calhoun, Jr.
John P. Craven
†Paul M. Fye
David S. Potter
†Athelstan Spilhaus
†E. C. Stephan
†Allyn C. Vine
†James H. Wakelin, Jr.



Cover Images: Front: Randeni et al., Figure 2a (in this issue). Back (top to bottom): A Spray Glider under the surface about to embark on a 2-month mission off the West Florida Shelf (Photo credit: Brian Cousin/Harbor Branch Oceanographic Institute); Randeni et al., Figures 3c and 1b (in this issue); Cai et al., Figure 2a (this issue).



Text: SPI
Cover and Graphics:
Michele A. Danoff, Graphics By Design

The Marine Technology Society Journal
(ISSN 0025-3324) is published by the Marine Technology Society, Inc., 1100 H Street NW, Suite LL-100 Washington, DC 20005

Annual Subscription Prices (all prices include shipping): **Online access to the MTS Journal** (including 14 years of archives) is FREE for MTS members. Members can purchase the **printed Journal** for \$38 domestic, \$55 Canada, and \$125 international. Non-members and library subscriptions are: **Online only** (including 14 years of archives): \$465; **Online and print** (including 14 years of archives): \$499; **Print only**: \$155 domestic, \$175 Canada, and \$250 international. Single-issue (hardcopy) price is \$18 for members and \$20 for nonmembers, plus \$7 domestic shipping or \$14 international shipping for all single-issue orders. Pay-per-view (worldwide): \$28/article. Postage for periodicals is paid at Washington, DC and additional mailing offices.

POSTMASTER:
Please send address changes to:

Marine Technology Society Journal
1100 H Street NW, Suite LL-100
Washington, DC 20005
Tel: (202) 717-8705; Fax: (202) 347-4302

Copyright © 2016 Marine Technology Society, Inc.

marine technology SOCIETY Journal

Volume 50, Number 2, March/April 2016

General Issue

In This Issue

3

Message From the MTS Journal Editor
Anni Vuorenkoski Dalgleish

5

Rendezvous Point Technique for Multivehicle Mine Countermeasure Operations in Communication-Constrained Environments
Veronika Yordanova, Hugh Griffiths

17

Autonomous Underwater Vehicle Motion Response: A Nonacoustic Tool for Blue Water Navigation
Supun A. T. Randeni P.,
Alexander L. Forrest, Remo Cossu,
Zhi Quan Leong, Peter D. King,
Dev Ranmuthugala

27

Coupled Modeling of Hydrodynamics and Sound in Coastal Ocean for Renewable Ocean Energy Development
Wen Long, Zhaoqing Yang,
Andrea Copping, Z. Daniel Deng

37

Development and Application of a New Mobile pH Calibrator for Real-Time Monitoring of pH in Diffuse Flow Hydrothermal Vent Fluids
Chunyang Tan, Kang Ding,
William E Seyfried, Jr

48

Micro-Modem for Short-Range Underwater Mobile Communication Systems
Jun-Ho Jeon, Sung-Joon Park

54

Characteristics of Microstructure Turbulence Measurements With a Moored Instrument in the South China Sea
Xin Luan, Xiuyan Liu, Hua Yang,
Shuxin Wang, Guojia Hou, Dalei Song

63

Study and Design of a Heat Dissipation System in a Junction Box for Chinese Experimental Ocean Observatory Network
Dejun Li, Jun Wang, Jianshe Feng,
Canjun Yang, Yanhu Chen

75

Study of a Novel Underwater Cable With Whole Cable Monitoring
Jiawang Chen, Chunying Xu, Ying Chen,
Jian Ji, Dongxu Yan

83

Effect of Low Temperature and High Pressure on Deep-Sea Oil-Filled Brushless DC Motors
Minjian Cai, Shijun Wu, Canjun Yang

Editorial Board

Anni Vuorenkoski Dalgleish, Ph.D.
Editor
Harbor Branch Oceanographic
Institute at Florida Atlantic University

Ann E. Jochens, Ph.D.
Texas A&M University

Donna Kocak
HARRIS Corporation

Scott Kraus, Ph.D.
New England Aquarium

Dhugal Lindsay, Ph.D.
Japan Agency for Marine-Earth Science
& Technology

Eugene Masson
Monterey Bay Aquarium Research Institute

Ralph Rayner, Ph.D.
BMT Limited

Brock Rosenthal
Ocean Innovations

Editorial

Erika Montague, Ph.D.
VP of Publications

Anni Vuorenkoski Dalgleish, Ph.D.
Editor

Amy Morgante
Managing Editor

Administration

Ray Toll
President

Ms. Chris Barrett
Interim Executive Director

Josh Cohen
Member Groups and
Outreach Manager

Jeanne Glover
Membership Manager

Suzanne Voelker
Program Administrator

The Marine Technology Society is a not-for-profit, international professional society. Established in 1963, the Society's mission is to promote the exchange of information in ocean and marine engineering, technology, science, and policy.

Please send all correspondence to:
The Marine Technology Society
1100 H Street NW, Suite LL-100
Washington, DC 20005
(202) 717-8705 Tel.
(202) 347-4302 Fax
MTS Journal: morganteditorial@verizon.net
Publications: publications@mtsociety.org
Membership: Jeanne.Glover@mtsociety.org
Programs: Josh.Cohen@mtsociety.org
Director: chris.barrett@mtsociety.org
Subscriptions: suzanne.voelker@mtsociety.org
Online: www.mtsociety.org

MEMBERSHIP INFORMATION

may be obtained by contacting the Marine Technology Society. Benefits include:

- Free subscription to the online *Marine Technology Society Journal*, with highly reduced rates for the paper version
- Free subscription to the bimonthly newsletter, *Currents*, covering events, business news, science and technology, and people in marine technology
- Member discounts on all MTS publications
- Reduced registration rates to all MTS and MTS-sponsored conferences and workshops
- Member-only access to an expansive Job Bank and Member Directory
- Reduced advertising rates in MTS publications
- National recognition through our Awards Program

Individual dues are \$75 per year. Life membership is available for a one-time fee of \$1,000. Patron, Student, Emeritus, Institutional, Business, and Corporate memberships are also available.

ADVERTISING

Advertising is accepted by the *Marine Technology Society Journal*. For more information on MTS advertising and policy, please contact mtsoffice@mtsociety.org

COPYRIGHT

Copyright © 2016 by the Marine Technology Society, Inc. Authorization to photocopy items for internal or personal use, or the internal or personal use of specific clients, is granted by the Marine Technology Society, provided that the base fee of \$1.00 per copy, plus .20 per page is paid directly to Copyright Clearance Center, 222 Rosewood Dr., Danvers, MA 01923.

For those organizations that have been granted a photocopy license by CCC, a separate system of payment has been arranged. The fee code for users of the Transactional Reporting Service is 0025-3324/89 \$1.00 + .20. Papers by U.S Government employees are declared works of the U.S. Government and are therefore in the public domain.

The Marine Technology Society cannot be held responsible for the opinions given and the statements made in any of the articles published.

ABSTRACTS

MTS Journal article abstracts, if available, can be accessed for free at <http://www.ingentaconnect.com/content/mts/mtsj>.

Print and electronic abstracts of *MTS Journal* articles are also available through *GeoRef* <<http://www.agiweb.org/georef/>>, *Aquatic Sciences and Fisheries Abstracts*, published by Cambridge Scientific Abstracts <<http://www.csa.com/factsheets/aquacult-set-c.php>>, and *Geobase's Oceanbase* published by Elsevier Science.

CONTRIBUTORS

Contributors can obtain an information and style sheet by contacting the managing editor. Submissions that are relevant to the concerns of the Society are welcome. All papers are subjected to a stringent review procedure directed by the editor and the editorial board. The *Journal* focuses on technical material that may not otherwise be available, and thus technical papers and notes that have not been published previously are given priority. General commentaries are also accepted and are subject to review and approval by the editorial board.

Message From the *MTS Journal* Editor

Anni Vuorenkoski Dagleish

This issue of *Marine Technology Society Journal* includes three papers featuring research presented at the OCEANS '15 MTS/IEEE conference held on October 19–22, 2015, in Washington, DC. In addition, six papers in this issue describe recent advances covering a range of core general topics in the field of marine technology, including papers describing contributions to advances in ocean sensing technology, underwater communications systems, and underwater platforms, as well as technology related to fixed and floating offshore structures.

In their paper, Yordanova and Griffiths address a number of challenges related to strategies of using autonomous underwater vehicles (AUVs) for mine counter measure (MCM) applications. The authors provide an overview of methods currently used for searching, detecting, classifying, and identifying marine mines, and propose a novel, more efficient approach utilizing an adaptive network of AUVs. The paper proposes a novel multivehicle path planning architecture resulting in reduction in mission time and cost by optimizing vehicle task allocation and by adaptive scheduling of rendezvous points. The underwater environment poses significant challenges for implementing a dynamic strategy for a network of deterministically maneuvering vehicles; the authors include discussion on the limited range and bandwidth of free-space underwater communication systems and also on the limited ability to coordinate and configure positions. The simulation results presented in this paper pave a way for further explorations into beneficial usage of networked AUVs, and although the method is particularly discussed in the context of MCM missions, it can be modified and applied for other marine sectors.

AUVs are also the topic of Randeni et al. in their paper, which also is an expanded study based on the authors' OCEANS '15 presentation. The paper proposes a potential solution to a well-known and documented problem related to AUV navigation systems. The authors provide results from recent field experiments demonstrating and assessing the performance of a novel nonacoustic method to resolve the near-field flow velocity components around an AUV. In another expanded OCEANS '15 paper, Long et al. present a theoretical analysis of the sound propagation from a marine hydrokinetic (MHK) device. The method is coupled with the Finite Volume Community Ocean Model with the objective of studying MHK-induced acoustic pressure fields, which may potentially interfere with marine mammal communication.

In situ measurement of pH is essential in geochemical analysis of seawater and is the topic of the paper by Tan et al. The authors present a new mobile pH calibrator (MpHC), which was deployed on the DSRV *Alvin* to make in situ pH measurements at hydrothermal vents on

the Juan de Fuca Ridge. The paper by Jeon and Park describes the design and implementation of a micro modem for mobile underwater acoustic communications systems, where the modem could be integrated to a small mobile node such as a biomimetic fish robot. Luan et al. obtained long-term ocean turbulence measurements in the South China Sea with a moored instrument. Authors present the experimental data and processing methods to analyze the effects of a turbulence field on the platform stability, tracking flexibility, and microscale shear spectra. In another contribution, Li et al. report the results from a theoretical heat dissipation simulation and experimental study to assess the performance of a novel cooling system design for a junction box in a seafloor observatory network. Also in this issue, Chen et al. propose a low-cost method for underwater cable detection based on flexible sensors, whereas Cai et al. describe an application and verification method of a deep-sea DC motor to verify the motor's power loss and performance under low temperature and extreme pressure.

The Editorial Board would like to thank Jake Sabin for contributing to this issue by soliciting expanded papers from OCEANS '15 presenting authors. The Editorial Board would also like to thank all MTS members who have contributed to the *MTS Journal* by submitting manuscripts and serving as Guest Editors or reviewers. As always, the Board encourages the MTS community to continue submitting manuscripts and proposals for future Special Editions.

Rendezvous Point Technique for Multivehicle Mine Countermeasure Operations in Communication-Constrained Environments

AUTHORS

Veronika Yordanova

Hugh Griffiths

University College London

Introduction

There has been increased interest in the last decade in using autonomous underwater vehicles (AUVs) in a network configuration. However, the inability to maintain robust communication continuously is a major constraint for the development of such technology. Radio frequency and optical signals do not propagate well underwater, and therefore, acoustic transmissions are the most common choice. However, there are severe limitations in range and bandwidth of the acoustic communication, and the network operation must take this into account (Akyildiz et al., 2005).

The approach we propose is based on assigning dynamically a sequence of rendezvous points (RPs) throughout the mission, a location and time where all agents in the network agree to meet and the vehicles can exchange information. This way a complete lack of connection can be assumed outside of the RP perimeter, thus providing a means for the system to operate under severe channel conditions. The work we present applies mainly to mine countermeasures (MCMs). This paper presents the idea of applying RP to MCM by proposing adaptive RP scheduling. The overall goal of this new approach is to enable an adaptive reallocation of sys-

ABSTRACT

Advantages of using a multivehicle network over a single autonomous underwater vehicle platform include extended coverage area, potential cost and time efficiency, and more robust performance. A common issue that slows advancement in the field is the limited available communication between the platforms. The approach we propose is based on assigning a sequence of rendezvous points (RPs) where the vehicles can meet and exchange information. The work we present in this paper applies principally to mine countermeasure and suggests that, despite the disadvantage of time to allow for the vehicles to reach the RPs, there are techniques that can minimize the losses and provide advantages such as easier coordination and access points for operator monitoring and system modifications. The results we present in this paper give an estimate of the reduction in loss if such an approach is employed. We make a comparison between the RP and a benchmark case by analyzing numerical simulations.

Keywords: rendezvous, multivehicle, mine countermeasures

tem resources to maximize search area while making explicit the rule of revisiting all contacts on the way.

The remainder of the paper is organized as follows: Section 2 gives details on different types of MCMs; Section 3 focuses on relevant work published recently on underwater networks and autonomy; Section 4 gives an overview of the RP idea; Section 5 explains the methodologies adopted for evaluating the RP method and analyzing the suitable conditions for application; Section 6 shows simulation results; Section 7 presents the analysis and limitations of the approach. The last section concludes the work and suggests future directions.

Evolution of MCM Systems

The Korean and Gulf wars are examples where effective mine warfare was

applied. Warships were damaged and amphibious assaults aborted due to the inability of the navies to counter this asymmetric threat. Currently, the sheer number of existing naval mines is another reason to treat the problem as a challenging and diverse task: it is estimated that a million mines, of more than 300 types, are stored by 60 navies worldwide (this excludes U.S. weapons); mine production exists in more than 30 countries, and export is done by more than 20. These figures do not account for improvised explosive devices, which are considered affordable and relatively easy to make (Truver, 2012). The MCM problem arises from the difficulty of distinguishing between the real mines and the false alarms (FAs) due to mine-like seafloor objects (Sariel, Balch, & Erdogan, 2008), as well as from inefficient means of clearing them.

Due to the large diversity of mine types, their actuation mechanisms and means of deployment, it is hard to identify a single best method to deal with the problem of minefields. Currently, the conventional MCM approaches are sweeping and hunting. Minesweeping is used for removing mines by causing their detonation or capturing them. The design of the minesweeping vessel should be stealthy such that it does not trigger the mine itself, but instead the explosion occurs at a safe distance where the towed body with the triggering mechanism is. Minesweepers can also capture the chain or cable of moored mines, which was the predominant mine type until WWI, but not that common presently. The disadvantage of using such a sweeping technique is that there can be no assurance that the area is clear of mines. The other commonly employed technique, mine hunting, involves prior detection and classification before any neutralization action is taken. This brings the advantage of providing a probabilistic evaluation of the threat level of the area. The sensor used to detect mines is sonar, and the acquired imagery is processed by human operators to classify any contacts that could be actual mines. Once a decision is made, the object can be neutralized.

However, some countermeasures are becoming obsolete with the advancement of mine technology, and new solutions are being sought.

In minesweeping, the acoustic and magnetic vessel signature that would actuate a mine is mimicked by the minesweeper vessel in an attempt to trigger it prematurely. This is becoming less effective as modern mines rely on multiple signatures, which are not always possible to simulate all together (Truver, 2012). On the other hand, even if we disregard for a moment the complicated multiple triggering mecha-

nism, the sweeping method does not result in any certainty that an area is mine free (Cornish, 2003). There is the possibility that a mine did not activate even though it detected a suitable target. The actuation mechanism sometimes involves randomized control that selects a target from a sequence of detections in order to avoid multiple mines being triggered by the same contact or hit only the first vessel from a convoy.

Mine hunting is considered more reliable than sweeping as at the end of the mission a level of confidence can be reached that can be input to a decision-making process on whether to drive a ship or convoy through an area (Cao & Bell, 1999). The process includes a detection, classification, and identification stage performed using imagery from sonar towed by a ship. Once a certain target is located, a neutralization unit, usually a remotely operated vehicle (ROV), is sent to dispose of it. However, there are some issues with traditional mine hunting techniques. Mine hunting ships require design with a minimal vessel signature so that it does not trigger the mines in its vicinity (Schwarz, 2014). The bigger issue that remains is that no matter how stealthy the ship is, there still needs to be people on board to control the mission. An alternative is to use a remotely operated vessel that is controlled from a safe base on the shore. While this is technology that is advancing (Benjamin & Curcio, 2004), there is still the issue of the sonar not being able to explore the contacts from close proximity. The method also relies on a single sensor that makes repeated scans over the area, which might require long mission times. The interest in using AUVs for mine hunting has been increasing in the last decade, due to cumulative work in multiple relevant fields to allow collaboration between vehicles

and lowering the price of commercial hardware. Recent advances that have contributed to the area include work in communication, navigation, localization, mapping, vehicle design, underwater swarms, autonomy (surface and underwater), networking, international experiments with defense and scientific applications, etc. (Kalwa et al., 2015; Dugelay et al., 2015).

Another reason to adopt autonomous vehicles for MCM applications is that there are still some unconventional methods in use, such as sending divers or mammals to perform the neutralization and search phases. Although not that common, these techniques do exist. Mine neutralization methods conducted by human divers remain the most reliable. Mammals have more endurance and could be trained for MCM purposes, and there are several existing programs that have trained dolphins and sea lions for such a mission. However, the issue of misunderstanding between the animal and the handler exists during a mission. Overall, for both humans and mammals, the major disadvantage is risking their lives by sending them into a minefield (Brown et al., 2012).

Using AUVs for MCM gives the advantage of keeping all personnel at a safe distance by allowing for autonomous operation. When a group of networked vehicles is available, this has the potential to reduce time, cost, and efforts compared to single platforms and current conventional methods. Such a configuration could also introduce distributed and more efficient area coverage.

Related Work

Efforts to improve underwater sensor network (UWSN) performance are commonly aimed at modem development

and network protocol design (Partan et al., 2007; Kong et al., 2005; Cui et al., 2006). When moving platforms are the focus of the network configuration, solutions are driven by ideas adopted by the robotics community. Examples include adapting coordination techniques, such as auction mechanisms (Sariel et al., 2008; DeMarco et al., 2011). Often such approaches do not take into account the limitations imposed by the communication in the underwater channel. Some methods for reducing reliance on communication using prediction models are also available (Sotzing & Lane, 2010); however, they also rely on anticipated environmental conditions.

The work in this paper was developed with the focus of adapting optimization techniques to the appropriate application constraints. Relevant ideas have been used for a group of networked surface and underwater vehicles to adapt their formation to the water basin borders (Kemna et al., 2015). The possibility of a group of vehicles reconfiguring their positions has also been recognized when the nodes need to adapt to unexpected conditions or to seek optimal placement (Braca et al., 2014; Yilmaz et al., 2008). However, such solutions aimed at improving autonomy often discount or neglect the issue of communication.

The idea of synchronous rendezvous has been recognized and adopted for ad hoc networks of mobile autonomous agents (Cortes et al., 2006); however, it is not a typical approach for UWSN. Although it provides a means to avoid the communication restriction by allowing all nodes to meet and plan further actions, one major drawback is that part of the resources in the system are sacrificed to allow the nodes to travel to the appointed

place. To reduce the lost time, these points can be preplanned in a static sequence to guarantee optimality. This, however, introduces rigidness and lack of adaptability to external events. Therefore, we propose a rendezvous approach that allows dynamic online point allocation based on the information gathered by the vehicles and their future goals.

RP Approach

To improve the resource usage in the system, we consider a specific application and scenario to measure the loss and evaluate the significance of parameters for optimizing the RP scheduling. This paper looks into applying the RP approach to MCM and the typical operation specifics are presented. Furthermore, the loss mechanism is explained with regards to the selected scenario.

MCM Phases and Operation for AUVs

A typical mine hunting operation has five phases:

- **Search:** An area is scanned for mine-like objects (MLO). To secure complete coverage, often the platform is moved in a lawnmower pattern.
- **Detection:** Contact data are received from sensors, location is recorded, and a message of the contact and its location is created.
- **Classification:** A decision is made as to whether an object is a mine-like or non-mine-like. This is done by using autonomous target recognition software or a human operator. However, currently this decision is not trusted to be made autonomously.
- **Identification:** This determines the type of the mine so further neutralization strategies can be employed. Often, there is a long delay between

Identification and Neutralization phases, due to the system lacking the ability of autonomous Classification and Identification, which means the data first have to be recovered and processed off-board at the end of the search mission and before the neutralization phase (Brown et al., 2012).

- **Neutralization:** A mine is considered neutralized once its location is defined so it can be avoided. In case the platform cannot evade the mine, other measures are adopted. Those can include destroying the mine, disabling its detonation ability, or disabling its ability to detect.

The work in this paper is concerned with the Search and Identify phases, without taking into account the sensor specifics or the autonomous target recognition restrictions. Instead, it focuses on optimizing the collaboration between multiple platforms. The Neutralize phase is excluded as often a ROV, rather than AUV, is used to properly guide a disabling mechanism.

A typical multivehicle MCM mission configuration includes two types of sensor packages: Search-Classify-Map (SCM) and Reacquire-Identify (RI) (Freitag et al., 2005). The SCM relies on a coarse side-scan sonar allowing faster speed during the searching phase. The RI phase makes use of a high-resolution sensor, such as multi-beam sonar, that collects images for final identification and decision making. Often these two tasks are performed by separate vehicles. The SCM or search vehicle follows a lawnmower pattern, while the RI vehicle relocates the target and further examines it.

RP Loss in MCM Scenario

The limitation of using separate vehicles for distinct tasks is not

necessarily due to hardware restrictions. Modern vehicles can have multiple sensors mounted on the same platform. However, coordinated position and task reconfigurability of multiple networked vehicles is still a big issue underwater. Using RPs throughout the mission enables communication between the AUVs and thus allows for dynamic task reallocation. This can aid higher resource utilization in the network. On the other hand, there is a trade-off with the time spent for the platforms to travel to RP. Evaluating and minimizing this time loss is vital for the approach to be applicable.

In order to schedule an RP, all vehicles in the system have to agree on the most convenient time and location to meet. This is done multiple times throughout the mission, and the intervals between RPs are adapted based on the number of contacts found. We divide the RP scheduling into two stages: (1) select the time and (2) select the coordinates of the RP. To minimize the vehicle traveling time toward the RP, we want to minimize the total number of RPs and push the next point as far in time as possible. On the other hand, we want to give the system nodes regular chances to adjust future strategy and provide updates to the operator. It is useful to define a suitable time interval that satisfies the opposing demands by showing when the resource loss becomes prohibitive for the mission.

The resource loss per vehicle is defined as the time spent by each platform to travel to the RP instead of doing mission-related task. That is, travel time from the point when the vehicle stops its search function and goes to the RP. Equation 1 gives this relation by calculating what fraction

of the time window between RPs is spent for reaching the RP:

$$\text{loss} = \begin{cases} \frac{x}{v \times t_{RP}} \times \frac{1}{2} \left(1 - \frac{1}{n} \right), & n > 1 \\ \frac{x}{v \times t_{RP}} \times \frac{1}{2n}, & n = 1 \end{cases} \quad (1)$$

where x is the width of the search area, n is the number of vehicles (the cases and transformations relevant to n are explained further), v is speed, and t_{RP} is the time until the next RP. An important note is the reasoning behind the choice to evaluate the loss per single vehicle and per single RP interval. First, a single platform loss gives flexibility for reconfigurability throughout the mission. Second, the single RP interval evaluation, as opposed to total mission time, comes from the fact that all RP intervals vary, as they are a function of the number and location of contacts found during the search phase. Therefore, the resulting loss for adopting the RP approach will be additive, but nevertheless each time interval will be unique.

In order to apply Equation 1, some assumptions are made: the area is searched sequentially; the vehicles are homogeneous and have the same speed. Since the resource loss calculation is very dependent on the geometry of the search area, Figure 1 gives a graphical representation of the scenario considered in this paper for evaluating the RP approach. After defining the favorable parameters for minimizing the loss, some conclusions can be drawn on when this approach might not be applicable due to prohibitive losses.

The mission scenario considered for the remainder of the simulations in this paper is demining a strip near the shore. Typically, the width would

be much smaller compared to the length of the area. Another assumption is that the vehicles will not be able to cover the whole area before their batteries are exhausted. The overall purpose of the mission is to explore as much of the area as possible, while having the constraint of revisiting the detected MLOs.

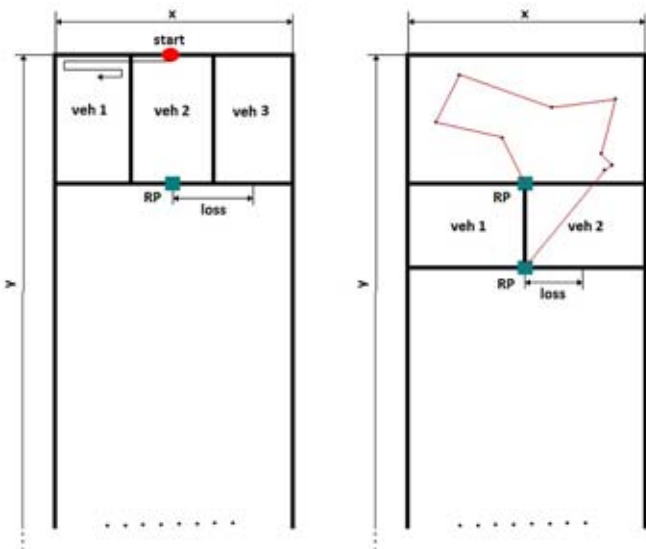
In Figure 1, x and y are the dimensions of the searched area in the simulated scenario. The red circle on the top left side pinpoints the starting position of three available vehicles. They are all equipped with search (side-scan sonar) and RI (multibeam) sensors and can perform both SCM and RI tasks. The first RP is predefined and the speed of the vehicles is known, so this can give a good idea of the location of the next meeting point as well as the area that will be covered by each platform. Since the vehicles are homogeneous, all three search areas will be equal ($\text{area}_{veh1} = \text{area}_{veh2} = \text{area}_{veh3}$).

The right-hand side of Figure 1 gives an example of the continuation of the mission after the first RP. At the RP, all vehicles have shared the location of the contacts they have encountered. The path and the required time to revisit them have been calculated. A decision has been made that one vehicle will be reallocated with an RI task and follow all known contacts (the route is drawn in red in Figure 1) and two platforms will continue in search mode, but now with changed area patterns.

Given the scenario from Figure 1, the loss calculation from Equation 1 can be further clarified. Normally, the AUVs would search in a lawnmower pattern, as shown in the first vehicle's search box ('veh 1', left-hand side of Figure 1). At the time of the RP, this will bring the AUV either at the far or close corner of its search

FIGURE 1

Rendezvous point approach: Left—starting point to first RP. Right—example scenario between two RPs. (Color version of figures are available online at: <http://www.ingentaconnect.com/content/mts/mtsj/2016/00000050/00000002>.)



box, which will define the distance and the subsequent resource loss to the RP. However, the simulation is not optimized to always position the nodes at the near corner. To account for this, the function in Equation 1 is adjusted to be proportional to the number of vehicles performing the search phase. The special case when $n = 1$ is required as otherwise it would result in $\text{loss} = 0$. The current penalty for this case resembles the loss of $n = 2$. With this correction, the calculation always assumes the distance between the middle point of the platform's search area (on the y axis, same as where the RP is) and the RP point (this distance is noted on both sides of Figure 1). The distance penalty is proportionate and increases when increasing the number of search platforms. The loss calculation also depends on the speed of the platforms—the faster they are, the less time is wasted to travel to the RP. And lastly, the time to the next RP defines what fraction of the total time will be used

for task-related purposes and what part will be traveling to the meeting point.

It is obvious that the longer the time between the rendezvous, the smaller fraction of the time will be lost in traveling there. On the other hand, there is a limitation on this time depending on how often the operator would need an update from the network. To evaluate when the loss becomes prohibitive or to define the minimum time for RP, we have parameterized Equation 1, and the result is shown on Figure 2. The graph presents the loss for a group of two and three vehicles, respectively, for different speed values, v , and width of the searched area, x , while the RP time interval and the length of the search area are kept constant ($RP = 1 \text{ h}$, $y = 5000 \text{ m}$). Then, in Figure 3, we have selected favorable, but realistic, conditions—3 vehicles, speed, 2 m/s and width of 2,500 m. The plot shows what percentage of the total time is lost if

we vary the time of the RP. This can be used as a rule of thumb guidance of the minimum time limit of the next RP.

In the scenario we have selected in Figure 3, RP between 1 and 2 h gives a loss between 5% and 12% of the total time. If this is considered unacceptable by the operator, the time window can be moved further in time. The calculations in the next sections adopt the parameters used in Figure 3 ($n = 3$, $x = 2,500 \text{ m}$, $v = 2 \text{ m/s}$) and define an RP interval of 1 h assuming there is no other parameter to base the decision on. The scenario from Figure 1 is used throughout all simulations for the remainder of the paper.

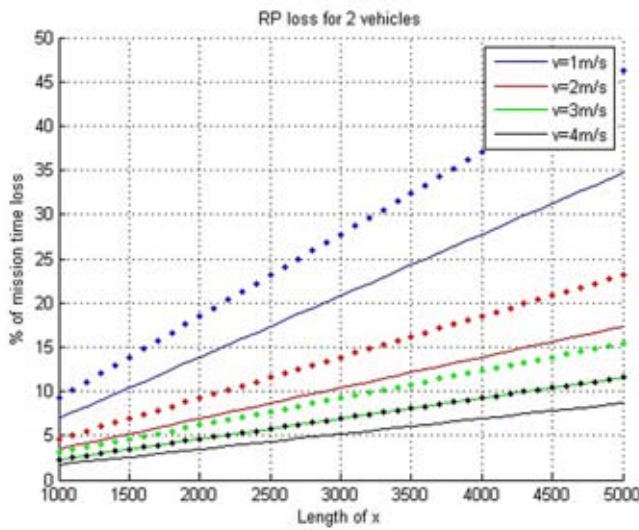
RP Scheduling and Analysis

Defining the lower boundary for scheduling RP is useful when there is no other information available. However, the main advantage of the RP approach comes from the ability to reallocate vehicle tasks based on the information they have gathered during the search.

For example, if we assume the scenario from Figure 1, on the right, but without utilizing the RP technique, at the start of the mission two vehicles will be performing search tasks and they will send the locations of the detected MLOs to the third vehicle that is tasked with RI. However, if there is no prior information about what number of targets to expect, the mission can be completed with few detected MLOs or with a very large number. In the former case, the RI vehicle will be idle most of the time; in the latter, the mission will be incomplete with targets observed only with low-resolution sensor. This scenario was assumed as a benchmark case and adopted in all

FIGURE 2

Loss calculation for two vehicles (lines) and three vehicles (dots): different speed values and width of search area (x), fixed RP time (1 h), and fixed length of the y dimension of searched space (5,000 m).



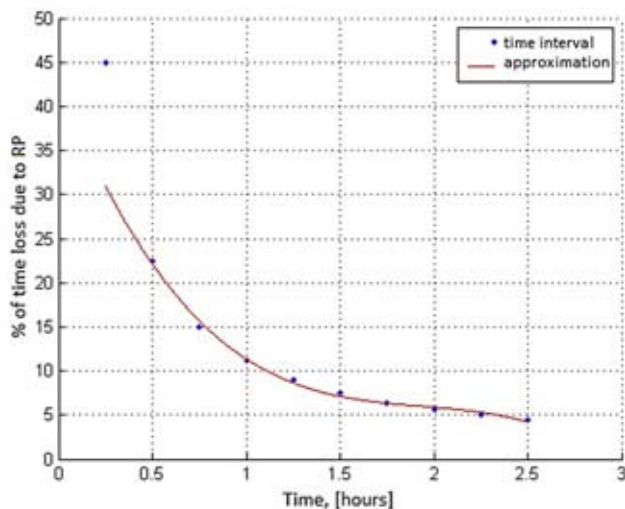
simulations throughout the remainder of this paper for comparison with the RP approach.

A higher amount of the system resource could be utilized if the vehicles are retasked adaptively according to the number of detected contacts. During an RP, a decision is made whether

there is a need to retask a search vehicle into an RI vehicle and vice versa based on how many detections were made during the previous RP interval. Therefore, the number of detected targets or the time it takes for the RI vehicle(s) to revisit them is the main parameter that decides how to utilize the avail-

FIGURE 3

Loss of time resource (yaxis) vs. total time between RP (xaxis)—calculation based on Equation 1 (parameters used: $n = 3$; $x = 2,500$ m; $v = 2$ m/s).



able vehicles as well as how to schedule the RP:

$$t_{RP} = f(t_{RI} + t_{require}), [\min, \max] \quad (2)$$

where t_{RI} is a calculation of the time required for a single vehicle to travel in an optimal path and visit all detected MLOs to identify them. Additional time for reacquiring the target locations once the AUV is at the reported coordinates and collecting high-resolution sensory information was added by the $t_{require}$ term. For more realistic calculation, this parameter needs to be adjusted depending on the mission conditions and the platform sensors. The $[\min, \max]$ interval is derived by using Equation 1 and Figure 3.

The second stage of scheduling the next RP is the position estimation of the vehicles at the time when they will be advancing toward it. This calculation is based on predicting the vehicles' positions at the next t_{RP} , or the area coverage of the search AUVs. The $\text{Area}_{\text{search}}$ parameter in Equation 3 gives the area that will be covered by the search vehicles in the time interval between RPs. This calculation is performed during the meeting at RP, after the following RP time is defined by Equation 2. The position of the search vehicles coincides with the y -axis from Figure 1, where the RP is positioned.

$$\text{Area}_{\text{search}} = v \times \text{sw} \times t_{RP} \times \text{loss} \times n \quad (3)$$

where v is speed of a vehicle, sw is swath width of the vehicle's sensor, t_{RP} is time until next RP, loss is the resource waste for traveling to RP using Equation 1, and n is number of AUVs. However, since all platforms are assumed to be of the same type, at time

t_{RP} , all nodes will be aligned at the same y coordinate in the search space. Therefore, the location of the RP is the middle of the width of the search area at this y coordinate, as seen in Figure 1. Equation 3 accounts only for the positions of the search vehicles. The RI vehicles follow the shortest path between the contacts they will be revisiting and reach back to the current RP. The advancement over the y -axis made by the search vehicles has not been considered for the RI vehicles.

These relations were used to explore the gains of network reconfigurability by applying the RP approach. The steps used in our simulation are summarized in the pseudo code in Algorithm 1, as well as the rule-based decision making for how many platforms to employ search and RI tasks.

At line 3, the first RP is predefined. It is assumed that no prior information is available at the start of the mission; hence, the RP time is solely driven by the loss calculation or given the minimum value from Equation 2. The simulation runs until the mission_time or the sum of the RP time windows exceeds a predefined threshold. This threshold was selected as a percentage of typical battery capacity of an AUV —70% of 10 h (line 7). Depending on the selected parameters, the average resource loss and search area are calculated (lines 8 and 9). Once all platforms reach the first RP, they will share information about the detected targets. Communication at RP is assumed available. The MLOs are simulated by generating a random number of targets, limited in number, and with locations constrained within the area that have been searched in the time window (line 10). The shortest path to revisit them is then calculated (line 11).

ALGORITHM 1

Dynamic allocation of vehicle tasks and RP.

```

1: procedure SCHEDULE RPs
2:    $min\_int \leftarrow min\ loss\ limit\ from\ Graph\ 4$ 
3:    $t_{RP} = min\_int \leftarrow assign\ time\ for\ first\ RP$ 
4:    $n \leftarrow number\ search\ vehicles$ 
5:    $targets = 0$ 
6:    $mission\_time = t_{RP}$ 
7:   while  $mission\_time < threshold$  do
8:     Calculate loss using Equation 1
9:     Calculate search area using Equation 3
10:     $targets = +new.targ \leftarrow generate\ MLOs\ for\ RI\ (applied\ limit\ t_{RI} < min\_int * 3)$ 
11:     $t_{RI} \leftarrow calculate\ RI\ time\ (Nearest\ Neighbor)$ 
12:    if ( $t_{RI} > min\_int * 3$ ) then
13:      break
14:    else
15:      if  $t_{RI} \in [min\_int; min\_int * 2]$  then
16:         $t_{RP} = t_{RI}$ 
17:         $n = n - 1$ 
18:         $targets = 0$ 
19:      else
20:        if  $t_{RI} \in [min\_int * 2; min\_int * 3]$  then
21:           $t_{RP} = t_{RI}/2$ 
22:           $n = n - 2$ 
23:           $targets = 0$ 
24:        else
25:           $t_{RP} = min\_int$ 
26:           $targets = new.targ$ 
27:        end if
28:      end if
29:       $mission\_time = +t_{RP}$ 
30:    end if
31:  end while

```

The decision making on when to schedule the next RP and how many vehicles to send is given between lines 12 and 30. Simple rule-based logic is used. If the RI time falls in the interval between min_int and $2*min_int$ (line 15), the time for the next RP is selected as the time it will take an RI vehicle to check all targets, the search vehicles are reduced by one and the targets in the searched area are considered identified. In case the time for the RI task exceeds the $2*min_int$ limit – line 20 (due to too many targets), then two vehicles are tasked to perform the RI task and the time for the next RP is half of the RI time. The number of search vehicles is reduced by two, and also all targets are considered identified. In the case when the RI time is below the min_int threshold, it is better to leave the targets unidentified until the next RP cycle. The advantage is that all vehicles will perform search rather than one vehicle tasked with RI and then being idle for portion of the time. The disadvantage is that, on the next cycle, when there are enough targets to identify, the path to travel will be longer. In the next section, this trade-off is explored further. Lines 12 and 13 ensure that the simulation will be terminated in the case that more than two RI vehicles are required to identify the contacts from the previous RP interval.

Results

The function from Algorithm 1 was used in a MATLAB simulation to evaluate the performance of the RP approach when variable numbers of MLOs are detected. This assumes the case where no prior intelligence is available about the expected number of contacts, and thus, the mission operators would be unable to manage the resources in the system offline.

The aim of this work is to show how applying the RP method gives the opportunity for the system to adapt to an unexpected and varying need for retasking the vehicles. On the other hand, a benchmark scenario was designed where the

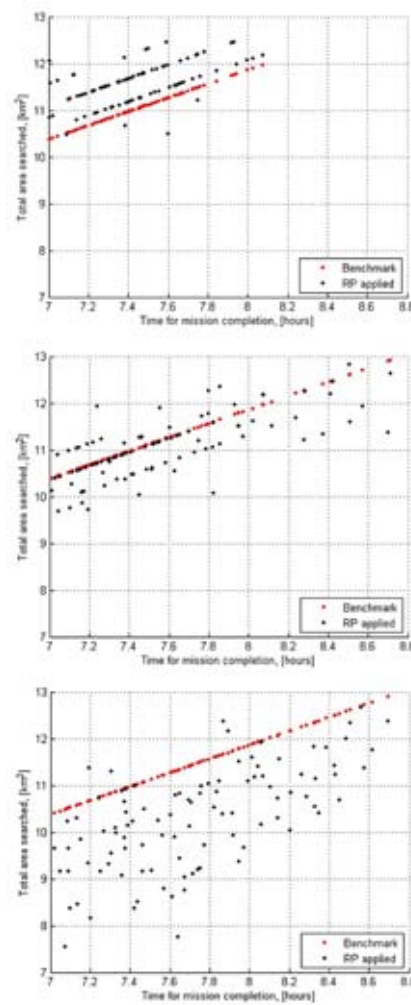
vehicles' functionality is predefined, as would be the case if no autonomy was implemented. Our expectations were that the results would show such architecture makes the system rigid and inefficient. To represent this base case, at the start of our simulated missions, from the total of three vehicles, to match the RP case, two AUVs were designated to perform search and one was tasked with identifying a detected contact. The reason to put more vehicles in search was that the objective of the mission is to maximize the overall search area. The advantage here is that there is no loss introduced from regularly traveling to a meeting point as when the RP method is applied. The benchmark case assumes that the vehicles have the ability to broadcast target locations continuously throughout the duration of the mission with no collision or message loss.

Figure 4 shows three graphs, each representing simulation results with different numbers of detected targets. At the top is a scenario with low number of targets (0–10 generated targets per RP window), the middle graph shows average number of targets (0–20 per RP), and at the bottom is a large number of simulated contacts (0–30 per RP). The choice of target number intervals is somewhat arbitrary, as this parameter is not based on literature or experiments. Since this variable is hard to determine, we have adopted these intervals based on the load that would be generated within the assumed system resources. Thus, each graph shows results for 100 repetitions of Algorithm 1 where the randomization of number and location of MLOs accounts for variability in losses and gains in the system.

The graphs in Figure 4 show the total area searched by the vehicles (depicted on the y axis) throughout

FIGURE 4

Comparison between the RP and benchmark approaches applied to MCM mission by plotting the search area gained by each method. The three graphs show how the results change when the number of targets increases: top graph gives a simulation with low number of targets (0 to 10), middle one doubles the targets (0 to 20), and bottom graph shows a cluttered environment (0 to 30 contacts per RP window).



the available mission time (shown in minutes on the x axis). The scattered black dots are full mission simulations with the RP approach applied, while the red dots are simulations with designated vehicles tasks or the benchmark case. It is essential to clarify that the mission time per simulation is defined by the RP approach, as de-

scribed in Algorithm 1 on line 7, and then this limit is applied to the benchmark case, where the same input of target distribution and number is used to calculate the overall area searched by this architecture. This creates a pair of RP and benchmark case simulations that give a comparable output as all inputs are the same. In Figure 4, there are 100 pairs in each graph, which allow an evaluation of the loss or gain of applying the different methods, even though multiple variables are present in the simulations, such as number and location of the targets, as well as mission duration.

It can be seen on the graphs that in all cases the red dots follow a linear relationship—the more mission time available, the larger area is searched. On the other hand, the black dots are scattered below and above this red line, showing lower resource utilization if they are below the red line and higher if they are above.

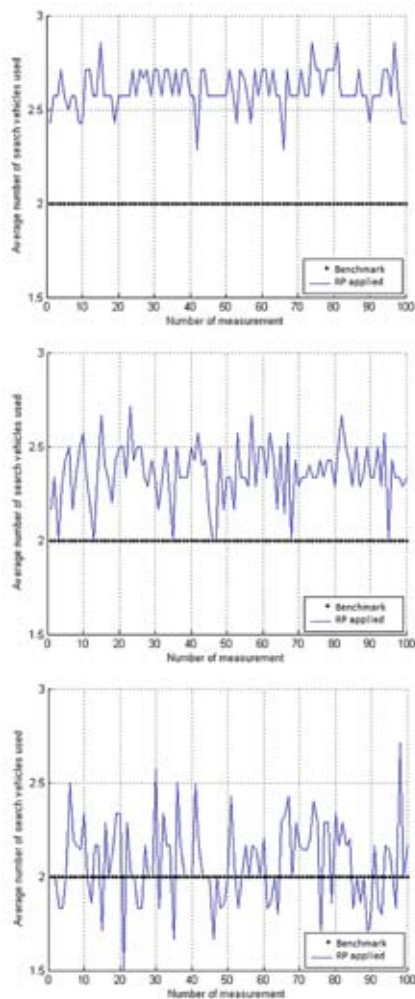
As expected, in the example of fewer targets (top graph in Figure 4), most of the simulations show better performance for the RP approach, which allows for function reconfigurability, compared to the case of predefined tasks for the AUVs. The reason is that the RI vehicle from the benchmark mission is being idle for the majority of the time, as there are not enough targets to fill its schedule. On the other hand, the third vehicle in the RP simulations is performing a search function during most of the RP windows as there were not enough targets found to justify the RI task. It can be observed that with increasing the number of targets, the advantage of the RP is lost due to multiple vehicles tasked with RI throughout the mission. However, in the case of a cluttered environment with many contacts present, the vehicles from the benchmark case

are not able to revisit all detections as only one vehicle is tasked with RI, and its resources are not enough. The comparison between the two approaches in their ability to revisit and identify the contacts has been analyzed further in this paper, and simulation results are available in Figure 7.

Figure 5 compares the distribution of the search resource in the RP and benchmark case. The y axis gives

FIGURE 5

Comparison between the RP and benchmark approaches by giving the average number of search vehicles used per mission. The graphs show the decreasing availability of search resource (top to bottom) in the RP case by increasing the number of detections in the simulations.



the average number of search vehicles utilized per simulation, and the x axis provides the simulation number. Since the base case is constantly using two search vehicles, regardless of the mission circumstances, there are 100 equally spaced black dots at $y = 2$ for every simulation number on all three graphs. When RP is applied, the search platforms change their number at every RP window depending on the available MLOs, as sometimes the RI vehicles can account for 0, 1, or 2 of the total number of vehicles (Algorithm 1, lines 15–28). Each data point from the blue lines in Figure 5 corresponds to the average number of search vehicles utilized throughout each simulation.

This result can be correlated with the graphs in Figure 4, explaining the higher search area covered in the case when less vehicles are tasked with RI (top graphs in both figures where less targets are found) and thus the average search platform number is much higher. The bottom graph in Figure 5, where the RP network of vehicles had to adapt to a large number of targets, shows that in a proportion of the simulations less than two vehicles on average were available for the whole mission. This can explain the majority of black scattered dots moving toward the bottom right corner in the third graph of Figure 4. This is the undesirable situation when more time spent at the MCM mission yields less area searched.

On the other hand, even in the unfavorable event of encountering many targets, the RP guarantees that all detections are revisited. The approach was built with this core objective in mind and it defined a condition driving the whole decision process in Algorithm 1. For the benchmark case, some contacts were not revisited as the RI

vehicle resource would not be enough. This is another advantage for the base scenario, together with the unlimited communication mentioned earlier, which makes its results to look more favorable. However, the objective to provide high-resolution images of all MLOs is violated in the benchmark case and thus making the RP approach show more pessimistic results than it would in a fair comparison. The RI success rate for both methods is further analyzed in the next section.

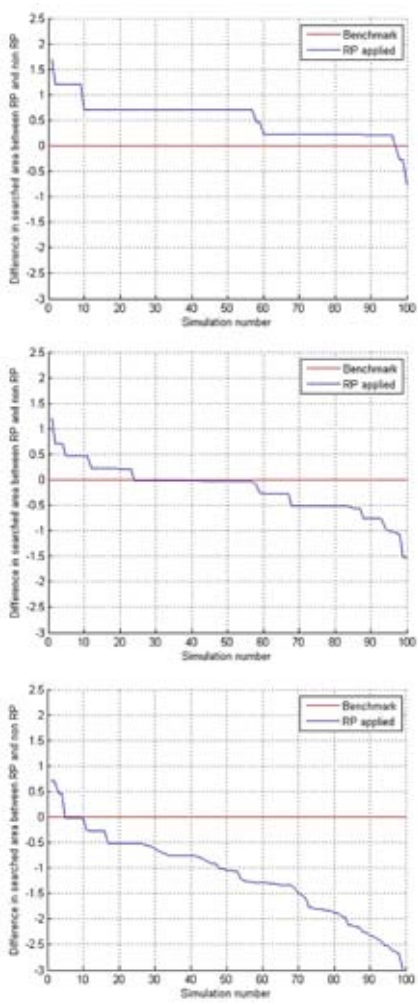
Analysis

In order to give a more suitable representation of the outcomes showing the efficiency gains and losses of the RP method, Figure 6 displays the same data as used to present results in Figure 4, but in a different format. To achieve a better visualization to distinguish between the different approaches, the benchmark case data points were rotated and translated to coincide with the $x = 0$ axis and plotted as a red line. Then, the difference between the area searched by using RP and benchmark was calculated. This emphasized the discrepancy in overall area between the RP and base case pairs. To capture the dynamics of this variation, these pairs were further sorted in a descending order, which resulted in the blue plotted line on all graphs in Figure 6. Such result representation is easier to evaluate by clearly differentiating how likely it is for the RP approach to be beneficial. Above the red line or the zero of the y axis, the RP approach gains additional search area even though the vehicles waste time resource for multiple meetings. If the blue line is below the red one, then the simulation instance results in a loss of search area.

In the top graph of Figure 6, showing results from a search with low

FIGURE 6

Normalized and sorted simulation results comparing the gain of search area achieved by applying RP and base case. The top graph gives a simulation with low number of targets (0 to 10), middle one doubles the targets (0 to 20), and the bottom graph shows a cluttered environment (0 to 30 contacts per RP window).

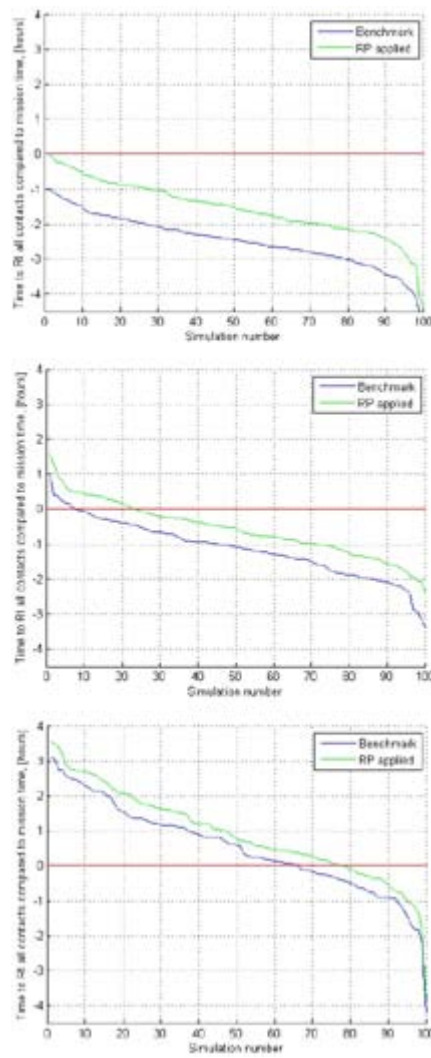


number of contacts, the RP gives a significant gain over the benchmark case in the majority of the simulations, even though the loss for vehicles meeting is accounted for. It is obvious that this is the most advantageous situation to apply RP.

The middle graph gives the resulting area search difference when doubling the number of targets from the previous case. Now it is visible that the majority of the blue line is under

FIGURE 7

Normalized and sorted simulation results comparing the time required to reacquire and identify (RI) all detected contacts for applying RP versus the benchmark case. The top graph gives a simulation with a low number of targets (0 to 10), the middle one doubles the targets (0 to 20), and the bottom graph shows a cluttered environment (0 to 30 contacts per RP window).



the red line; i.e., most simulations indicate a loss to the system when applying the RP. However, a large part of the simulation points fall very near the red line. In about 40% of the simulations, the results are within 0.2 km^2 of total search area. This accounts for about 3 to 4 min of a single

vehicles operation time, according to Equation 1. This shows that, half of the time, the RP approach is almost indistinguishably as good as the benchmark case. However, it adds the operational advantages discussed in Section 4 for system monitoring and periodic data gathering.

The final graph presents a state when there is an extensive number of contacts simulated during the mission and shows the expected undesirable results from the RP approach—a lot of resources would be spent on relocating these contacts, and this will add to the time loss brought from the regular meetings. In reality, most of the contacts would be FAs. Environments that are characterized by many FAs in the vehicle sensor, such as rocky sea bottom, are unfavorable for the RP approach. It can be seen on the graph that only very few data points have the blue line above the red, and in the majority of the cases this approach brings loss. In addition, the loss propagates to significant difference in search area, in the order of 1.5 km^2 and above, for the 30% of the cases.

So far, only the search resource in the system has been analyzed. Figure 7 gives an insight how the benchmark and RP approach spend their RI resources. The x axis on all graphs is the simulation number and the y axis measures the time it would require to spend in RI phase per mission. In order to make the comparison clearer, the results of the 100 repeated simulations were sorted in a descending order. The red line is the mission time (different for each iteration of the algorithm). The blue line follows the benchmark results, and the green line follows the corresponding RP results. It is clear that the benchmark case always uses less resources compared to when RP is applied (the blue line is always below the

green line). This comes from the fact that the RI vehicles in the RP simulations have to go back to each contact location only after its route is defined at the meeting point, which adds a time overhead. On the other hand, the benchmark case assumed perfect communication, so the two search vehicles can instantly send their contact locations and the RI vehicle can select the shortest path without delay.

In all the cases when the benchmark is above the red line or the limit of the mission time, some contacts remain unidentified, as the RI resource is not sufficient. This is evident in the bottom graph where the majority of the simulations result in contacts requiring extra RI time. On the other hand, the RP approach adaptively reallocates part of its resource from search into RI, resulting in more than one RI vehicle per mission on average, as can be seen in Figure 5. Therefore, all contacts are identified by the end of the mission. This flexibility gives an advantage to the RP approach that can surpass the overall loss of time to meet and the reduced total search area.

A disadvantage of the RP in relation to the RI resource is that the contacts are always revisited after a meeting point. This results in a delayed reaction, and the current simulation does not allow for the contacts from the last RP interval to be revisited (as the algorithm terminates once the mission time reaches the selected threshold—line 7 in Algorithm 1). This is an oversight of the approach, but it does not violate the conclusions made in this paper, as both the benchmark and the applied RP simulations disregard these contacts. In a real MCM or experimental setting, where revisiting the contacts is crucial, this can be easily amended by setting the last RP interval to force

each search vehicle to perform the RI task for its contacts before it goes back to the mission end point. This, however, would not contribute to the current evaluation and was not included in the simulations.

Conclusion and Future Direction

This paper has presented the idea of adaptive scheduling of RPs for MCM application with AUVs. The benefit of using RP is that the vehicles can be utilized at a constant rate independent of the number of targets detected throughout the mission. In contrast, when adopting a typical configuration where the functions of search and ID vehicles are separated from the start of the mission, the overall time to achieve the same result could be significantly increased if there are large numbers of MLOs or the ID vehicle could be underutilized if their number is low. The conventional approach thus becomes less efficient compared to the presented RP method.

This work can be improved by relaxing or refining some of the assumptions which forced pessimistic calculations, such as adjusting the position of the search vehicle when calculating the loss and the time required for reacquiring a target. Another important change would be allowing different kinds of vehicles with varying speed and sensors that will add diversity to the simulation and make it more realistic. Finally, relaxing the assumption of sequential search allows for the use of a probabilistic model of selecting which area to be given priority for exploration and which one needs a repeated coverage. This also calls for more sophisticated decision making, such as using Markov processes.

Acknowledgment

This project is funded by Atlas Elektronik UK and EPSRC Doctoral Training Centre no: EP/G037264/1. The authors would like to thank A. Gibbert, A. Charlish, and R. Brind for being available and providing early feedback to this work.

Authors

Veronika Yordanova and Hugh Griffiths
Department of Electronic and Electrical Engineering
University College London
Torrington Place,
London WC1E 7JE, UK
Email: veronika.yordanova.11@ucl.ac.uk; h.griffiths@ucl.ac.uk

References

- Akyildiz, I.F., Pompili, D., & Melodia, T.** 2005. Underwater acoustic sensor networks: research challenges. *Ad Hoc Netw.* 3(3): 257-79. <http://dx.doi.org/10.1016/j.adhoc.2005.01.004>.
- Benjamin, M.R., & Curcio, J.A.** 2004. COLREGS-based navigation of autonomous marine vehicles. In: *Proceedings of Autonomous Underwater Vehicles*. pp. 32-9. Sebasco, ME: IEEE/OES.
- Braca, P., Goldhahn, R., LePage, K.D., Marano, S., Matta, V., & Willett, P.** 2014. Cognitive multistatic AUV networks. In: *17th International Conference on Information Fusion (FUSION)*, 1-7. Salamanca: IEEE.
- Brown, T., Damiano, J., Jhala, S., Moore, R., Morgan, B., Nguyen, V., & Turk, J.** 2012. Next generation mine countermeasures for the very shallow water zone in support of amphibious operations (No. NPS-SE-001). Naval Postgraduate School Monterey CA Department of Systems Engineering.
- Cao, P., & Bell, M.J.** 1999. New methods to evaluate the detection performance of a minehunter (No. DSTO-TN-0200). Defence Science and Technology Organisation Canberra (Australia).

- Cornish**, G.J. 2003. US Naval Mine Warfare Strategy: Analysis of the Way Ahead. Army War Coll Carlisle Barracks PA.
- Cortes**, J., Martínez, S., & Bullo, F. 2006. Robust rendezvous for mobile autonomous agents via proximity graphs in arbitrary dimensions. *IEEE T Automat Contr.* 51(8):1289-98. <http://dx.doi.org/10.1109/TAC.2006.878713>.
- Cui**, J.H., Kong, J., Gerla, M., & Zhou, S. 2006. The challenges of building mobile underwater wireless networks for aquatic applications. *IEEE Netw.* 20(3):12-8. <http://dx.doi.org/10.1109/MNET.2006.1637927>.
- DeMarco**, K., West, M.E., & Collins, T.R. 2011. An implementation of ROS on the Yellowfin autonomous underwater vehicle (AUV). In: OCEANS 2011, 1-7. Kona: MTS/IEEE.
- Dugelay**, S., Williams, D.P., Okopal, G., Connors, W.A., Midtgård, Ø., Sæbø, T., ... Hesby, A. 2015. MANEX'14: Experimental description and preliminary results. Tech. Rep.: NATO STO Center for Marine Research and Experimentation, La Spezia, Italy: CMRE-FR-2014-013.
- Freitag**, L., Grund, M., Von Alt, C., Stokey, R., & Austin, T. 2005. A shallow water acoustic network for mine countermeasures operations with autonomous underwater vehicles. In: Undersea Defence Technology (UDT), Amsterdam: UDT. pp. 1-6.
- Kalwa**, J., Pascoal, A., Ridao, P., Birk, A., Glotzbach, T., Brignone, L., & Bibuli, M. 2015. EU project MORPH: Current status after 3 years of cooperation under and above water. *IFAC-PapersOnLine.* 48(2): 119-24. <http://dx.doi.org/10.1016/j.ifacol.2015.06.019>.
- Kemna**, S., Caron, D.A., & Sukhatme, G.S. 2015. Constraint-induced formation switching for adaptive environmental sampling. In: OCEANS 2015, 1-7. Geneva: MTS/IEEE. <http://dx.doi.org/10.1109/oceans-genova.2015.7271361>.
- Kong**, J., Cui, J.H., Wu, D., & Gerla, M. 2005. Building underwater ad-hoc networks and sensor networks for large scale real-time aquatic applications. *IEEE Military Communications Conference, MILCOM 2005.* 3:1535-41. <http://dx.doi.org/10.1109/MILCOM.2005.1605894>.
- Partan**, J., Kurose, J., & Levine, B.N. 2007. A survey of practical issues in underwater networks. *ACM SIGMOBILE Mobile Computing and Communications Review.* 11(4): 23-33. <http://dx.doi.org/10.1145/1347364.1347372>.
- Sariel**, S., Balch, T., & Erdogan, N. 2008. Naval mine countermeasure missions. *IEEE Robot Autom Mag.* 15(1):45-52. <http://dx.doi.org/10.1109/M-RA.2007.914920>.
- Schwarz**, M. 2014. Future mine countermeasures: No easy solutions. *Naval War Coll Rev.* 67(3):123.
- Sotzing**, C.C., & Lane, D.M. 2010. Improving the coordination efficiency of limited communication multi-autonomous underwater vehicle operations using a multiagent architecture. *J Field Robot.* 27(4):412-29. <http://dx.doi.org/10.1002/rob.20340>.
- Truver**, S.C. 2012. Taking mines seriously. *Naval War Coll Rev.* 65(2):1-37.
- Yilmaz**, N.K., Evangelinos, C., Lermusiaux, P.F., & Patrikalakis, N.M. 2008. Path planning of autonomous underwater vehicles for adaptive sampling using mixed integer linear programming. *IEEE J Oceanic Eng.* 33(4):522-37. <http://dx.doi.org/10.1109/JOE.2008.2002105>.

Autonomous Underwater Vehicle Motion Response: A Nonacoustic Tool for Blue Water Navigation

AUTHORS

Supun A. T. Randeni P.

Australian Maritime College,
University of Tasmania

Alexander L. Forrest

Department of Civil and
Environmental Engineering,
University of California-Davis,
and Australian Maritime College,
University of Tasmania

Remo Cossu

School of Civil Engineering,
University of Queensland, and
Australian Maritime College,
University of Tasmania

Zhi Quan Leong

Peter D. King

Dev Ranmuthugala

Australian Maritime College,
University of Tasmania

Introduction

Autonomous underwater vehicles (AUVs) are submarine robots that are able to carry out ocean sampling campaigns (Curtin et al., 1993), bathymetric data collections (Grasmueck et al., 2006), and military and security exercises in unstructured environments (Paull et al., 2014). Accurate point-to-point guidance of an AUV (i.e., navigation) as well as precise knowledge of its position within a 3-D domain (i.e., localization) are mandatory (Paull et al., 2014). Despite the AUVs are being developed since the 1970s, the current navigation and localization tech-

ABSTRACT

Autonomous underwater vehicles (AUVs) use secondary velocity over ground measurements to aid the Inertial Navigation System (INS) to avoid unbounded drift in the point-to-point navigation solution. When operating in deep open ocean (i.e., in blue water—beyond the frequency-specific instrument range), the velocity measurements are either based on water column velocities or completely unavailable. In such scenarios, the velocity-relative-to-water measurements from an acoustic Doppler current profiler (ADCP) are often used for INS aiding. ADCPs have a blanking distance (typically ranging between 0.5 and 5 m) in proximity to the device in which the flow velocity data are undetectable. Hence, water velocities used to aid the INS solution can be significantly different from that near the vehicle and are subjected to significant noise. Previously, the authors introduced a nonacoustic method to calculate the water velocity components of a turbulent water column within the ADCP dead zone using the AUV motion response (referred to as the WVAM method). The current study analyzes the feasibility of incorporating the WVAM method within the INS by investigating the accuracy of it at different turbulence levels of the water column. Findings of this work demonstrate that the threshold limits of the method can be improved in the nonlinear ranges (i.e., at low and high levels of energy); however, by estimating a more accurate representation of vehicle hydrodynamic coefficients, this method has proven robust in a range of tidally induced flow conditions. The WVAM method, in its current state, offers significant potential to make a key contribution to blue water navigation when integrated within the vehicle's INS.

Keywords: water column velocity, INS, autonomous underwater vehicles (AUVs), acoustic Doppler current profilers (ADCPs), WVAM

niques need improvement, particularly for blue water operations (Hegrenæs & Berglund, 2009).

Inertial navigation is one of the key navigation techniques used by AUVs where the rotational and translation accelerations of the AUV are determined using the Inertial Navigation System (INS) sensors. Inertial navigation is most effective when the acceleration solution from the INS is aided with the velocity over ground measurements from a bottom-tracking

Doppler Velocity Logger (DVL) or a GPS. An INS determines the position, velocity, and orientation of the vehicle using the data from inertial measurement units (IMUs) relative to inertial space. Due to inherent errors, the INS navigation solution will have an unbounded drift unless counteracted with the speed over ground velocity estimates (Hegrenæs & Hallingstad, 2011). The DVL bottom track, where the velocity relative to the ground is determined from the Doppler frequency

shift of soundwaves reflected off the seabed, is commonly used for this purpose. This technology is limited by frequency-specific penetration of tens to hundreds of meters through the water column (Hegrenæs et al., 2008).

In blue water, specifically during deep descents/ascents, operating in the mid-water zone and over rough bathymetry, DVL bottom track data may be intermittently or completely unavailable (Hegrenæs et al., 2008). In such cases, as illustrated in Figures 1a and 1b, an alternative approach is to use the DVL water-tracking mode, that is, acoustic Doppler current profiler (ADCP) mode, in conjunction with a real-time current estimation methods to aid the INS navigation so-

lution (Hegrenæs & Berglund, 2009). This method has proven to produce better navigation solutions and less free inertial drift compared to systems utilizing INS alone; however, they are inherently susceptible to instrument noise (Hegrenæs & Berglund, 2009).

In addition to instrument noise, ADCPs or water-tracking DVLs have a blanking distance (i.e., a dead zone) in proximity to the device in which the flow velocity data remain unresolved (Simpson, 2001). The blanking distance can typically span from 0.5 to 5 m from the vehicle depending on the sampling frequency and selected bin size of the instrument (see Figure 1a). Therefore, the water velocity used to aid the INS navigation is at least

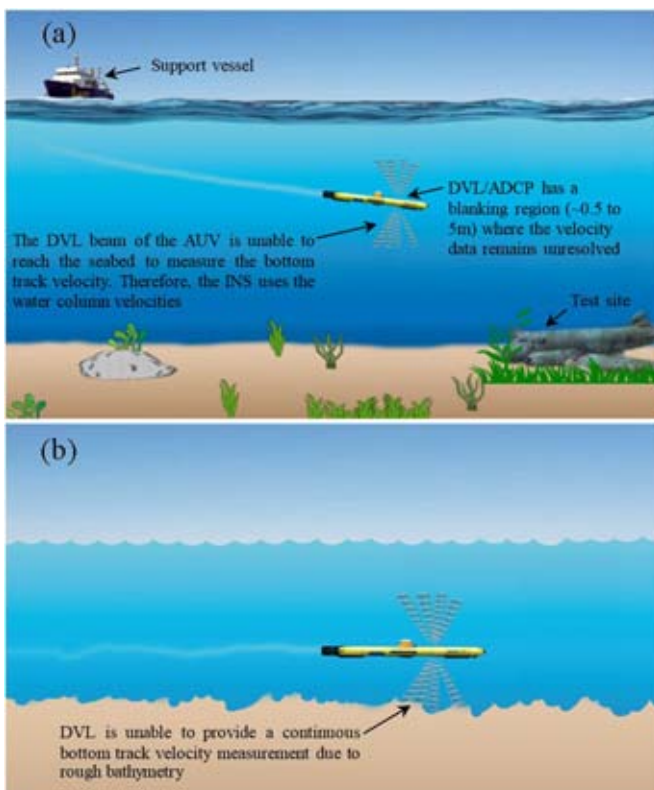
0.5 m and sometimes even up to 5 m from the vehicle resulting in an uncertainty of the water velocity near the vehicle. This can induce error and cause adverse effects on the navigation and localization solutions.

The authors previously introduced a nonacoustic method to calculate the water velocity components of a turbulent water column using the AUV motion response without the aid of an ADCP referred to as the WVAM method (Randeni et al., 2015b). In this method, the water velocities are determined by comparing the motion response of the vehicle when operating within turbulent and calm water environments. A key advantage of the WVAM method is that it is able to estimate the flow velocities at the vehicle's center of buoyancy; however, the authors indicated that the accuracy of the WVAM method might vary with the intensity of the measuring velocity components (Randeni et al., 2015b). That is, the precision of the water velocity measurements from a highly turbulent environment with relatively large velocities may be different than those of low turbulence conditions with lower velocities. The remaining unanswered question was whether the WVAM method is able to measure low and high flow velocities that are likely to be encountered in blue water conditions.

In this context, the current work was conducted as a feasibility study to find the threshold limits by investigating the variation of the WVAM method's accuracy in varying turbulence levels in the water column through field deployments in a river estuary that exhibits strong tidal currents up to 2 m s^{-1} . The uncertainty of the method was calculated based on a direct comparison with velocity measurements obtained from the AUV's ADCP at different

FIGURE 1

(a) An AUV descending to a test site in blue water where the bottom track velocities of the vehicle are unavailable to the INS since the DVL beam span is unable to reach the seabed. (b) DVL is incapable of providing continuous bottom-track velocity measurements when traveling over rough bathymetry.



stages within the tidal cycle. Additional steps to improve the applicability of the WVAM method for blue water navigation are also discussed.

Methodology Instruments

A *Gavia*-class modular AUV was used to test the WVAM method (Randeni et al., 2015a), with the vehicle configured to an overall length of 2.7 m, diameter of 0.2 m, and a dry weight in air of approximately 70 kg (see Figure 2a). The modularized vehicle in the tested configuration consisted of a nose cone, battery, GeoSwath interferometric sonar, 1,200-kHz Teledyne RDI ADCP/DVL, Kefkott T24 INS, and control and propulsion modules, as shown in Figure 2b. The ADCP module of the AUV included two 4-beam ADCPs arranged in a vertical plane to make both upward- and

downward-oriented velocity measurements (see Figure 2c). The ADCPs were set to profile the 9.94 m of water column in 0.5-m range bins so that the three directional water velocity components in the vehicle's body-fixed coordinate system are measured in each bin. Adjacent to the transducers (both above and below), there was a blanking distance of 0.44 m, as shown in Figure 2c. The maximum uncertainty margin of the DVL in measuring the speeds over ground is $\pm 0.03 \text{ m s}^{-1}$ (Hildebrandt & Hilljegerdes, 2010).

The Kefkott T24 INS together with the ADCP/DVL module measured the orientation, velocities in 6 degrees of freedom (6 DOFs), and the position of the AUV. The depth of the vehicle was obtained from the pressure sensor on-board the AUV. These sensor measurements were recorded in the vehicle log at a frequency of 0.87 Hz. The percentage uncertainty

of the pressure sensor is 0.1% giving a depth rate uncertainty margin of $\pm 1.0 \times 10^{-4} \text{ m s}^{-1}$ (Hildebrandt & Hilljegerdes, 2010). The respective uncertainties of the INS in providing the pitch and yaw rates of the AUV are $\pm 7.96 \times 10^{-5} \text{ rad s}^{-1}$ and $\pm 1.60 \times 10^{-4} \text{ rad s}^{-1}$.

Site Description

The objective of this study was to determine the accuracy of the WVAM method in different flow conditions in order to assess the feasibility of using the method for blue water AUV navigation. To achieve this, the WVAM method was tested in the Tamar estuary near the Batman Bridge (see Figures 3a and 3b), located in Tasmania, Australia. Due to the proximity to the open sea and the flow constriction of the river bed, the Tamar estuary exhibits strong tidal currents with maximum flow velocities of up to 2.5 m s^{-1} (see Figure 3c).

Nine AUV runs were conducted along the track line shown in Figure 3b. The first five were conducted on April 14, 2015, and the last four were conducted on April 15, 2015. Runs 1–3 and 6–9 were conducted during slack water as shown in the tidal curve given in Figure 4. The velocity of the tidal currents during the first runs on each day (i.e., Runs 1 and 6) was approximately 0.25 m s^{-1} . Due to the development of the strong flood tide, the flow speeds increased rapidly during the subsequent runs on each day. Runs 4 and 5 were carried out at partially and fully developed flood tide conditions with strong tidal currents (around 2 m s^{-1}).

WVAM Method

For the WVAM method (Randeni et al., 2015a, 2015b), the AUV needs to undergo a straight line, constant

FIGURE 2

(a) Omarama Primary School (Lake Ohau, New Zealand) students inspecting the *Gavia*, the modular AUV that was utilized to test the WVAM method; (b) the tested configuration of the vehicle; and (c) the body-fixed coordinate system (origin at the center of buoyancy—marked by the circle) showing the ADCP beam geometry.

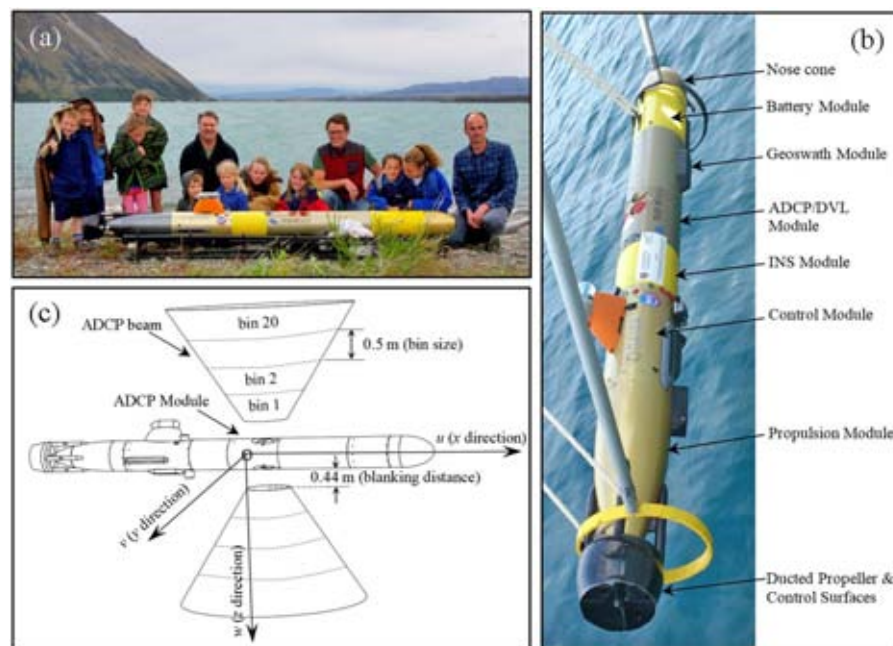
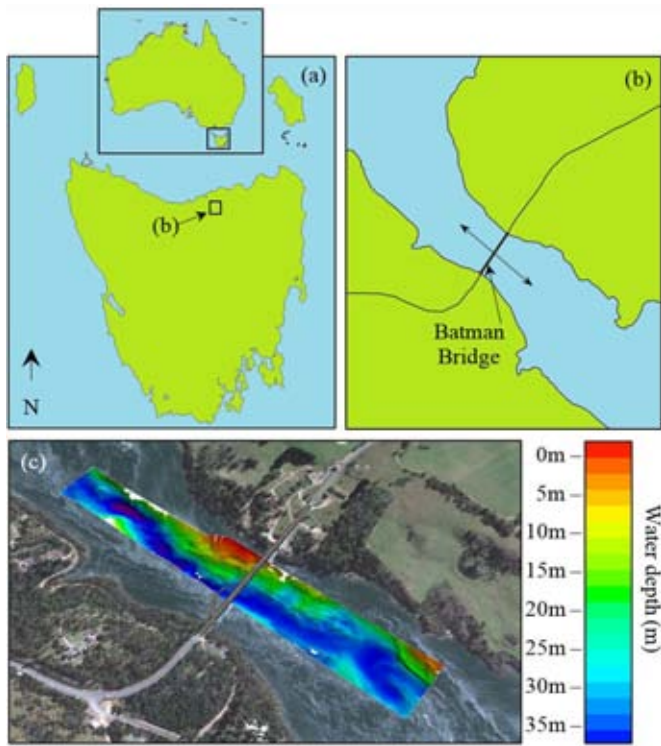


FIGURE 3

(a) The experimental field site in Tasmania, Australia (inset). (b) The Tamar estuary with a bidirectional arrow representing the AUV track. (c) Due to the proximity to the open sea and the flow constriction of the river bed, the site exhibited strong tidal currents.

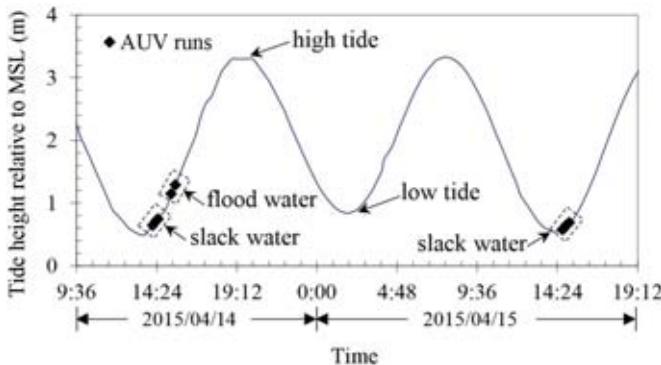


depth trajectory through the region where the water column velocities are to be measured. Typically, when an AUV is operating in an environment with fluctuating water velocities, the forces and moments induced by these velocities can interrupt the control sta-

bility and change the vehicle speed, depth, pitch, and yaw angles from the desired values. In order to compensate for such changes in performance, the vehicle's control system adjusts the revolution speed of the propeller and the angles of the four control sur-

FIGURE 4

The water level relative to the mean sea level (MSL) observed on April 14 and 15, 2015, with the periods that the AUV runs were conducted indicated by filled diamond markers.



faces. In response to these adjustments, the motion of the AUV will change in order to return the AUV to the prescribed mission track unless the propeller and the control surfaces are unable to compensate for the external forces (Kim & Ura, 2003).

The WVAM method uses the compensation commands given by the vehicle's control system to the propulsion motor and control surfaces as recorded in the vehicle log and executes these commands within a simulation model representing a calm water environment. Since there are no disturbing forces due to flow variations in calm water conditions, the simulated vehicle motion will be different than the actual motion. The difference between the two motion responses provides an estimation of the absolute water column velocities in the body-fixed coordinate system.

Equation 1 gives a generalized form of the water velocity calculation used within the WVAM method:

$$\bar{v}_{\text{water}(t)} = \bar{v}_{\text{AUV(turbulent)}(t)} - \bar{v}_{\text{AUV(calm)}(t)} \quad (1)$$

where \bar{v}_{water} is the velocity component of the surrounding water column relative to the earth in the body-fixed coordinate system (see Figure 2c), $\bar{v}_{\text{AUV(turbulent)}}$ is the velocity component of the AUV observed in the turbulent environment, and $\bar{v}_{\text{AUV(calm)}}$ is the velocity component obtained from the calm water simulation when the control commands recorded during the field tests were simulated. Subscript t indicates the time step. To estimate the water velocity component along the x , y , and z axes, \bar{v} is replaced with the surge, sway, and heave velocity components (i.e., u , v , and w) of the vehicle in the body-fixed frame of reference, respectively.

Simulation Model and Hydrodynamic Coefficients

The simulation model of the *Gavia* AUV was developed to reproduce the vehicle's trajectory within a calm water environment in response to the time series of the control commands. It requires an accurate approximation of the associated hydrodynamic coefficients (i.e., a representation of the forces and moments acting on the vehicle at different orientations, velocities) to adequately predict the motion of the AUV. Generally, the forces and moments acting on submerged bodies in 6 DOFs are highly nonlinear (Lewis, 1988). For example, the vertical hydrodynamic force acting on an AUV varies linearly with its pitch angle up to a value of around $\pm 8^\circ$, beyond which it becomes nonlinear (Randeni et al., 2015a). Similar threshold values exist for other hydrodynamic forces and moments transitioning between their respective linear and nonlinear ranges. Therefore, the hydrodynamic coefficients estimated for the linear ranges are only valid up to a certain threshold value (Lewis, 1988).

During the initial development of the WVAM method, a basic curve fitting method was utilized to determine the hydrodynamic coefficients due to its relative simplicity (Randeni et al., 2015a). The coefficients obtained from this method were limited to small angles of incidence (i.e., generally below 8°) restricting them to the linear range. When an AUV operates in turbulent environments, its pitch and yaw angles typically fluctuate around the baseline values. The magnitude of these fluctuations increases with increasing levels of turbulence due to the inability of the AUV's control system to compensate for the severe disturbance forces (Kim & Ura, 2003). Therefore, in extremely turbulent water columns, these fluctuation

angles will be greater than $\pm 8^\circ$. Thus, a simulation model that is limited to linear hydrodynamics data is unable to adequately replicate the motion of the vehicle in extreme environments.

Results and Discussion

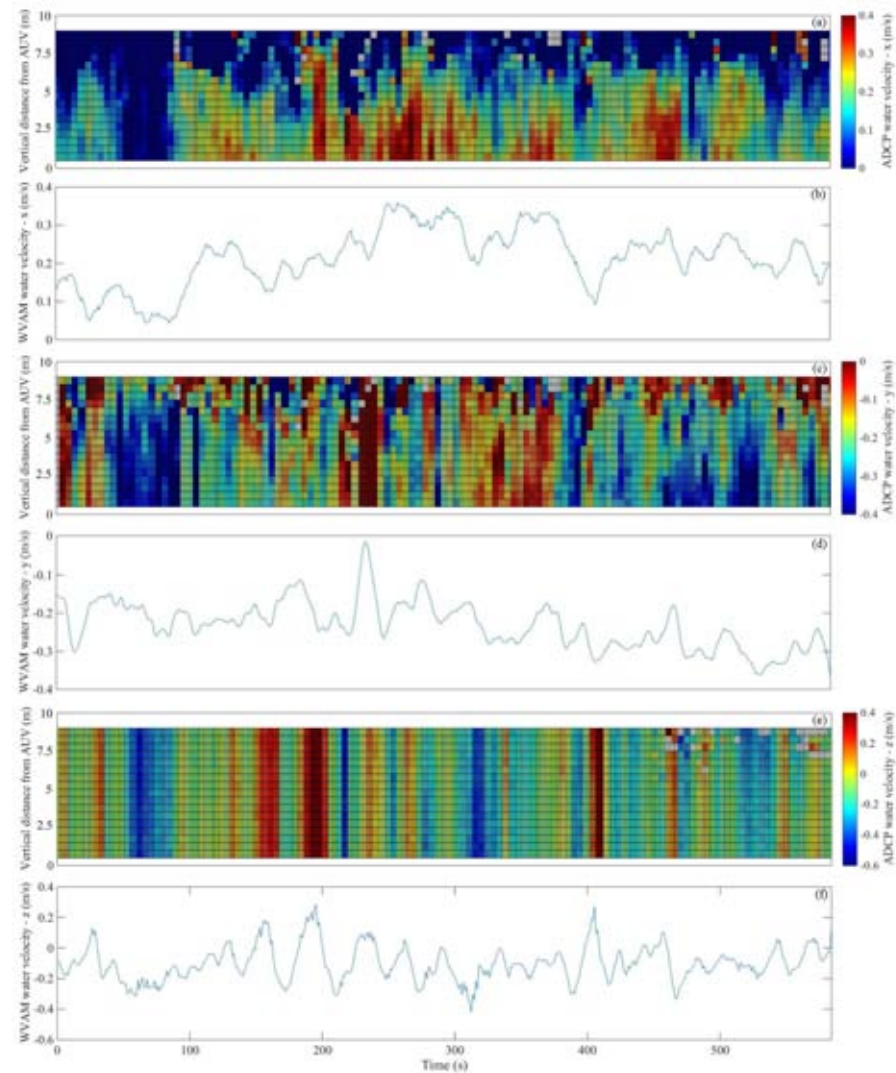
Validation of the WVAM Method

Figures 5a, 5c, and 5e illustrate the variations of the ADCP-measured

water velocity components (i.e., velocities in x , y , and z directions, respectively) with the vertical distance from the AUV. Figures 5b, 5d, and 5f present the respective flow velocity components estimated with the WVAM method. The velocity data shown in Figure 5 were recorded during Run 1 (i.e., when the AUV was moving with the predominant tidal currents). As seen, the WVAM velocity estimates

FIGURE 5

Panels a, c, and e illustrate the ADCP-measured variations of the water column velocity components in x , y , and z directions (respectively) with the vertical distance from the AUV. The respective flow velocity components estimated by the WVAM method are presented in Panels b, d, and f. The illustrated velocity data were obtained from Run 1 when the AUV was moving with the predominant tidal currents.



well correlate with the ADCP measurements, especially around the bins closer to the vehicle.

The uncertainty of the water velocity measurements from the WVAM method compared to the ADCP results was quantified using Equation 2 that approximates the standard error (SE) with a percentage confidence of 99.7% (Devore, 2011).

$$SE = \frac{3}{\sqrt{n}} \sqrt{\frac{\sum_{t=1}^n (\bar{v}_{\text{water(ADCP)}} - \bar{v}_{\text{water(WVAM)}})^2}{n}} \quad (2)$$

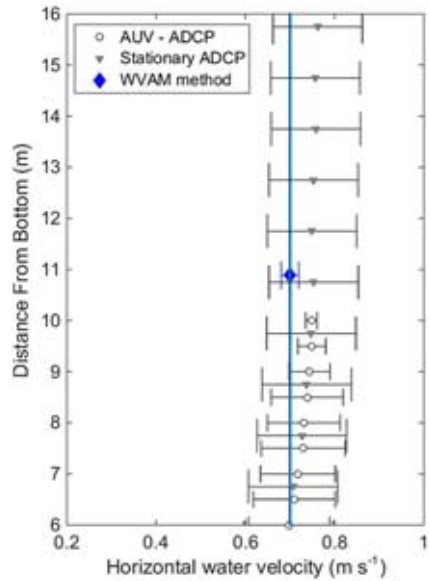
where $\bar{v}_{\text{water(ADCP)}}$ is the water velocity measured using the ADCP, $\bar{v}_{\text{water(WVAM)}}$ is the water velocity calculated using the WVAM method, and n is the number of time steps. The SEs for the velocity components in the x , y , and z directions for the first run were ± 0.068 , ± 0.017 , and $\pm 0.045 \text{ m s}^{-1}$, respectively. These numbers represent the difference between WVAM and ADCP velocity predictions in each of the three directions, with the greatest error seen in the x direction.

It is evident from these plots that the WVAM method provides a good replication of the flow velocities measured using the onboard ADCP. Since the vehicle was moving with the predominant tidal flow direction, a positive water velocity along the x direction is seen in Figures 6a and 6b. The negative water velocity component in the y direction (Figures 6c and 6d) indicates that the transverse flow direction is from northeast side to southwest. Although the transverse water velocity does not follow the ADCP velocity trend for some periods, the averaged velocities are in favorable agreement. However, further studies will be conducted to investigate the reasons for this. The best replica between the WVAM and ADCP velocities is seen in the vertical velocity component. The largest mismatches in the vertical velocities are seen at the peaks. The hydrodynamic coefficients of the simulation model estimated using the basic system identification method were only valid for small angles of incidence of the vehicle, where the coefficients are in their linear ranges. Therefore, as the yaw and pitch angle fluctuations become larger, the accuracy of the simulation model decreases, adversely affecting the WVAM velocity prediction (Randeni et al., 2015a). The disparity at peaks of the vertical velocity component is due to the hydrodynamic coefficients exceeding their linear ranges causing a reduction in the accuracy of the simulation model.

A recent study (Green, 2015) compared the water velocity measurements obtained from the *Gavia* AUV's onboard ADCP with a stationary ADCP moored to the seabed. This investigation was carried out in the same test location (i.e., Tamar estuary) with the same *Gavia*-class AUV as used in this study. Green (2015) found very good agreements between the AUV-mounted and stationary ADCP measurements. In addition, the stationary ADCP data set was used to validate estimates with the WVAM for a period when the AUV was in close proximity to the moored ADCP. Similar to the findings from the AUV-ADCP and stationary ADCP comparison, the velocities between WVAM and stationary ADCP showed a good agreement with differences of 0.05 , 0.08 , and 0.01 m s^{-1} for the respective velocity components in the x , y , and z directions (see Figure 6).

FIGURE 6

Comparison of the horizontal water velocities obtained from the WVAM method, stationary ADCP, and the AUV-fixed ADCP; modified from Green (2015).



Accuracy of the WVAM Method With the Level of Turbulence

Runs 1–3 and 6–9 were conducted in lower turbulent environments, with a vertical water velocity range of around -1 to 1 m s^{-1} compared to the Runs 4 and 5, which were at vertical water velocity range of -2 to 0.5 m s^{-1} . Due to the developing flood tide, the level of turbulence increased gradually with each run. The averaged fluctuations of the vehicle's yaw angle, pitch angle, and surge speed from the target values are given in Table 1. If the AUV's control system is capable of guiding the vehicle accurately along the prescribed path in turbulent environments, these values would be close to zero. As seen from Table 1, the fluctuations have raised with the increasing level of turbulence.

The SEs of the WVAM water velocity predictions compared to the ADCP measurements for each run are presented in Table 1 and Figure 7.

TABLE 1

SEs of the water velocity components determined from the WVAM method compared to the onboard ADCP measurements and the associated averaged deviations for the prescribed parameters.

Run Number	SE			Averaged Deviation From the Prescribed Value		
	<i>u</i>	<i>v</i>	<i>w</i>	Yaw Angle (Degrees)	Pitch Angle (Degrees)	Surge Speed (m s ⁻¹)
1	0.068	0.017	0.045	±1.5	±3.6	±0.2
2	0.029	0.153	0.075	±17.4	±7.1	±0.6
3	0.041	0.095	0.108	±3.5	±7.5	±0.7
4	0.063	0.061	0.241	±2.8	±9.2	±1.6
5	0.035	0.079	0.191	±5.6	±9.7	±1.6
6	0.042	0.063	0.052	±3.1	±3.1	±0.1
7	0.048	0.058	0.067	±2.6	±6.4	±0.3
8	0.025	0.104	0.092	±14.5	±7.4	±0.4
9	0.054	0.082	0.097	±5.8	±7.5	±0.6

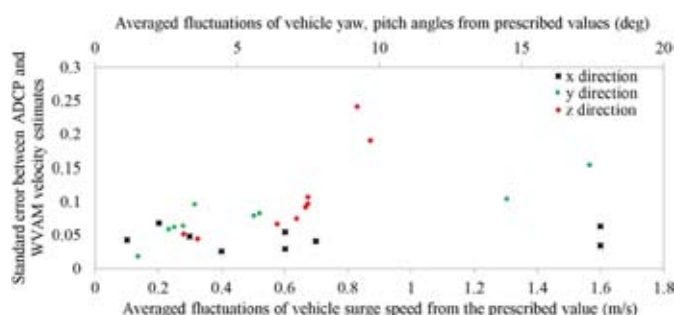
The uncertainties of the vertical and transverse water velocity estimates increase with the averaged fluctuations of the pitch and yaw angles, respectively. For example, in Run 2, the averaged deviation of the yaw angle is around ±17°, and the SE of the transverse velocity prediction is much larger than for Run 1 (i.e., 0.153 m s⁻¹). Run 1 has a smaller deviation of the yaw angle of around ±1.5°, which results in a much smaller uncertainty in the vicinity of 0.017 m s⁻¹. A similar outcome is seen in the vertical water

velocity component. In Run 9, the averaged deviation of the pitch angle is ±7.5° giving an SE in the vertical water velocity prediction of around 0.1 m s⁻¹. However, in Run 6, the deviation of the pitch angle is comparatively lower at ±3.1° resulting in a smaller SE for the velocity of around 0.05 m s⁻¹. Although the tides were not fully developed during the Runs 2 and 8, the yaw angle deviations are relatively higher. This could be as a result of a strong crosscurrent acting on the vehicle at the particular water height.

Generally, an SE between the ADCP and WVAM that results up to 0.1 m s⁻¹ is acceptable as the uncertainty of the measurements from an AUV-mounted ADCP is of similar magnitude (Fong & Jones, 2006). The threshold averaged deviation of the pitch and yaw angles that provide the water column velocities with an SE below 0.1 m s⁻¹ is around 7°–8°. Above this threshold angle, the hydrodynamic coefficients usually become nonlinear. The hydrodynamic coefficients estimated for the simulation model using the curve fitting method are only valid for small angles of incidence of the vehicle, that is, when the coefficients are in the linear range (Randeni et al., 2015b). Therefore, when the pitch and yaw angles are above the linear range, the accuracy of the simulation model decreases, and the uncertainty of the vertical and transverse water velocity components obtained from the WVAM method increases. Hence, the WVAM method, in its current state, is less accurate in determining transverse and vertical water velocities in high turbulent environments.

FIGURE 7

The variations of the WVAM method's SEs with the averaged fluctuations of the vehicle surge speed and yaw and pitch angles from the prescribed values. The water velocity components in *x*, *y*, and *z* directions correspond with the surge speed, yaw angle, and pitch angle, respectively.



The accuracy of the water velocity component in the x direction remains generally the same for all the runs regardless of the averaged fluctuations of the surge speed (see Figure 7). During the development of the simulation model, the hydrodynamic coefficients dominating the motion in the x direction were estimated for a propeller speed range of 525–825 RPM (i.e., an approximate vehicle speed range of 1.43 to 2.46 m s^{-1} in a calm water environment). During this study, the AUV field runs were conducted at 700 RPM providing a mean forward speed of around 2.04 m s^{-1} in calm water conditions with a standard deviation of 0.01 m s^{-1} . The observed speed during the runs varied as much as $\pm 1.6 \text{ m s}^{-1}$ from the calm water speed of 2.04 m s^{-1} , especially during Runs 5 and 6 due to the strong drag on the vehicle imparted by the strong tidal currents. Although the actual vehicle speed deviated from the simulated speed, the prescribed propeller speed of 700 RPM provides a calm water simulated speed of around 2.04 m s^{-1} , which is within the identified forward speed range of 1.43–2.46 m s^{-1} . Therefore, the simulation model provided an accurate representation of the forward speed of the AUV in calm water. It can thus be concluded that the SE results between the WVAM and ADCP in the x direction generally remained unrelated to the turbulence level of the water column.

Applicability of the WVAM Method for Blue Water Navigation

The outcome of the above analysis shows that the WVAM method captures the water velocity up to around 1–1.5 m s^{-1} with an acceptable accuracy. Therefore, it can be used to aid the INS navigation solution for the situa-

tions discussed in Figure 1 without further improvements. However, the threshold of the WVAM method in measuring velocity components in the y and z directions can be improved for higher turbulent environments by a more accurate estimation of the vehicle hydrodynamic coefficients within their linear as well as nonlinear ranges. Captive model experiments and computational fluid dynamic (CFD) simulations are capable of determining the nonlinear hydrodynamic coefficients of AUVs with a greater accuracy; albeit the associated experimental costs and the computational times are higher (Randeni et al., 2015c). The coefficients obtained from such methods are only valid for the vehicle configuration that was tested during the experiments. However, the arrangements of modular AUVs change with the mission and addition/removal of payloads occurs frequently. As it is not feasible to conduct cost-intensive experiments and simulations for each alteration, estimating the nonlinear hydrodynamic coefficients using a system identification method such as least squares optimization is more suitable (Ljung, 1998).

Ascend and Descend Parallel to Sea Currents

Gavia-class AUVs are underactuated vehicles (i.e., they have a lower number of actuators than the vehicle's DOF). Its actuator control is limited to the surge speed, roll angle, pitch angle, and yaw angle of the vehicle. Depth and transverse displacement is obtained by changing the pitch and yaw angles, respectively. Generally, underactuated underwater vehicles are difficult to control when external forces such as currents are acting parallel to the underactuated directions (Aguiar & Pascoal, 2007). For example, the control system of the *Gavia* AUV strug-

gles to maintain the trajectory when crosscurrents are acting perpendicular to the AUV's motion.

In such situations, the vehicle tends to oscillate, resulting in higher unbound drifts in the INS navigation solution compared to normal operations, unless properly counteracted with the velocity over ground measurements from the DVL bottom track. These drift fluctuations are considerably less when the vehicle is traveling in line with the currents (i.e., currents are acting along the x axis of the AUV). A positive outcome of this study is that water column velocities in x direction obtained from the WVAM method were accurate for all turbulence levels present during the field campaign in the Tamar estuary. The results suggest that deep water ascents and descents should be carried out with the vehicle in line with the currents to improve the accuracy of the WVAM-INS navigation solution (i.e., as seen in Figure 5, the accuracy is higher in the flow measurements along the x direction compared to y direction), although this may be challenging in unknown environments. Occasionally, a reconnaissance mission may be conducted over the test site prior to the deep dive to ensure the safety of the vehicle and to adjust instrument settings, for instance, sonar parameters of the multibeam unit. In such cases, the main flow direction could be simply and accurately determined using the WVAM method during this mission, and an algorithm can be created to autonomously decide the direction of ascent/descent.

Velocity Overground Measurements for the WVAM Method

During the vehicle operations outlined in Figure 1, continuous velocity measurements of the AUV relative to

the ground are not obtainable from DVL bottom tracking to assist the INS navigation solution. Therefore, the INS could be aided with velocity estimates from secondary instruments or methods, although this does not represent typical operations. An accurate simulation model is able to predict the vehicle velocities in real time when the control commands of the AUV are provided (Hegrenæs & Hallingstad, 2011). The hydrodynamic coefficients of simulation models generally represent the calm water operational condition of the AUV. Therefore, vehicle drift resulting from currents in the water column will not be included in the velocity predictions, causing inaccuracies in the AUV position estimated by the INS (Augenstein & Rock, 2008; Hegrenæs & Berglund, 2009). The results discussed in the above sections show that the WVAM method could be successfully utilized to determine the water column velocities that can be used in conjunction with model-predicted vehicle velocities to aid the INS navigation solution.

A disadvantage of the WVAM method is that it requires an estimation of the vehicle velocity relative to the ground in order to measure the water column velocities. The position and velocity estimates of the vehicle can be determined using acoustic transponders (i.e., ultra short baseline or long baseline), albeit with an infrequent update rate. The intermittent velocity updates from the transponders will be used for the WVAM to determine the water column velocities, and the estimated flow measurements will then be assumed to remain constant until the next reliable velocity update is received.

As an alternative to the velocity estimates from acoustic transponders, the velocity of the AUV relative to the ground can be computed in a prop-

agative manner starting from the initial measurements taken at the beginning of the process when DVL bottom track or GPS data are available. That is, the initial vehicle velocity measurements will be used to determine the water column velocities using the WVAM method and will be used in conjunction with the velocities predicted from the simulation model to recalculate the vehicle velocities relative to the ground. The initially measured and calculated vehicle velocities will be compared, and, if the correlation is satisfied, the computation will be iteratively updated by obtaining the velocity solution of the current time stamp using the previous time stamp's velocity information. However, further measures should be taken to reduce the error accumulation. The INS navigation solution is more robust and less prone to errors when velocity overground readings from various sensors and estimates are considered, for example, by using a Kalman filter, since the signal outputs from individual sensors can be discontinuous (Hegrenæs & Hallingstad, 2011). Thus, the INS aided with the vehicle velocity estimates determined from the proposed method is expected to provide a better localization performance.

Conclusions

The WVAM method is a non-acoustic technique to determine the water velocity components of a turbulent water column using the motion response of an AUV. The accuracy of the WVAM method was examined at different turbulence levels of the water column. Nine AUV runs were conducted along the same track line at different times in the tidal cycle in the Tamar estuary in Tasmania, Australia. Typically, when an AUV

undertakes missions in rough water environments, the pitch and yaw angles of the vehicle fluctuate around the target values due to the inability of the AUV's dynamic controller to adequately compensate for the external disturbing forces. The greater the turbulence level of the water, the larger the fluctuations. The estimated water velocity components in the y and z directions using the WVAM method agreed well with the experimental measurements obtained from the AUV's onboard ADCP for low turbulent conditions (with a vertical water velocity range of around -1 to $+1$ m s $^{-1}$), where the averaged deviations of the vehicle's pitch and yaw angles are below 7° – 8° . The correlation reduced when the averaged deviations were above 7° – 8° . The accuracy of the water velocity component in the x direction remained generally the same for all the runs regardless of the turbulence level of the water column.

The hydrodynamic coefficients for the simulation model utilized in the WVAM method were determined using a curve fitting technique. These estimated coefficients were only valid for small angles of incidence of the vehicle, where the coefficients are within their linear range. Therefore, as the pitch and yaw angle fluctuations become larger, the accuracy of the simulation model decreases adversely affecting the prediction of the vertical and transverse water velocity components obtained from the WVAM method. During the AUV missions, the vehicle speed remained within the identified forward speed range of 1.43–2.46 m s $^{-1}$. Therefore, the simulation model was able to provide an accurate prediction of the forward speed of the vehicle enabling the WVAM method to accurately determine the water velocities in the x direction.

The WVAM method is capable of capturing the velocity up to around $1\text{--}1.5 \text{ m s}^{-1}$ with an acceptable accuracy. Therefore, it could be incorporated to aid the INS navigation solution without further improvements for situations where the DVL bottom track is intermittently or completely unavailable or ineffective. However, the accuracy of the method will be increased by upgrading the simulation model to replicate the motion response of the vehicle in both the linear and nonlinear ranges.

Acknowledgments

This study was partially funded through the Research Enhancement Grant Scheme of the University of Tasmania (UTAS). The authors would like to thank Jeff Watts, Nathan Kemp, and Isak Bowden-Floyd at the Australian Maritime College, UTAS, for their support during the AUV field experiments. The authors also thank Helgi Porgilsson (Senior Systems Engineer at Teledyne Gavia) and Hordur Johannsson (Senior Software Engineer at Teledyne Gavia) for the continued technical support and assistance.

Corresponding Author

Supun A. T. Randeni P.
Locked Bag 1395,
Launceston, TAS 7250, Australia
Email: Supun.Randeni@utas.edu.au

References

- Aguiar**, A.P., & Pascoal, A.M. 2007. Dynamic positioning and way-point tracking of underactuated AUVs in the presence of ocean currents. *Int J Control.* 80(7):1092-108. Available at: <http://dx.doi.org/10.1080/00207170701268882>.
- Augenstein**, S., & Rock, S. 2008. Estimating inertial position and current in the midwater. Paper presented at the OCEANS 2008.
- Quebec City, Canada: IEEE. Available at: <http://dx.doi.org/10.1109/OCEANS.2008.5152057>.
- Curtin**, T.B., Bellingsham, J.G., Catipovic, J., & Webb, D. 1993. Autonomous oceanographic sampling networks. *Oceanography.* 6(3): 86-94. Available at: <http://dx.doi.org/10.5670/oceanog.1993.03>.
- Devore**, J. 2011. Probability and Statistics for Engineering and the Sciences. Cengage Learning.
- Fong**, D.A., & Jones, N.L. 2006. Evaluation of AUV-based ADCP measurements. *Limnol Oceanogr-Meth.* 4(3):58-67. Available at: <http://dx.doi.org/10.4319/lom.2006.4.58>.
- Grasmueck**, M., Eberli, G.P., Viggiano, D.A., Correa, T., Rathwell, G., & Luo, J. (2006). Autonomous underwater vehicle (AUV) mapping reveals coral mound distribution, morphology, and oceanography in deep water of the Straits of Florida. *Geophys Res Lett.* 33:L23616. Available at: <http://dx.doi.org/10.1029/2006GL027734>.
- Green**, S.M. 2015. Tidal Site Characterisation Using Stationary and AUV-Mounted ADCPs in a Highly Dynamic Environment. Launceston, Tasmania, Australia: (Bachelor of Engineering), Australian Maritime College, University of Tasmania, Launceston.
- Hegrenæs**, Ø., & Berglund, E. 2009. Doppler water-track aided inertial navigation for autonomous underwater vehicle. Paper presented at the OCEANS 2009-EUROPE. Bremen, Germany: IEEE. Available at: <http://dx.doi.org/10.1109/OCEANSE.2009.5278307>.
- Hegrenæs**, Ø., Berglund, E., & Hallingstad, O. 2008. Model-aided inertial navigation for underwater vehicles. Paper presented at the IEEE International Conference on Robotics and Automation, 2008. ICRA 2008. Pasadena, California, USA: IEEE. Available at: <http://dx.doi.org/10.1109/ROBOT.2008.4543346>.
- Hegrenæs**, Ø., & Hallingstad, O. 2011. Model-aided INS with sea current estimation for robust underwater navigation. *IEEE J Oceanic Eng.* 36(2):316-37. Available at: <http://dx.doi.org/10.1109/JOE.2010.2100470>.
- Hildebrandt**, M., & Hilljegerdes, J. 2010. Design of a versatile AUV for high precision visual mapping and algorithm evaluation. Paper presented at the Autonomous Underwater Vehicles (AUV), 2010 IEEE/OES. Available at: <http://dx.doi.org/10.1109/AUV.2010.5779663>. Monterey, California, USA: IEEE.
- Kim**, K., & Ura, T. 2003. Fuel-optimal guidance and tracking control of AUV under current interaction. Paper presented at the The Thirteenth International Offshore and Polar Engineering Conference. San Diego, California, USA: IEEE.
- Lewis**, E.V. 1988. Principles of Naval Architecture: Motions in Waves and Controllability (Vol. 3). Jersey City, New Jersey, USA: Society of Naval Architects & Marine Engineers.
- Ljung**, L. 1998. System identification. New Jersey, USA: Springer. Available at: http://dx.doi.org/10.1007/978-1-4612-1768-8_11.
- Paull**, L., Saeedi, S., Seto, M., & Li, H. 2014. AUV navigation and localization: A review. *IEEE J Oceanic Eng.* 39(1):131-49. Available at: <http://dx.doi.org/10.1109/JOE.2013.2278891>.
- Randeni**, S.A.T., Forrest, A.L., Cossu, R., Leong, Z.Q., & Ranmuthugala, D. 2015a. Estimating flow velocities of the water column using the motion response of an autonomous underwater vehicle (AUV). Paper presented at the OCEANS '15 MTS/IEEE, Washington, DC.
- Randeni**, S.A.T., Forrest, A.L., Cossu, R., Leong, Z.Q., Zarruk, G.A., & Ranmuthugala, D. 2015b. Determining the horizontal and vertical water velocity components of a turbulent water column using the motion response of an autonomous underwater vehicle. *J Atmos Ocean Tech.*
- Randeni**, S.A.T., Leong, Z.Q., Ranmuthugala, D., Forrest, A.L., & Duffy, J. 2015c. Numerical investigation of the hydrodynamic interaction between two underwater bodies in relative motion. *Appl Ocean Res.* 51(0):14-24. Available at: <http://dx.doi.org/10.1016/j.apor.2015.02.006>.
- Simpson**, M.R. 2001. Discharge measurements using a broad-band acoustic Doppler current profiler. Sacramento, California, USA: U.S. Department of the Interior, U.S. Geological Survey.

Coupled Modeling of Hydrodynamics and Sound in Coastal Ocean for Renewable Ocean Energy Development

AUTHORS

Wen Long
 Ki Won Jung
 Zhaoqing Yang
 Andrea Copping
 Z. Daniel Deng
 Pacific Northwest
 National Laboratory

Introduction

Renewable energy generated from renewable offshore resources—from waves, tidal streams, and ocean currents and from offshore wind energy—has the potential to contribute to the U.S. low carbon “all of the above” portfolio of renewable energy sources. These devices are commonly deployed in estuaries and coastal waters within 32 km of the coastline. However, stakeholders and regulators have concerns that the extraction of marine renewable energy may pose a risk to the well-being of marine mammals and fish (Bailey, 2012; NRC, 2005). One of the potential risks is from the addition of unnatural sound generated by energy devices that could injure, disorient, or alter the movements of marine animals. The effects of sound from wave and tidal stream devices and sound from pile driving for offshore wind turbines are some of the most significant concerns.

There have been efforts to understand the sound propagation from the anthropogenic noise sources in range-dependent (e.g., varying bathymetry) settings. Ray tracing was used to study

ABSTRACT

The rapid growth of renewable offshore energy development has raised concerns that underwater noise from construction and operation of offshore devices may interfere with communication of marine animals. An underwater sound model was developed to simulate sound propagation from marine and hydrokinetic energy (MHK) devices or offshore wind (OSW) energy platforms. Finite difference methods were developed to solve the 3-D Helmholtz equation for sound propagation in the coastal environment. A 3-D sparse matrix solver with complex coefficients was formed for solving the resulting acoustic pressure field. The complex shifted Laplacian preconditioner (CSLP) method was applied to solve the matrix system iteratively with Message Passing Interface (MPI) parallelization using a high-performance cluster. The sound model was then coupled with the Finite Volume Community Ocean Model (FVCOM) for simulating sound propagation generated by human activities, such as construction of OSW turbines or tidal stream turbine operations, in a range-dependent setting. As a proof of concept, the validation of the solver is tested with an ideal case against two other methods, and its application is then presented for two coastal wedge problems. This sound model can be useful for evaluating impacts on marine mammals due to deployment of MHK devices and OSW energy platforms.

Keywords: sound, coastal ocean, renewable ocean energy, coupling, Helmholtz equation

the impact of the noise from the seismic air guns on fish behavior (Hovem et al., 2012) and to estimate the received sonar signals by the northern bottlenose whales (Miller et al., 2015). Parabolic equation (PE) was also utilized to estimate the sound exposure level to seals around the pile driving location near a wind farm construction site (Hastie et al., 2015). DeRuiter et al. (2006) used both ray tracing and PE to model acoustic propagation of air-gun array pulses and compared the results with the recorded signals by tag-equipped sperm whales. Although a range dependency was considered in terms of bathymetry and a

speed of sound profile, it was mostly 2-D variation based on axis symmetry, and none of the previous works considered the 3-D heterogeneity in salinity, temperature, sound speed, and bathymetry. This becomes important when there are river plumes in the coastal area of interest, because the freshwater can alter both salinity and temperature, both of which affect sound speed in water.

Sound transmission is closely related to ocean water density, which is in turn dependent on water temperature, salinity, and depth (pressure) (Lurton, 2002). Typical vertical density stratification due to temperature and salinity

in the ocean was described by Talley et al. (2011). A simple regression of the data provides sound speed C (m/s) as (Medwin, 1975)

$$C = 1449.2 + 4.6T - 0.055T^2 + 0.00029T^3 + (1.34 - 0.01T)(S - 35) + 0.016D \quad (1)$$

where S is salinity in practical salinity unit (PSU), T is temperature in degrees Celsius, and D is depth in meters. For typical deep ocean areas, the main contribution to variation of sound speed is due to temperature stratification and pressure (depth). This relationship sets up a minimum speed at around 700-m depth. As an example, sound generated at about 1,100-m water depth propagates at small angles around the horizontal direction and is refracted up and down around the same depth level, resulting in horizontal propagation over very long distances. However, in coastal zones only with a consideration of depth, this variability in C becomes less than 5 m/s because of its shallow depth less than 200 m. Instead, in coastal zones, where salinity could vary from 0 to 35 PSU, the variation of C due to salinity could be as much as ± 50 m/s. Moreover, sound transmission in coastal waters is temporally and spatially more variable than that in the open ocean, for example, due to seasonal influences of river plumes, effects of meteorological wind stress and heat fluxes, acoustic scattering from internal waves, and reflections of sound from complex coastal geometries. An advanced model can be used to account for this variability to accurately predict sound fields. However, coupled hydrodynamic and acoustic models have not been developed because of the intensive computational resources needed.

We improved the ability to predict sound propagation in coastal regions by coupling of the 3-D ocean hydrodynamic circulation model FVCOM (Finite Volume Community Ocean Model; Chen et al., 2003, 2006, 2007; Lai et al., 2010; Yang et al., 2015), which resolves the variations of water density and sea surface elevation, with our 3-D acoustic model that solves underwater sound transmission loss (TL), as well as reflection from lateral, bottom, and surface boundaries and refraction due to varying density fields.

Hydrodynamic Model

FVCOM solves the continuity and momentum equations using the finite-volume method and sigma-stretched coordinate transformation in the vertical direction.

Formulation of Hydrodynamics in FVCOM

The momentum equations of FVCOM in the horizontal directions have the general form (Chen et al., 2003, 2006, 2007; Lai et al., 2010) of

$$\frac{\partial uD}{\partial t} + \frac{\partial u^2 D}{\partial x} + \frac{\partial uvD}{\partial y} + \frac{\partial u\omega}{\partial \sigma} - fvD = -\frac{D}{\rho_o} \frac{\partial p}{\partial x} + \frac{1}{D} \frac{\partial}{\partial \sigma} \left(K_m \frac{\partial u}{\partial \sigma} \right) + DF_x \quad (2)$$

$$\frac{\partial vD}{\partial t} + \frac{\partial uvD}{\partial x} + \frac{\partial v^2 D}{\partial y} + \frac{\partial v\omega}{\partial \sigma} + fuD = -\frac{D}{\rho_o} \frac{\partial p}{\partial y} + \frac{1}{D} \frac{\partial}{\partial \sigma} \left(K_m \frac{\partial v}{\partial \sigma} \right) + DF_y \quad (3)$$

where x , y , and σ are the east, north, and vertical axes in the sigma coordinates; u , v , and ω are the three velocity components in the x , y , and σ directions; D is the total water depth; F_x and F_y are the horizontal momentum diffusivity terms in the x and y directions; K_m is the vertical eddy viscosity coefficient; ρ is water density; p is pressure; and f is the Coriolis parameter. σ is the stretched vertical coordinate system based on an algebraic transformation from vertical Cartesian coordinate z .

$$\sigma = \frac{z - \xi}{D}, \quad (4)$$

with $\xi(t, x, y)$ being the surface elevation and $D = h + \xi$, where $h(x, y)$ is still water depth. The surface and bottom boundaries are corresponding to $\sigma = 0$ and $\sigma = -1$, respectively. Similarly, the temperature $T(x, y, \sigma, t)$ and salinity $S(x, y, \sigma, t)$ are solved in 3-D using the transport equations below.

$$\frac{\partial TD}{\partial t} + \frac{\partial u TD}{\partial x} + \frac{\partial v TD}{\partial y} + \frac{\partial \omega T}{\partial \sigma} = \frac{1}{D} \frac{\partial}{\partial \sigma} \left(K_T \frac{\partial T}{\partial \sigma} \right) + D \hat{H} + D F_T \quad (5)$$

$$\frac{\partial SD}{\partial t} + \frac{\partial u SD}{\partial x} + \frac{\partial v SD}{\partial y} + \frac{\partial \omega S}{\partial \sigma} = \frac{1}{D} \frac{\partial}{\partial \sigma} \left(K_S \frac{\partial S}{\partial \sigma} \right) + D F_S \quad (6)$$

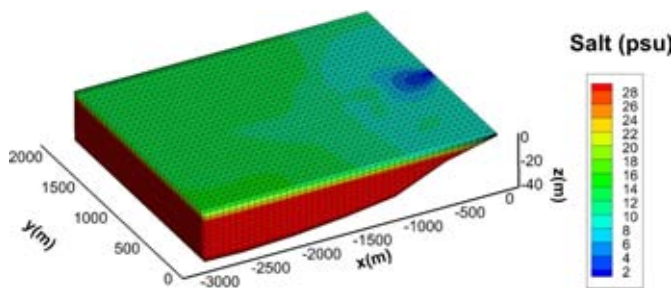
where $\hat{H}(x, y)$ is the heating source/sink for a given vertical location; F_T and F_S are the horizontal turbulent eddy diffusion terms for temperature and salinity, respectively; K_T and K_S are for vertical eddy diffusivities of temperature and salinity. The above equations are solved using finite volume integration based on spatial discretization with triangular meshes in horizontal plane (x, y) and fixed σ layers in vertical direction. For derivations of the discretized system, readers are referred to the publications on FVCOM (Chen et al., 2003, 2006, 2007; Lai et al., 2010) for details.

Application of FVCOM for a Coastal Wedge Case with a River Plume

A typical coastal wedge (idealized coastal domain with a wedge shape for the water part) application is depicted in Figure 1. The water depth at the shoreline (right-hand side) is 2 m, and the shoreline is about 2 km long. The cross-shore bathymetry is described as a piece-wise linear sloping bottom with maximum depth at the open boundary being 44 m. A river discharge of 150 m/s is placed at the center of the coastline, delivering a freshwater plume to the coastal zone. For such a relatively simple geometry, an unstructured grid mesh is chosen such that all the triangular nodes collapse into a structured mesh. The FVCOM model was run for 39 days of simulation with time step $\Delta t = 1$ s from initially evenly distributed salinity of 30 PSU and quiescent flow field (i.e., $(u, v, \omega) = (0, 0, 0)$). Salinity distribution at the last hour of the 39-day simulation is plotted using colored contours (Figure 1). For simplicity, Coriolis forcing is set to zero, and temperature simulation is disabled.

FIGURE 1

Coastal wedge simulation of river plume. (Color version of figures are available online at: <http://www.ingentaconnect.com/content/mits/mitsj/2016/00000050/00000002>.)



Coastal Acoustic Model

Mathematical Description of Sound in Coastal Oceans

In Cartesian coordinates (x, y, z) , the pressure disturbance caused by sound in ocean $p(x, y, z, t)$ is governed by the 3-D wave equation below.

$$\frac{\partial^2 p}{\partial t^2} - C^2 \nabla^2 p = F(x, y, z, t) \quad (7)$$

where $C(x, y, z)$ is the sound speed (unit: m/s) and F is the sound source strength. For a given frequency f , the pressure p can be written in harmonic form (using complex numbers, and the physical pressure will always be the real part of the complex number)

$$p(x, y, z, t) = \hat{p}(x, y, z) e^{i\bar{\omega}t} \quad (8)$$

Substituting this harmonic equation into equation (7), the Helmholtz equation is obtained as

$$\nabla^2 \hat{p} + k^2 \hat{p} = -\frac{1}{C^2} \hat{F} \quad (9)$$

where $F = \hat{F} e^{i\bar{\omega}t}$ and $\bar{\omega} = 2\pi f$ is the angular frequency and $k(x, y, z) = \frac{\bar{\omega}}{C}$ is the angular wave number. In coastal oceans, C and k are spatially variable due to the variation of temperature and salinity. For applications with attenuation, k^2 is replaced by $(1 - \alpha i)k^2$, where α is the attenuation coefficient and i is the notation for the imaginary part of a complex number.

Finite Difference Formulation

For implementation with a structured grid system of constant grid spacing $\Delta x, \Delta y, \Delta z$ in a 3-D regular box-shaped domain, denoting \hat{p} as indexed by (i, j, l) in x, y , and z directions, equation (9) can be discretized using the finite difference method as

$$\frac{(\hat{p}_{i-1,j,l} - 2\hat{p}_{i,j,l} + \hat{p}_{i+1,j,l})}{\Delta x^2} + \frac{(\hat{p}_{i,j-1,l} - 2\hat{p}_{i,j,l} + \hat{p}_{i,j+1,l})}{\Delta y^2} + \frac{(\hat{p}_{i,j,l-1} - 2\hat{p}_{i,j,l} + \hat{p}_{i,j,l+1})}{\Delta z^2} + k^2 \hat{p}_{i,j,l} = -\frac{1}{C^2} \hat{F}_{i,j,l} \quad (10)$$

where $i = 2 \dots, M - 1, j = 2 \dots, N - 1, l = 2 \dots, L - 1$ and M, N , and L are the number of grid points in x, y , and z directions, respectively. In addition, the surface boundary condition is $\hat{p}_{i,j,l=1} = 0$. Equation (10) can also be arranged in the following form for all \hat{p} values.

$$A\hat{p} = b \quad (11)$$

where A is an $M \times N \times L$ by $M \times N \times L$ sparse matrix.

Iterative Helmholtz Solver Based on Complex Shifted Laplacian Preconditioner Method

The matrix A in equation (11) is typically a very large sparse matrix of complex numbers. For high-frequency sound and large domain, the matrix equation (11) becomes difficult to solve directly. The Complex Shifted Laplacian Preconditioner (CSLP) method by Vuik et al. (2003) with either Bi-CGSTAB (Van de Vorst, 1992) or GMRES (Saad & Schultz, 1986) is used for this research. The CSLP method is based on construction of a preconditioning matrix M_P

$$M_P = B + (\beta_1 - i\beta_2)k^2 I \quad (12)$$

where I is the unit matrix and $B = A - k^2 I$. Instead of solving equation (11), the following left preconditioned equation is solved for \hat{p} .

$$M_P^{-1} A \hat{p} = M_P^{-1} b \quad (13)$$

β_1 and β_2 have been optimized for the best convergence rate. In our simulations, we used $\beta_1 = 0$ and $\beta_2 = 0.5$. M_P^{-1} was simply calculated using an SOR (Young, 1971) iteration method from M_P . To solve for \hat{p} from equation (13), the Krylov

TABLE 1

The test result is shown in terms of the iteration number (the running time is in the parentheses) as a function of wave number. The test was done using 16 CPUs and the restart value of 20 in GMRES.

Wave Number [1/m] (# of Grid Points)	(β_1, β_2)	(β_1, β_2)
	(1, 0.5)	(0, 0.5)
20 (35,937)	1,157 (0.432 s)	710 (0.257 s)
40 (274,625)	2,196 (7.62 s)	1,253 (4.51 s)
60 (912,673)	3,629 (49.1 s)	1,842 (26.1 s)
80 (2,146,689)	5,187 (175 s)	2,470 (84 s)
200 (33,076,161)	25,677 (17640 s)	6,318 (4160 s)

subspace methods called Bi-CGSTAB (Van de Vorst, 1992) or GMRES (Saad & Schultz, 1986) can be used. These two methods are implemented in the PETSc parallel computation library (version 3.6.0) (Balay et al., 2015).

The 3-D wedge case with heterogeneous wave number (Erlangga, 2005) is tested for the speed of computation with different wave numbers and number of grids on a high performance cluster with 16 CPUs (Intel Xeon CPU E5-2670 v3, 2.3 GHz). The results are given in Table 1. We found that $(\beta_1, \beta_2) = (0, 0.5)$ gave significantly better results than $(\beta_1, \beta_2) = (1, 0.5)$ that was reported in Erlangga et al. (2006).

Radiation Boundary Treatment

The radiation boundary is needed for open-domain simulations. However, because an imperfect radiation condition can reflect in the simulation domain of interest, a treatment that does not return the sound wave should be applied. This is implemented using the perfectly matched layer (PML) method (Chew & Weedon, 1994). Typically, this is done by placing 50 grids at the open boundary to absorb outgoing sound waves with a large damping term. Within the PML zone, k^2 in equation (9) is replaced by

$(1 - i\alpha)k^2$, where α is the attenuation factor in the PML zone, which is ramped up from zero at the physical domain boundary to 0.475 at the interior end of the PML layer. The external boundaries of the PML layers are terminated by the first-order Sommerfeld radiation boundary condition, defined as $\frac{d\hat{p}}{dn} = ik\hat{p}$, where n is the direction normal to the boundary.

Figure 2 depicts the \hat{p} solution (real part) of a 2-D simulation using the

PML layer in a homogeneous (uniform sound speed) domain with open boundaries. This demonstrates that our implementation of the PML layers has effectively removed artificial reflections from boundaries.

Validation of Acoustic Propagation Model

The finite difference scheme (equation (10)) along with the CSLP method (equation (13)) is tested on a wedge discussed by Lin et al. (2012) for validation. As the geometry is illustrated in Figure 3, the slope angle of the wedge is 2.86°, and the cross-shore distance is 4 km. The resulting water depth is 200 m at 4 km away from the shoreline. Here, because the validation is only focused on the TL across the wedge, the width of the wedge is reduced to 600 m. The water is assumed to be uniform in density with the sound speed $C = 1,500$ m/s. While the density of the seabed is assumed to be identical

FIGURE 2

2-D benchmark testing of PML for absorbing sound waves at the boundary. The real part of the pressure is shown in a 2-D homogeneous medium with the wave number of 0.4189 (1/m) with PML (not shown). The number of grid points per wavelength is set at 10. The point source is placed on the top line of the figure.

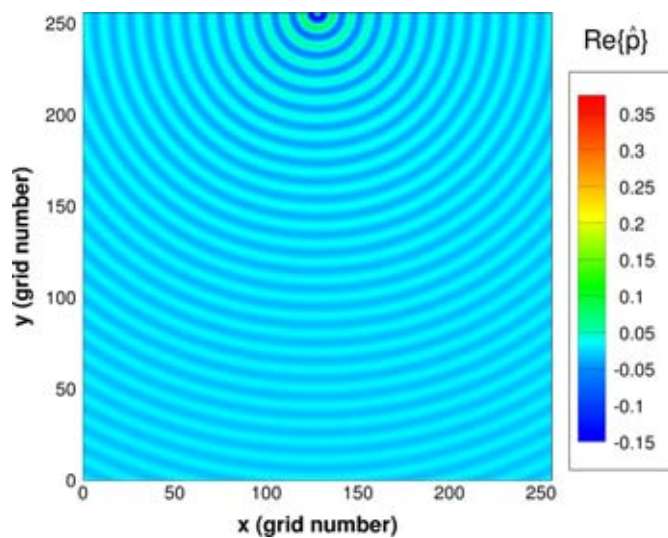
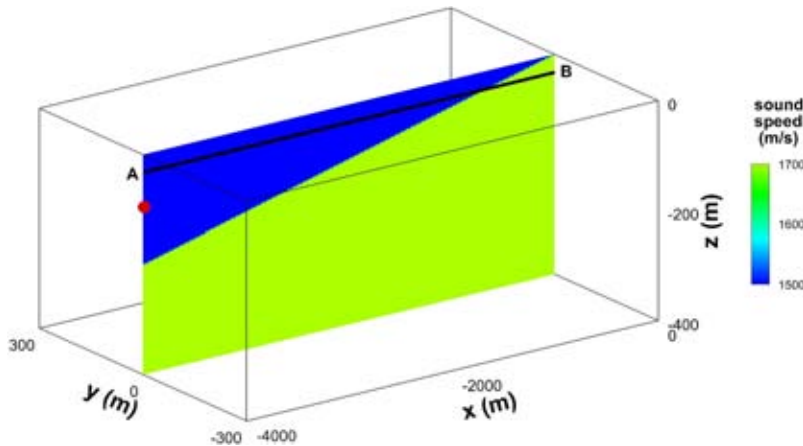


FIGURE 3

Geometry and sound speed profile of ASA wedge for the validation of the acoustic propagation model. The sound source location is indicated by a sphere below point A.



to that of the water, the seabed is modeled with a uniform sound speed $C = 1,700$ m/s. The attenuation in the seabed is set as 0.5 dB/wavelength. A point sound source with the frequency $f = 25$ Hz is placed at $x = -4,000$ m, $y = 0$ m, and $z = -100$ m (shown as the red sphere in Figure 3). In order to minimize the reflections from the boundaries surrounding the propagation medium, PML zones are added to the bottom and lateral boundaries. The grid sizes are defined as Δx and $\Delta y = 5$ m and $\Delta z = 2.5$ m.

Figure 4 shows the TL defined as

$$TL = -20 \log_{10} |\hat{p}| \quad (14)$$

at $z = -30$ m (70 m above the source) on the plane perpendicular to the shoreline as a function of distance from the source (i.e., along the line AB in Figure 3). Here, the pressure amplitude $|\hat{p}|$ is calibrated to become 1 Pa at the distance of 1 m from the source. For comparison, solutions using a PE-based RAMGEO (Collins, 1993) and using the image method (Deane & Buckingham, 1993) are pre-

method is presented for two idealized coastal wedge examples.

3-D ASA Wedge

The first example is for an idealized coastal water domain, which consists of shoreline coastal water confined in a wedge shape. Lin et al. (2012) discussed (called ASA wedge here) simulating the sound in such a domain using several PE-based methods. Here, a similar wedge domain is constructed and simulated. Figure 5 shows the straight wedge-shaped coastal zone with a shoreline depth of zero and an offshore depth of 200 m, a cross-shore distance of 4 km and an along-shore distance of 20 km. Different from the wedge case used for the validation, a unit sound source of frequency $f = 25$ Hz is placed at $x = -2,000$ m, $y = 0$ m, and $z = -50$ m (shown as the red sphere in Figure 5). The water is assumed to be uniform in density with a sound speed $C = 1,500$ m/s; the seabed is also depicted and extends to $z = -200$ m with the sound speed being $C = 1,700$ m/s. PML zones are

Application in Idealized Coastal Wedge Examples

The application of the acoustic propagation model based on 3-D Helmholtz equation with the CSLP

FIGURE 4

The TL curve along the line AB at $z = -30$ m. For comparison, the TL curves based on the image method (Deane & Buckingham, 1993) and a PE-based RAMGEO (Collins, 1993) are also presented.

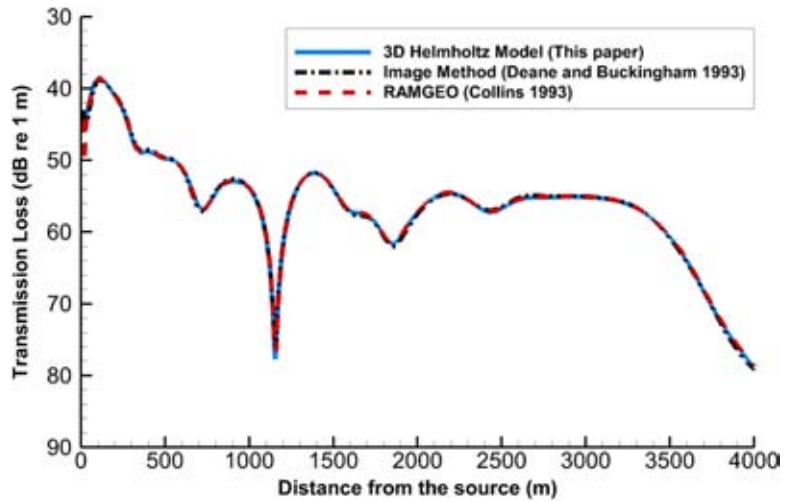
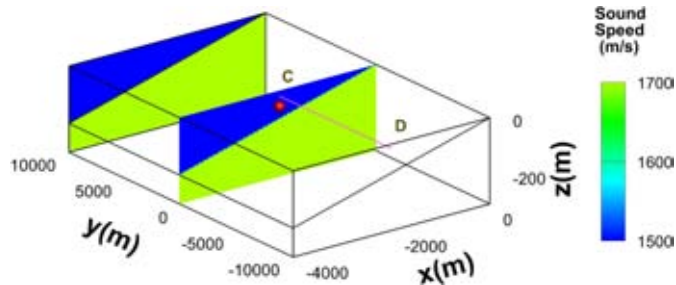


FIGURE 5

Geometry and sound speed profile of ASA wedge; sound source location is indicated by a sphere below point C.



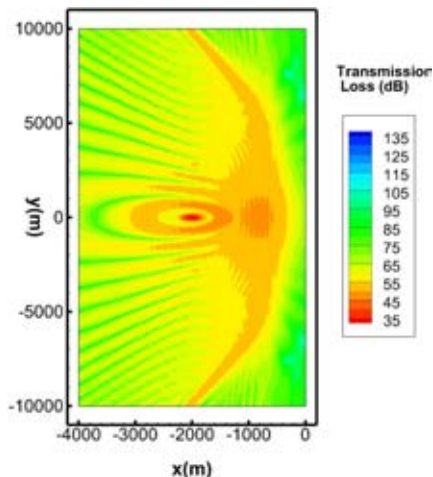
added for all lateral sides and bottom (not shown) for the simulation.

Figure 6 shows the computed TL at $z = -15$ m, that is, 15 m below surface. In order to obtain the TL value directly, \hat{p} is scaled by pressure at the distance of 1 m from the acoustic source. This results in a significant reflection from the shoreline. Figure 7 shows the vertical transect view of the xz plane at $y = 0$; the sound penetrates into the seabed below the sound source. There is also considerable penetration on the shoreline, whereas the area below the seabed offshore is sheltered.

Figure 8 shows the TL along line CD of Figure 5, which is located 15 m below the surface.

FIGURE 6

TL of xy plane at $z = -15$ m.



Coastal Wedge with a River Plume

The second example includes a coastal wedge with a river plume. The FVCOM model simulation of the coastal wedge (Figure 1) provided the salinity field at a constant temperature of 20°C. The grid size of the hydrodynamic model in Figure 1 is 62.5 m in horizontal plane with 10 vertical layers used for the water column discretization. We interpolated

the temperature and salinity fields onto finite difference grids to calculate the sound speed based on equation (1). A unit sound source of frequency $f = 100$ Hz is placed 5 m below the surface. The finite difference scheme formulation (equation (10)) is applied with a uniform grid size of Δx , Δy , and $\Delta z = 1.25$ m for the domain with the seabed extending below the maximum water depth (44 m deep at the open boundary) to $z = -144$ m with a sound speed $C = 2,500$ m/s below seabed. There are also 60 PML grids added in all lateral boundaries and that extended below the seabed for this test case. The surface is treated as a pressure-release boundary condition (zero acoustic pressure). The simulation is carried out using 25 parallel computer nodes, each with 24 cores. The model run-time is about 4 h for the simulation. Figure 9 shows the plane (xy) view of TL at $z = -5$ m, that is, the same depth as the source

FIGURE 7

TL of xz plane results at $y = 0$ m; the dark line indicates the seabed.

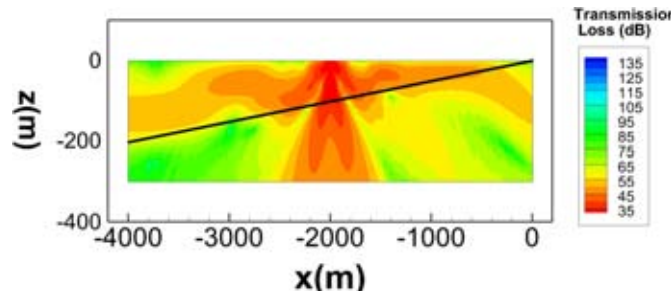


FIGURE 8

TL along line CD at $z = -15$ m (35 m above source).

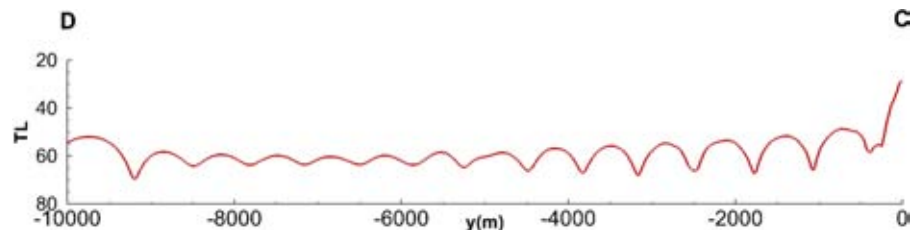
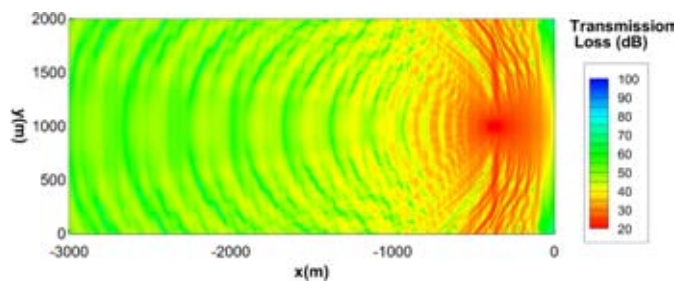


FIGURE 9

TL at $z = -5$ m based on hydrodynamic prediction of sound speed field at the end of 39-day simulation (Figure 1).



for the sound speed field corresponding to the last hour of hydrodynamic simulation in day 39 (Figure 1). Figure 10 shows the xz plane view at $y = 1,000$ m at the middle of the shoreline. Similar to the wedge shown in Figure 7, the sound penetrates into the seabed. There are multiple reflections along the shoreline, ocean surface, and seabed, which form standing wave patterns. Figure 11 shows the difference of TL between the fully developed river plume condition at the end of day 39 and the initial uniform conditions ($T = 20^\circ\text{C}$ and $S = 30 \text{ PSU}$) at $z = -5$ m. The presence of the river plume changes the sound field significantly in the far-field.

using an ASA benchmark wedge in terms of the TL as a function of the distance from the source along the upslope direction of the wedge, and the model was applied to two wedge examples.

FIGURE 10

TL for the xz plane at $y = 1,000$ m based on hydrodynamic prediction of sound speed field at the end of 39-day simulation.

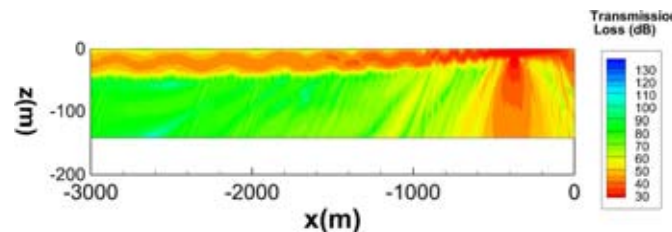
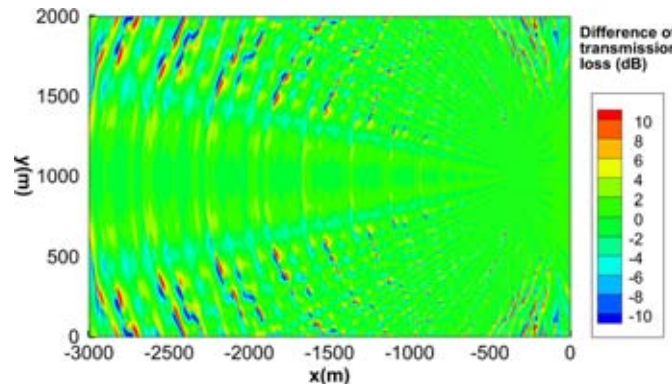


FIGURE 11

Difference of TL between using hydrodynamic predictions of sound field at the end of 39-day simulation (with the river plume) and the initial state ($T = 20^\circ\text{C}$ and $S = 30 \text{ PSU}$) without a river plume at $z = -5$ m.



This underwater sound model, forced by sound speed predictions from a hydrodynamic model, can be useful for evaluating impact on marine mammals due to construction of offshore wind (OSW) turbines and deployment and operation of marine and hydrokinetic energy devices in coastal regions. Pile driving for installation of OSW turbines may cause significant underwater noise that will disturb marine mammals including highly endangered whales. Similarly, operational sounds from tidal and ocean current turbines may disturb marine mammals and fish that are afforded special regulatory protection. The availability of a linked acoustic-hydrodynamic model that easily

Conclusion and Future Work

An underwater sound model using a finite difference method was developed to simulate sound transmission in the coastal ocean. The hydrodynamic model FVCOM was used to simulate the varying distributions of density in coastal waters and to calculate the speed of sound in the coastal environment. The CSLP method was used for fast iteration to solve the resulting large and sparse matrix system on a parallel cluster. The validation of finite difference has been presented

provides a solution for underwater acoustic outputs from these activities could allay regulatory and stakeholder concerns as well as allow rapid response for installers to mitigate noise that may be harmful or enable engineers to design turbines that produce less sound.

We are further developing the model using finite volume formulations of the Helmholtz equations with sigma coordinates that are compatible with the FVCOM model, followed by validation of the model using field observations in nearshore coastal waters in Puget Sound. In addition, in order for this model to be of practical use, the characteristics of acoustic sources and its effect on the model need to be fully investigated. For instance, the frequency range from a pile driving, which is between 100 and 1,000 Hz (Erbe, 2009; Bailey et al., 2010), can cause a large burden to the computational cost because the number of grids is proportional to the frequency cubed. Therefore, an effort needs to be made to optimize a trade-off between the fast running time and the amount of required computational resource.

Acknowledgments

This study was funded by the Pacific Northwest National Laboratory's Laboratory Directed Research and Development program under project number #66978. Drs. Taiping Wang and Genevra E. Harker from PNNL provided internal review of this manuscript. We appreciate Dr. Zhongxiang Zhao from the Applied Physics Laboratory and one anonymous scientist who served as external reviewers and helped with their insights and proofreading. We also want to express gratitude to Dr. C. Vuik's group at Delft

University of Technology for providing sample code with 2-D examples and email communications. Mr. Satish Balay from Argonne National Laboratory was very helpful with the usage of PETSc library for high-performance computing.

tion studies: Comparisons with finite difference models. *J Geophys Res.* 112:C03018. doi:10.1029/2006JC003485.

Chew, W.C., & Weedon, W.H. 1994. A 3d perfectly matched medium from modified Maxwell's equations with stretched coordinates. *Microw Opt Techn Let.* 7(13):599-604. <http://dx.doi.org/10.1002/mop.4650071304>.

Collins, M.D. 1993. A split-step Padé solution for the parabolic equation method. *J Acoust Soc Am.* 93(4):1736-42. <http://dx.doi.org/10.1121/1.406739>.

Deane, G.B., & Buckingham, M.J. 1993. An analysis of the three-dimensional sound field in a penetrable wedge with a stratified fluid or elastic basement. *J Acoust Soc Am.* 93(3):1319-28. <http://dx.doi.org/10.1121/1.405417>.

DeRuiter, S.L., Tyack, P.L., Lin, Y.T., Newhall, A.E., Lynch, J.F., & Miller, P.J. 2006. Modeling acoustic propagation of airgun array pulses recorded on tagged sperm whales (*Physeter macrocephalus*). *J Acoust Soc Am.* 120(6):4100-14. <http://dx.doi.org/10.1121/1.2359705>.

Erbe, C. 2009. Underwater noise from pile driving in Moreton Bay, Qld. *Acoust Aust.* 37(3):87-92.

Erlangga, Y.A. 2005. A robust and efficient iterative method for the numerical solution of the Helmholtz equation. Ph.D. thesis, Delft University of Technology. 126 pp.

Erlangga, Y.A., Oosterlee, C.W., & Vuik, C. 2006. A novel multigrid based preconditioner for heterogeneous Helmholtz problems. *SIAM J Sci Comput.* 27(4):1471-92. <http://dx.doi.org/10.1137/040615195>.

Hastie, G.D., Russell, D.J., McConnell, B., Moss, S., Thompson, D., & Janik, V.M. 2015. Sound exposure in harbour seals during the installation of an offshore wind farm: predictions of auditory damage. *J Appl Ecol.* 52(3):631-40. <http://dx.doi.org/10.1111/1365-2664.12403>.

Hovem, J.M., Tronstad, T.V., Karlsen, H.E., & Lokkeborg, S. 2012. Modeling propagation

Corresponding Author:

Ki Won Jung
Pacific Northwest National Laboratory
P.O. Box 999, Richland, WA 99352
Email: KiWon.Jung@pnnl.gov

References

- Bailey**, H., Senior, B., Simmons, D., Rusin, J., Picken, G., & Thompson, P.M. 2010. Assessing underwater noise levels during pile-driving at an offshore windfarm and its potential effects on marine mammals. *Mar Pollut Bull.* 60(6):888-97. <http://dx.doi.org/10.1016/j.marpolbul.2010.01.003>.
- Bailey**, H. 2012. Impacts of wind turbine construction on marine mammals: what can be done? *Int Sustain Energ Rev.* 6(1):34-7.
- Balay**, S., Abhyankar, S., Adams, M.F., Brown, J., Brune, P., Buschelman, K., ... Zhang, H. 2015. PETSc Users Manual, ANL-95/11—Revision 3.6.
- Chen**, C., Liu, H., & Beardsley, R.C. 2003. An unstructured, finite-volume, three-dimensional, primitive equation ocean model: application to coastal ocean and estuaries. *J Atmos Ocean Tech.* 20:159-86. [http://dx.doi.org/10.1175/1520-0426\(2003\)020<0159:AUGFVT>2.0.CO;2](http://dx.doi.org/10.1175/1520-0426(2003)020<0159:AUGFVT>2.0.CO;2)
- Chen**, C., Beardsley, R.C., & Cowles, G. 2006. An unstructured grid, finite-volume coastal ocean model: FVCOM user manual. School for Marine Science and Technology, University of Massachusetts Dartmouth. 315 pp.
- Chen**, C., Huang, H., Beardsley, R., Liu, H., Xu, Q., & Cowles, G. 2007. A finite volume numerical approach for coastal ocean circulation studies: Comparisons with finite difference models. *J Geophys Res.* 112:C03018. doi:10.1029/2006JC003485.
- Chew**, W.C., & Weedon, W.H. 1994. A 3d perfectly matched medium from modified Maxwell's equations with stretched coordinates. *Microw Opt Techn Let.* 7(13):599-604. <http://dx.doi.org/10.1002/mop.4650071304>.
- Collins**, M.D. 1993. A split-step Padé solution for the parabolic equation method. *J Acoust Soc Am.* 93(4):1736-42. <http://dx.doi.org/10.1121/1.406739>.
- Deane**, G.B., & Buckingham, M.J. 1993. An analysis of the three-dimensional sound field in a penetrable wedge with a stratified fluid or elastic basement. *J Acoust Soc Am.* 93(3):1319-28. <http://dx.doi.org/10.1121/1.405417>.
- DeRuiter**, S.L., Tyack, P.L., Lin, Y.T., Newhall, A.E., Lynch, J.F., & Miller, P.J. 2006. Modeling acoustic propagation of airgun array pulses recorded on tagged sperm whales (*Physeter macrocephalus*). *J Acoust Soc Am.* 120(6):4100-14. <http://dx.doi.org/10.1121/1.2359705>.
- Erbe**, C. 2009. Underwater noise from pile driving in Moreton Bay, Qld. *Acoust Aust.* 37(3):87-92.
- Erlangga**, Y.A. 2005. A robust and efficient iterative method for the numerical solution of the Helmholtz equation. Ph.D. thesis, Delft University of Technology. 126 pp.
- Erlangga**, Y.A., Oosterlee, C.W., & Vuik, C. 2006. A novel multigrid based preconditioner for heterogeneous Helmholtz problems. *SIAM J Sci Comput.* 27(4):1471-92. <http://dx.doi.org/10.1137/040615195>.
- Hastie**, G.D., Russell, D.J., McConnell, B., Moss, S., Thompson, D., & Janik, V.M. 2015. Sound exposure in harbour seals during the installation of an offshore wind farm: predictions of auditory damage. *J Appl Ecol.* 52(3):631-40. <http://dx.doi.org/10.1111/1365-2664.12403>.
- Hovem**, J.M., Tronstad, T.V., Karlsen, H.E., & Lokkeborg, S. 2012. Modeling propagation

- of seismic airgun sounds and the effects on fish behavior. *IEEE J Oceanic Eng.* 37(4): 576-88. <http://dx.doi.org/10.1109/JOE.2012.2206189>.
- Lai**, Z., Chen, C., Colwes, G.W., & Beardsley, R.C. 2010. A nonhydrostatic version of FVCOM, 1. Validation experiments. *J Geophys Res-Oceans*. 115(C11). <http://dx.doi.org/10.1029/2009JC005525>.
- Lin**, Y., Colis, J.M., & Duda, T.F. 2012. A three-dimensional parabolic equation model of sound propagation using higher-order operator splitting and Pade approximants. *J Acoust Soc Am.* 132(5):EL364-70. <http://dx.doi.org/10.1121/1.4754421>.
- Lurton**, X. 2002. An Introduction to Underwater Acoustics. London: Springer. 347 pp.
- Medwin**, H. 1975. Speed of sound in water: A simple equation for realistic parameters. *J Acoust Soc Am.* 58(6):1318-9. <http://dx.doi.org/10.1121/1.380790>.
- Miller**, P.J.O., Kvadsheim, P.H., Lam, F.P.A., Tyack, P.L., Curé, C., DeRuiter, S.L., ... Hooker, S.K. 2015. First indications that northern bottlenose whales are sensitive to behavioural disturbance from anthropogenic noise. *Roy Soc Open Sci.* 2(6):140484. <http://dx.doi.org/10.1098/rsos.140484>.
- National Research Council**. 2005. Marine Mammal Populations and Ocean Noise: Determining When Noise Causes Biologically Significant Effects, Committee on Characterizing Biologically Significant, Marine Mammal Behavior. Available at: <http://www.nap.edu/catalog/11147.html>.
- Saad**, Y., & Schultz, M.H. 1986. GMRES: A generalized minimal residual algorithm for solving nonsymmetric linear systems. *SIAM J Sci Stat Comp.* 7:856-69. <http://dx.doi.org/10.1137/0907058>.
- Talley**, L.D., Pickard, G.L., Emery, W.J., & Swift, J.H. 2011. Descriptive Physical Oceanography, Sixth Edition. Boston, MA: Elsevier. 560 pp.
- Van de Vorst**, H.A. 1992. Bi-CGSTAB: a fast and smoothly converging variant of Bi-CG for solution of non-symmetric linear systems. *SIAM J Sci Stat Comp.* 13:631-44. <http://dx.doi.org/10.1137/0913035>.
- Vuik**, C., Erlangga, Y.A., & Oosterlee, C.W. 2003. Shifted Laplace preconditioners for the Helmholtz equations. Report# 03-18, ISSN 1389-6520, Delft University of Technology.
- Yang**, Z., Wang, T., Voisin, N., & Copping, A. 2015. Estuarine response to river flow and sea-level rise under future climate change and human development. *Estuar Coast Shelf S.* 156:19-30. <http://dx.doi.org/10.1016/j.ecss.2014.08.015>.
- Young**, D.M. 1971. Iterative Solution of Large Linear Systems. New York: Academic Press. 570 pp.

Development and Application of a New Mobile pH Calibrator for Real-Time Monitoring of pH in Diffuse Flow Hydrothermal Vent Fluids

AUTHORS

Chunyang Tan
 Kang Ding
 William E Seyfried, Jr
 University of Minnesota

Introduction

It is widely recognized that the investigation of the geochemical and biochemical processes of hydrothermal vent systems relies on constraining key chemical and physical components of vent fluids (Childress et al., 1991; Von Damm, 1995). In this regard, pH is considered especially important because of the role it plays in the solubility of minerals, with direct implications for the temporal evolution of seafloor sulfide deposits. Moreover, tracing pH variation and distribution can help scientists understand the interactions between the vent organisms and their environments, which are dominated by mixing between cold oxygen bearing seawater and highly reduced hydrothermal fluid (Sarrazin et al., 1999; Von Damm & Lilley, 2004). Thus, the need is great for the development and application of *in situ* instruments that can measure and monitor pH and related components in unusually challenging environments with high resolution and accuracy in space and time (Shank et al., 1998).

In situ electrochemical measurements have been widely used in chemical

ABSTRACT

In situ measurement of pH in diffuse flow hydrothermal vent fluids is necessary to investigate the feedback between geochemical and biochemical processes. Accurate pH determination has been unusually challenging owing to temperature and pressure effects that place severe constraints on the performance of a wide variety of pH sensor systems. In this paper, we describe a newly developed mobile pH calibrator (MpHC), which makes use of *in situ* calibration protocols that enhance the accuracy of pH measurement and monitoring on the ocean floor at deep-sea hydrothermal vents. The MpHC combines the physically robust and highly sensitive iridium solid-state pH electrode with a flow control system to perform 2-point calibration with on-board pH buffer solutions. The small size and novel design of the sensor probe allow more effective access to seafloor hydrothermal vent fluids and their associated sulfide structures and biological communities. The MpHC is capable of *in situ* deployment by submersible via ICL (inductively couple link) communication around hydrothermal vents at pressures and temperatures up to 45 MPa and 100°C, respectively. In this paper, we also present results of *in situ* calibration methods used to correct the standard potential and slope (mV/pH) of the solid-state electrode for temperature effects. The MpHC has been deployed most recently using the submersible *Alvin* during cruise AT26-17 to Axial Seamount and Main Endeavour Field, Juan De Fuca Ridge in the NE Pacific. With *in situ* calibration functionality, the MpHC offers the prospect of more successful longer-term measurements in keeping with power availability provided by cabled seafloor observatories coming online in the NE Pacific.

Keywords: *in situ*, pH, calibration, hydrothermal, electrode

oceanography for decades (Reimers, 2007). With advances in electroanalytical chemistry and microelectronics technology, the pH electrode is now well suited to operate at high pressure and variable temperatures, potentially providing fundamental insight on complex geochemical and biogeochemical processes inherent to hydrothermal vent systems (Ding & Seyfried, 2007; Prien, 2007). To achieve the full potential that the new generation of electrochemical

sensors may provide, however, limitations imposed by long-term deployment in challenging and changing chemical and physical environments must be overcome; so too, the robustness of the electrodes must also be improved, if the full range of deep-sea vent applications is to be realized (Le Bris et al., 2001).

In the past few years, we developed an *in situ* pH calibration device (Deployable Calibrator), which could

perform 2-point calibration of pH *in situ* with pH buffers optimized for specific applications (Tan et al., 2010, 2012, 2014). The *in situ* calibration method minimizes potential sources of drift, enhancing accuracy of pH measurements. This instrument was used more recently to investigate the pH of diffuse flow hydrothermal vent fluid and also modified for use with cabled ocean observatories for real time pH monitoring (Tan et al., 2014). Although successful, the size of pH probe and functionality of the sensor system could be improved upon to enhance geochemical applications at deep-sea hydrothermal vents. To address these issues, a so-called mobile pH calibrator (MpHC) was developed. This highly integrated pH measurement and monitoring system was smaller than its predecessor, inherently more precise, and more tolerant of temperature variability (0–100°C). The calibrator and supporting electronics can be easily and effectively mounted on the basket of the submersible, *Alvin*, facilitating deployment at different and diverse vent sites. The calibrator was tested during a series of dives to cold seeps in connection with the *Alvin* Science Verification Cruise (AT26-12) and again during *Alvin/Atlantis* operations (AT26-17) at hydrothermal vents at Axial Seamount and the Main Endeavour Hydrothermal Field (Juan de Fuca Ridge). Here we emphasize technological modifications and operational capabilities inherent to the new electrochemical system, while also briefly reviewing results of preliminary data from the recent deployments of the calibrator at NE Pacific vent sites.

Materials and Methods

The MpHC is designed around three critical components: (1) a slim

profile (20 mm OD) terminating in the sensor probe that allows precise positioning in unusually restrictive areas, inherent to seafloor hydrothermal vent applications; (2) simultaneous pH, redox, and temperature measurement at temperatures up to 100°C; and (3) *in situ* calibration of the electrochemical sensors with no pH buffer leakage into the ambient environment. In its simplest configuration, the MpHC device consists of two parts: the sensor probe itself, for detection, and the main body, which is comprised of solenoid valves, precision pumps for fluids delivery, and supporting electronics, all contained within an oil-filled pressure housing.

The Flow Control System of MpHC

Importantly, the MpHC was specifically designed to make use of a flow control system that can deliver multiple pH buffer solutions needed to calibrate the electrodes *in situ* (Figure 1). The electrodes (Figure 2) are sealed in the flow cell at one end of the probe to facilitate interaction with the hydrothermal fluids. Subsequent to acquisition of vent fluid pH and

temperature data, *in situ* calibration is activated. This *in situ* calibration capability represents one of the most important characteristics of the sensor system. In practice, this entails flow of two different pH buffer fluids into the electrode (sensor probe) bearing flow cell. All the time, the probe is maintained at a constant position, fulfilling the promise of *in situ* calibration. Outflow of the spent buffer enters an on-board reservoir for storage, precluding contamination of the local environment. The sample fluid inlet port is sealed during the calibration interval in response to automated activation of an in-line check valve. In addition to sealing the flow cell, the check valve also acts to reduce the volume of the cell effectively precluding thermal convection of the hydrothermal fluid (Figure 1).

During *in situ* measurement of pH and temperature, the flow control system activates the micrometering pump (FMI, Inc.) to continuously draw the sample fluid through the check valve into the flow cell. The fluid passes the normally open port of valves V4 and V5 (LVM10 series valves, SMC, Inc.) and is eventually released into

FIGURE 1

Schematic illustration of process control system used for *in situ* and autonomous operations inherent to the functionality and performance of the MpHC. Arrows indicate the direction of fluid flow. Hydrothermal fluid sampling and analysis require only pump operation, while calibration requires autonomous operation of both pump and valves.

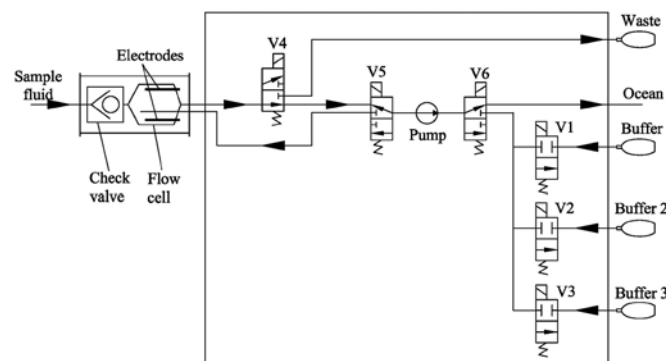
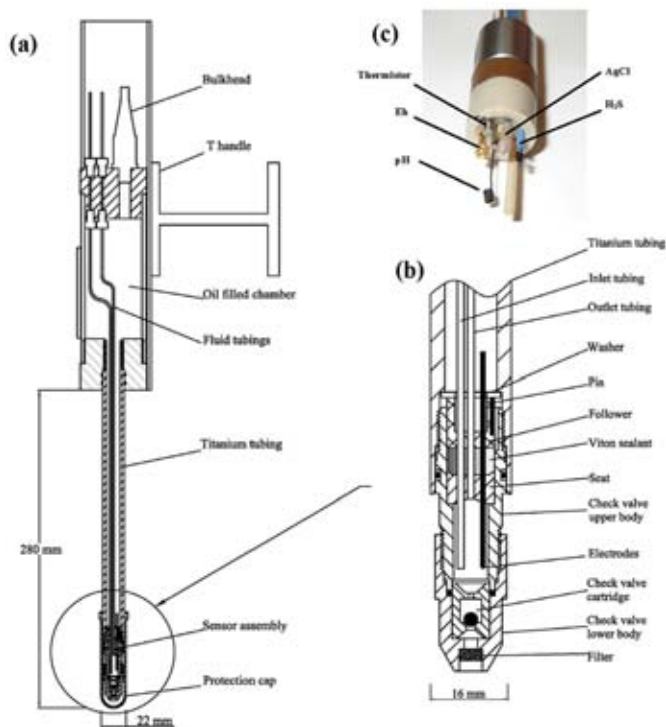


FIGURE 2

Schematic illustration of the pH probe of mobile calibrator showing integrated configuration of electrodes and check valve (a), expanded view of the flow cell assembly (b), and sensor assembly with Viton sealant and Conax fitting (c).



the surrounding seawater. In contrast, during the calibration mode of operation, the pump action is reversed, and power to the valves permits access and measurement of buffer fluids. Thus, the pH buffers are pumped into the flow cell, while the check valve is forced into the closed position by the confining pressure, as described above. This pattern of fluid flow minimizes the number of valves used and power consumption during pH measurements and calibration cycles. The flow control system of valves and pumps is contained in an oil-filled chamber. The flow rate is preset to 20 ml/min and is adjustable up to 60 ml/min depending on the specific application. All wetted parts are constructed by highly corrosive resist material, such as Teflon (PTFE) and PEEK.

The Sensor Probe

The electrochemical sensors inherent to the design and functionality of the MpHC device include solid-state electrodes for measurement of pH ($\text{Ir}-\text{IrO}_x$), redox (platinum), dissolved sulfide ($\text{Ag}-\text{Ag}_2\text{S}$), and reference electrode ($\text{Ag}-|\text{AgCl}$) (Figure 2c). The small size (~1 mm OD) and solid-state design of the pH cell enhance durability and deployment in and around rigid sulfide and rock structures. The electrochemical array also includes a titanium-sheathed thermistor with $\pm 0.1^\circ\text{C}$ resolution. Owing to the chemical and thermal heterogeneity of diffuse flow vent fluids and the importance of pH on microbial and mineralization processes, the *in situ* measurement and calibration protocols we demonstrate represent an initial, but essential step, if long-term

measurement and accurate interpretation of biogeochemical processes associated with these systems is to become a reality.

The sensor probe for pH measurement is constructed of three essential components: (1) oil-filled chamber for hydrostatic pressure compensation, (2) titanium housing for structural support, and, (3) flow cell assembly, which automates sampling and calibration procedures (Figure 2a). The oil-filled chamber contains dielectric silicone oil and is equipped with a T handle to facilitate deployment by submersible manipulator action. The flow cell assembly is situated at the end of the titanium housing and connects to the oil filled electronics chamber, as summarized above (Figure 2b). A modified Conax (Conax Technologies, Inc.) fitting with PEEK and Viton sealants holds the electrodes and two PEEK fluid circulation tubes (OD 1.58 mm) in place. Applying torque on the Viton sealant forms a watertight seal between the flow cell and the silicone oil-fluid titanium tubing. The small internal volume (~1 ml) of the flow cell minimizes dead volume and enhances signal response to samples and standards. A PEEK check valve cartridge (Optimize Technologies) with ruby ball and sapphire seat was selected to meet the stringent fluid flow requirements discussed above. The fluid circulation tubing allows for distribution of fluid samples and pH buffer fluids in and out of the electrochemical sensor cell. A PTFE mesh is used at the sample inlet to remove large particle entrained in the fluid samples.

The upper and lower portions of the check valve assembly unit are constructed entirely of PEEK. The distance between the sensing portion of the pH electrode and the sample inlet port is 20 mm. The OD of the flow cell

assembly is ~16 mm, and the total length of the titanium tubing including the flow cell assembly is 280 mm (Figure 2a). As noted, the tolerance to relatively high fluid temperatures together with narrow width of the probe facilitates deployment in environments in and around diffuse flow hydrothermal vent sites.

Lab experiments demonstrated that approximately 5 min is required to complete one calibration cycle. Thus, the MpHC can complete more than 16 calibration cycles with the current design constraints and on-board storage capacity of the waste buffer solutions.

General Description of the MpHC

The MpHC, including the flow control system, battery compartment, electronics housing, and buffer fluid reservoirs, is placed in a plastic container that occupies approximately 0.5 m² of “basket” space on the *Alvin* submersible (Figure 3). The sensor probe (external to the control system container box) is stored in a vertical PVC tube designed to facilitate its

removal and return. The control system and probe, however, were linked by communication cable (3 m). The MpHC weighs approximately 27 kg in air and 16 kg in water.

Sensor signals are processed at a rate of one measurement every 5 s and stored on a 14-bit data logger. The flow system is linked to a control circuit, which, like the data logger, is of low power design and consists of ICL (inductively couple link) communication (Fornari et al, 1997) and on-board flash memory.

Before deployment, the flow cell is filled with artificial saltwater to maintain hydrostatic pressure balance at the seafloor. In practice, *in situ* pH measurement is coordinated between the *Alvin* pilot and the scientist operating the MpHC via ICL communication. A control GUI was developed using LabVIEW software and loaded on a Samsung XE700T tablet to facilitate operation. When the manipulator positions the sensor probe at a target location, the operator turns on the flow control system to draw in hydro-

thermal fluid, while the sensor signal is displayed on a computer screen. Subsequently, the operator will activate the calibration subroutine, while the manipulator maintains the sensor probe in a stationary position. The GUI stores the MpHC status and electrode readings on the hard drive of the tablet. Accordingly, all the data are copied to onboard memory for subsequent processing.

In situ pH Calculation

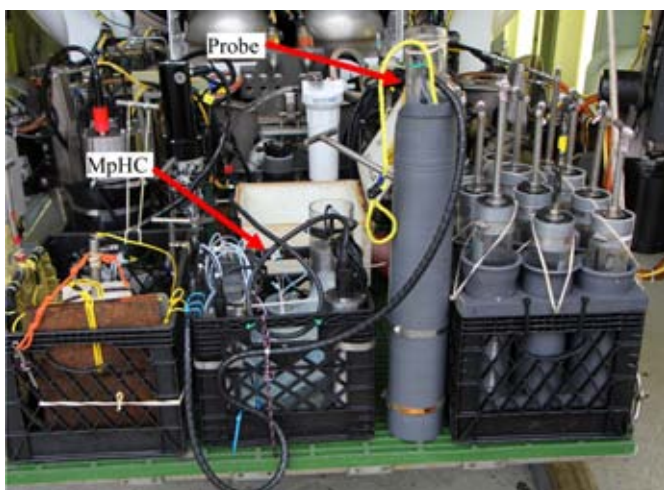
Temperature and pressure play an important role in sample and buffer pH and electrochemical characteristics of the electrodes. Theoretically, sample acquisition and calibration should be performed at the same temperature; however, this is not always possible because of abrupt temperature changes caused by mixing between hydrothermal fluids and seawater. Accordingly, sharp temperature gradients are common during a measurement or calibration cycle, for which laboratory correction needs to be applied.

Laboratory Calibration

To correct pH buffer solutions for temperature variability experienced on the seafloor at deep-sea vents, three pH buffer solutions were subjected to a series of laboratory experiments. These pH buffers are commercially available from Fisher Scientific, with product identification numbers B79, B82, and B77, respectively. As with our seafloor buffers, the dissolved chloride concentration of each of these buffers was adjusted to minimize liquid junction effects when used in seawater-type fluids. This, of course, requires reassessment of the buffer pH value, especially when exposed to temperature variability. The temperature calibration test of each buffer was performed

FIGURE 3

MpHC mounted on basket of DSRV *Alvin* prior to dives to the Ashes vent area, Axial Seamount, NE Pacific Ocean in July 2014. The entire system occupies approximately 0.2 m² of basket space and weighs approximately 16 kg in water. The probe is stowed in a PVC chamber on basket.



using a Ross pH combination electrode (Thermo Scientific), which was connected to an ATC probe (Orion) for temperature compensation. In practice, the tests were performed in a water bath where temperatures could be adjusted from 2°C to 50°C. The pH buffers were determined to have pH values of 3.74, 7.05, and 10.39 at 25°C and 1 atm. Although tests such as these allow buffer fluid pH response to be calibrated at temperatures broadly analogous to the range of vent fluid temperatures that may be encountered on the seafloor, uncertainties associated with the corresponding response of the Ir-IrO_x solid-state pH electrode also need to be determined. Thus, we performed a separate series of measurements using the same Ir-based solid-state pH sensor actually used for our vent studies. The electrochemical response of this pH sensor was previously established at elevated temperatures (Pan & Seyfried, 2008), but until now this has not been verified at temperatures less than 25°C, in terms of both Nernstian response and response time. Accordingly, the Ir-IrO_x|Ag-AgCl electrodes, combined with Orion ATC probe, were sealed in a glass reaction cell into which the previously calibrated pH buffer fluids were incrementally added. In this case, however, only pH buffers 3.74 and 7.05 (25°C) were utilized, since these buffers are less sensitive to changing temperature, allowing us to more closely and effectively examine the effect of temperature and pH on the electrochemical response inherent to the Ir-IrO_x sensor. Temperature and electrode potential were simultaneously measured and recorded at 1°C increments from 2°C to 50°C using a modified Thermo A211 pH meter. With benefit of the previously established values of

the pH buffers with temperature, the slope of the electrodes could be unambiguously determined (Figure 4). The measured slope, S_{measured} , is in excellent agreement with the theoretical Nernstian slope, $S_{\text{theoretical}}$, over the full temperature range. The potential of the electrode with buffer 3.74 was also shown to vary linearly with temperature with a coefficient of -0.8625 mV/°C.

Thus, laboratory calibration helped to establish the effect of temperature variability on pH measurement and calibration. In effect, with two *in situ* calibration cycles, the Nernst slope can be determined, providing accurate pH data for diffuse flow hydrothermal vent fluids. It is important to emphasize, however, that this approach assumes that the effect of temperature on the buffer solutions used for the *in situ* calibration is known, either from lab tests, as performed here, or based on theoretical calculations that explicitly consider the effect of

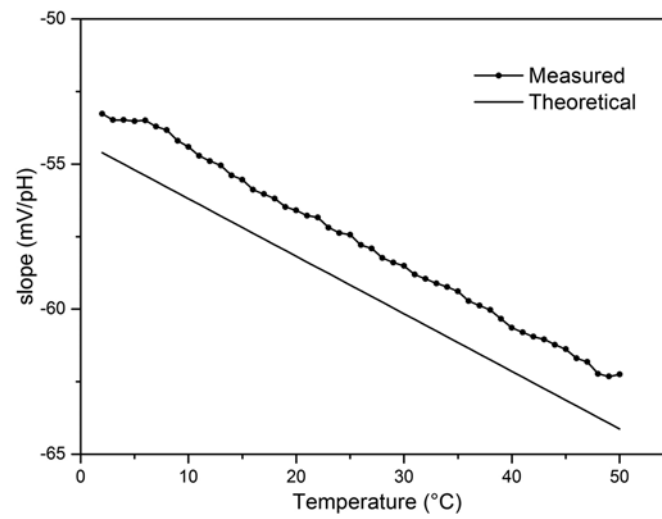
temperature on the distribution of aqueous species.

***In situ* pH Calculation Method**

In situ calculation of pH at seafloor vents using the MpHC instrument is accomplished by a three-step procedure. First, at an initial temperature (T_1), the potential of the pH and reference electrodes are determined in response to reaction with two buffer fluids (A and B). This procedure allows determination of the Nernst slope (S_{T_1}). It is important to emphasize that the choice of buffer A is based on our previously determined tests showing that the pH value of the solution is largely unaffected by temperature. Thus, buffer A with the pH value pH_A can more effectively provide a reference or anchor potential against which temperature effects can be compared. Subsequently, the procedure is repeated for the same two buffers at a different temperature (T_2), which then allows determination of the slope

FIGURE 4

Measured mV/pH response of Ir-IrO_x (pH) and Ag-AgCl (reference) electrodes with temperature. The measured data show a linear correlation with temperature equivalent to $0.198 \text{ mV} \cdot \text{pH}^{-1} \cdot ^\circ\text{C}^{-1}$. This is in excellent agreement with that predicted from the theoretical Nernstian slope over the temperature range tested. The y-intercept is a unique function of the standard potential (E°) of the electrode.



(S_{T_2}). Finally, actual pH measurements of the hydrothermal fluid are carried out at some other temperature (T_x), with the slope (S_{Tx}) and reference potential obtained from buffer A (E_{ATx}), as defined from the following set of linear equations:

$$S_{Tx} = S_{T1} + (T_x - T_1) \frac{S_{T2} - S_{T1}}{T_2 - T_1} \quad (1)$$

$$E_{ATx} = E_{AT1} + (T_x - T_1) \frac{E_{AT2} - E_{AT1}}{T_2 - T_1} \quad (2)$$

With equations (1) and (2), the *in situ* pH of a sample (pH_{STx}) can be determined from the measured potential E_{STx} as follows:

$$pH_{STx} = pH_A + \frac{E_{STx} - E_{ATx}}{S_{Tx}} \quad (3)$$

In effect, by performing two *in situ* calibration cycles at any temperature, the temperature dependence of the standard potential of the Ir-IrO_x sensor is accounted for and corrected. Using this procedure, the accuracy of the *in situ* pH derived from the raw potential is significantly improved. The hydrothermal diffuse flow environment at deep-sea vents is characterized by relatively large temporal temperature and pH variability and is well suited to test the procedures proposed for pH calibration and measurement. The first calibration cycle is typically conducted in ambient seawater at depth as the vent system is approached, whereas the second calibration is conducted at the point of the target hydrothermal fluids, and immediately followed by the hydrothermal measurement. Thus, two calibrations at different temperatures are obtained in keeping with the calibration scheme

outlined above. In some cases, only one calibration can be performed due to the schedule of a certain dive. In such cases, the coefficients of the slope and buffer potential obtained in the lab are used to calculate the *in situ* pH value, but this is not optimal, since the effect of pressure is not being accounted for, rendering small, but uncertain error (Le Bris et al., 2001).

Field Deployment and Initial Result

Field Test

The MpHC has undergone a number of field trials that have provided confirmatory evidence of the effectiveness of the *in situ* auto calibration procedures as a means of monitoring pH in variably high temperature subseafloor hydrothermal environments. For example, during cruise AT26-17 (July 2014), the MpHC was used to measure the pH of diffuse hydrothermal fluids at Axial Seamount, in the NE Pacific (45°55'N, 130°0.0'W) and also at similar low-temperature vents within Main Endeavour Field, Juan De Fuca Ridge (47°57.0'N, 129°6.6'W). These vent systems have been long-studied, since both are target locations for the U.S. Ocean Observatory Initiative and the Neptune cabled observatory (Oceans Network Canada), respectively (Kelly et al., 2012, 2014). The MpHC completed three deployments facilitated by assets intrinsic to DSRV *Alvin*. Importantly, during dive 4743 (Sully diffuse flow vent site, MEF), the MpHC was used for pH and redox measurements in vent fluids at temperatures as high as 70°C. The water depth at this site is 2,189 m.

Longer-term deployment opportunities were available at the Axial Seamount. In particular, vent fluids were

sampled at the base of the Phoenix sulfide structure within the ASHES field (45°55.99'N, 130°0.82'W) at a depth of 1,544 m. The temperature of the diffuse flow fluid ranged from 3°C to 25°C, whereas the nearby high-temperature (black smoker) vent fluid issuing from the central portion of the same structure was 312°C. The temperature distribution underscores that the mixing with cold ambient seawater contributes to diffuse flow hydrothermal processes, while still providing components sufficient to fuel microbial communities and associated macrofaunal assemblages (Figure 5), which are intimately related to the low temperature vent fluid.

For this dive, buffer fluids with pH values (25°C) of 3.74 and 10.39 were utilized to calibrate the chemical sensor system on the seafloor. Accordingly and in keeping with previously defined procedures, the MpHC calibration cycle was first performed at the ambient seawater temperature 2.6°C.

FIGURE 5

MpHC in operation in and around a tubeworm colony at Phoenix hydrothermal site at Ashes vent field (Axial Seamount) during *Alvin* dive 4741, July 21, 2014 at a depth of 1,544 m. The temperature of the diffuse flow fluid ranged from approximately 5°C to 25°C. Note the close proximity of a tube worm colony and the diffuse flow to high-temperature vents where fluid temperatures exceed 300°C.



Upon initial deployment at the vent site, the MpHC unit performed a 10-min measurement of the temperature and pH of the hydrothermal fluid and then conducted a 2-point calibration for the next 20 min. During the entire process, the *Alvin* manipulator maintained the sensor probe at the same location (Figure 6). At the onset of the calibration cycle potential (mV) readings changed rapidly and consistently owing to constraints imposed by temperature variability and the values of pH buffer fluids relative to ambient seawater and the conditions of the diffuse flow hydrothermal environment. Indeed, data indicate that the temperature increased from approximately 2.6 to $\sim 23^{\circ}\text{C}$ within the diffuse flow fluid and then decreased.

The potential/pH relationship of the two calibration cycles and corresponding hydrothermal fluid measurement cycles are shown in Figure 7 (data of the calibration cycles are

FIGURE 7

Potential/pH relationships over two calibration cycles at the Axial Seamount study area. These data provide temperature-dependent mV/pH response to correct for temperature variability during calibration and measurement at 2.6°C and 12°C . Based on the two calibration cycles (Table A1), the *in situ* pH at any other temperature within the range of the calibration scheme (e.g., T_x) can be determined. Predicted mV/pH for $T_x=23^{\circ}\text{C}$ is shown for comparison (see text). Buffer 3.74 (25°C) was used to obtain the standard potential E_{ATx} due to its pH value (pH_A) shows relative thermal stability. The variability of the slopes of the temperature dependent E/pH trends is largely a property of the effect of temperature on the standard potential of the Ir-IrO_xpH sensor, underscoring the need for *in situ* calibration.

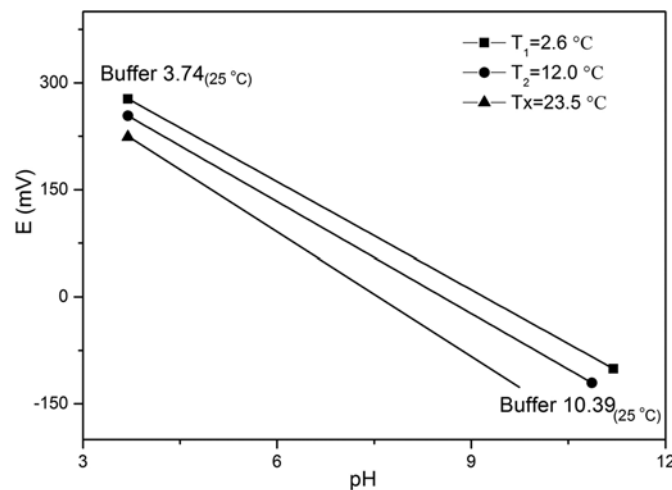
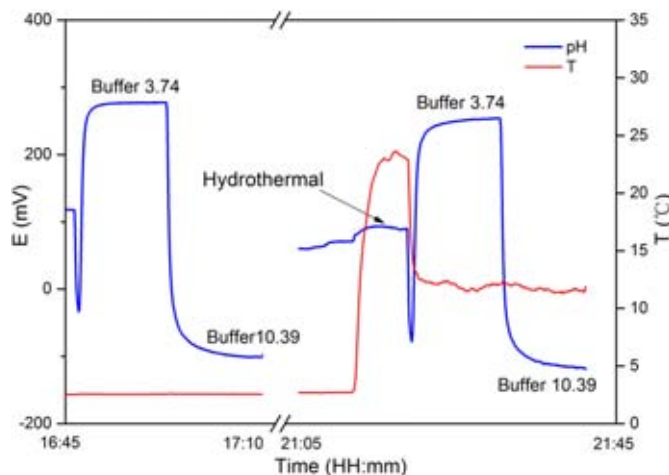


FIGURE 6

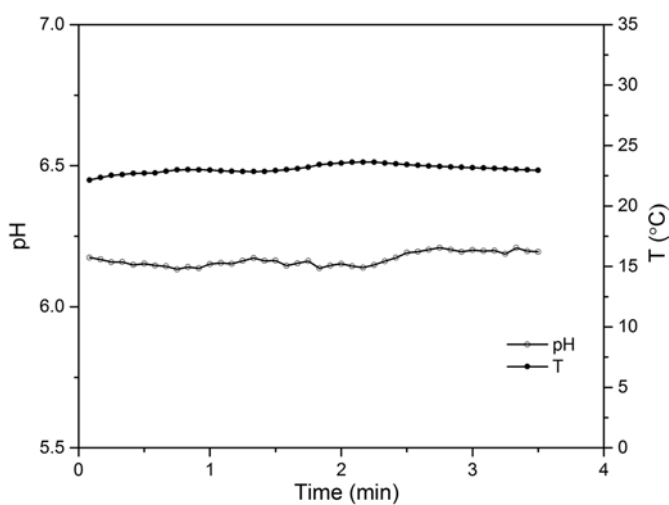
In situ potential of Ir-IrO_xpH electrode with coregistered temperature data from MpHC deployment during *Alvin* dive 4741, 1,544 m (see text) to Phoenix hydrothermal site in ASHES vent field (Axial Seamount). Initial pH calibration was performed in seawater at 2.6°C immediately before repositioning the sensor system in the diffuse flow fluid where fluid temperature increased sharply to $\sim 23.5^{\circ}\text{C}$, while temperature and electrochemical data were continuously recorded. The change in temperate of the vent fluid to approximately 12°C elicited a second calibration cycle. The two buffer calibration cycles, *in situ*, at two different temperatures allowed.



shown in Table A1). As emphasized earlier, the potential response of the 3.74-pH buffer was used to calculate the E_{ATx} in Equation 2. Figure 7 also reveals the steepening of the mV/pH slope with increasing temperature at seafloor pressure. This is caused by the effect of temperature and pressure on the thermodynamic properties of the Ir-IrO_x sensor, which influence the sensors standard potential (E°). Thus, using equations (1)–(3), a pH value of 6.14 is obtained for the hydrothermal fluid at 23°C (Figure 8). The accuracy of this number is difficult to constrain unambiguously owing to the inherent temperature, pressure, and compositional variability that characterizes diffuse flow hydrothermal fluids and the limited bottom time available, precluding repeat measurements at similar conditions. However, we did conduct multiple

FIGURE 8

pH and temperature data obtained for diffuse flow vent fluid at Axial Seamount, NE Pacific Ocean. The ~4-min record reveals steady state temperature and pH of 23°C and 6.14, respectively. The accuracy of the pH data benefits from temperature and pressure calibration procedures outlined in the text and summarized in Figures 6 and 7.



measurements of seawater at a depth of 1,450 m at Axial Seamount with a similar instrument with the same electrochemical and buffer control systems (Tan et al., 2012). These data indicate seawater pH of 7.65 ± 0.1 . The extent to which this test applies to the uncertainty attending the diffuse fluid pH measurements reported above is largely dependent on the effectiveness of the temperature dependent correction procedures developed and applied during the present investigation.

Comparing Data With Other Sites of Diffuse Flow Hydrothermal Activity

It has long been recognized based on mass balance and limited geochemical modeling results that diffuse flow fluids are best explained as nearly conservative mixes of high temperature vent fluids with seawater, with some additional conductive heating of the seawater vent mix (Von Damm & Lilley, 2004; Luther et al., 2012; Pester et al., 2008; Butterfield et al., 2004). Data

from these and other studies confirm this for diffuse flow fluids at the Axial Seamount study area (Edmond et al., 1979) and at EPR 9°N (Von Damm et al., 2004), where the extent of seawater mixing is, as usual, best indicated by the near seawater concentrations of dissolved Mg. In spite of this, however, there still exist noteworthy concentrations of transition metals and dissolved gases needed to fuel microbial metabolism, while the relatively high dissolved silica provides evidence of the magnitude of high-temperature source fluids that is added to the mix (Von Damm et al., 2004; Butterfield et al., 2004; Le Bris et al., 2003). Almost always, pH values are less than typical of seawater, as reported during the present study, although in a more general sense, pH decrease often correlates positively with temperature and dissolved sulfide (Luther et al., 2012). *In situ* pH values reported here (6.14 at 23°C) are generally within the range of analogous values reported for vent sites at EPR 9°N for fluids with

similar dissolved sulfide concentrations, although substantial variability in pH (*in situ*) is the norm not the exception (Luther et al., 2012). Part of the variability likely relates to constraints imposed by the composition of the high-temperature hydrothermal component, while other factors including biological activity and uncertain chemical reaction processes in the mixing zone, also likely play a role. Brief, but repeated spikes in temperature and fluid chemistry, including pH, are a well-recognized if not a characteristic feature of diffuse flow venting, further complicating cause and effect phenomena. Only by extending the time series and deploying *in situ* samplers with internal calibrating capabilities at different vent sites for much longer times can we expect to understand unambiguously the interplay among chemical, physical, and biological processes at deep-sea vents. Efforts reported here represent an important first step in realizing this goal.

Conclusions

The MpHC system was developed to perform reliable and precise pH measurements in and around hydrothermal diffuse flow vents on the seafloor at midocean ridges. A critical element of the new device involves the capability for autonomous calibration *in situ* on the seafloor. Accordingly, multiple on-board buffers are sequentially delivered to a small volume flow cell in which solid-state pH, reference, and redox electrodes, as well as temperature sensors, are contained. Computer-controlled valves and pumps activated in response to temperature or time facilitate the *in situ* calibration procedures, including rinse cycles with ambient seawater. The small size and low dead volume

of the electrode-bearing flow cell enhance signal response time, while minimizing consumption of buffer fluid.

The *in situ* calibration capability of the MpHC is essential to address the effect of temperature and pressure on electrochemical performance, especially in the diffuse flow vent systems, where the mixture between high-temperature vent fluid and seawater often produces temperature variability in time and space. Lab measurements have confirmed that temperature variability influences not only the pH buffer speciation but more importantly the standard potential (E°) of the solid-state IrO_x sensor. *In situ* calibration on the seafloor at two different temperatures with two different pH buffers has been found to be sufficient to correct for temperature effects permitting accurate pH measurement of vent fluids at temperatures different from the temperature of calibration cycle, broadening the efficiency and effectiveness of collecting vent fluid pH data.

The MpHC has been deployed by the submersible *Alvin* to measure and monitor pH at sites in the Gulf of Mexico and also at diffuse flow vents associated with hydrothermal activity at the Ashes vent field, Axial Caldera, northeast Pacific Ocean. In both cases, data indicate that the auto calibration procedures provide an effective means to assure the accuracy of the pH data and offer promise for longer-term monitoring of pH and other components with power available from cabled observatories.

Acknowledgments

We would like to thank the *Alvin* operations team, the captain and crew of R/V *Atlantis*, and the Deep Submergence Science Committee (DeSSC)

for their help during the deployment of MpHC. This work is funded by U.S. NSF grant 0927615, China CAS grant XDB06040300, and China NSF grant 41406110.

Corresponding Author:

Chunyang Tan
Department of Earth Sciences,
University of Minnesota
310 Pillsbury DR SE,
Minneapolis, MN 55455
Email: tanc@umn.edu

References

- Butterfield**, D.A., Roe, K.K., Lilley, M.D., Huber, J.A., Baross, J.A., Embley, R.W., & Massoth, G.J. 2004. Mixing, reaction and microbial activity in the sub-seafloor revealed by temporal and spatial variation in diffuse flow vents at Axial Volcano. In: Subseafloor Biosphere at Mid-Ocean Ranges, eds. Wilcock, W.S.D., DeLong, E.F., Kelley, D.S., Baross, J.A., & Cary, S.C., pp. 269-89. Washington, DC: American Geophysical Union.
- Childress**, J.J., Fisher, C.R., Favuzzi, J.A., Kochevar, R.E., Sanders, N.K., & Alayse, A.M. 1991. Sulfide driven autotrophic balance in the bacterial symbiont containing hydrothermal vent tubeworm, *Riftia pachyptila* Jones. Biol Bull. 180(1):135-53. <http://dx.doi.org/10.2307/1542437>.
- Ding**, K., & Seyfried, W.E., Jr. 2007. *In situ* measurement of pH and dissolved H₂ in mid-ocean ridge hydrothermal fluids at elevated temperatures and pressures. Chem Rev. 107(2):601-22. <http://dx.doi.org/10.1021/cr050367s>.
- Edmond**, J.M., Measures, C., McDuff, R.E., Chan, L.H., Collier, R., Grant, B., ... Corliss, J.B. 1979. Ridge crest hydrothermal activity and the balances of the major and minor elements in the ocean: the Galapagos data. Earth Planet Sci Lett. 46(1):1-18. [http://dx.doi.org/10.1016/0012-821X\(79\)90061-X](http://dx.doi.org/10.1016/0012-821X(79)90061-X).
- Fornari**, D., Bradley, A., Humphris, S., Walden, B., Duester, B., Catanach, R., ... Hickey, J. 1997. Inductively coupled link (ICL) temperature probes for hot hydrothermal fluid sampling from ROV Jason and DSV *Alvin*. Ridge Events. 8(1):26-31.
- Kelley**, D.S., Carbotte, S.M., Caress, D.W., Clague, D.A., Delaney, J.R., Gill, J.B., ... Wilcock, W.S.D. 2012. Endeavour Segment of the Juan de Fuca Ridge: One of the most remarkable places on Earth. Oceanography. 25(1):44-61. <http://dx.doi.org/10.5670/oceanog.2012.03>.
- Kelley**, D.S., Delaney, J.R., & Kim Juniper, S. 2014. Establishing a new era of submarine volcanic observatories: Cabling Axial Seamount and the Endeavour Segment of the Juan de Fuca Ridge. Mar Geol. 352(1):426-50. <http://dx.doi.org/10.1016/j.margeo.2014.03.010>.
- Le Bris**, N., Sarradin, P.M., & Pennec, S. 2001. A new deep-sea probe for *in situ* pH measurement in the environment of hydrothermal vent biological communities. Deep-Sea Res Pt I. 48(8):1941-51. [http://dx.doi.org/10.1016/S0967-0637\(00\)00112-6](http://dx.doi.org/10.1016/S0967-0637(00)00112-6).
- Le Bris**, N., Sarradin, P., & Caprais, J. 2003. Contrasted sulphide chemistries in the environment of 13°N EPR vent fauna. Deep-Sea Res Pt I. 50(6):737-47. [http://dx.doi.org/10.1016/S0967-0637\(03\)00051-7](http://dx.doi.org/10.1016/S0967-0637(03)00051-7).
- Luther**, G.W., III, Gartman, A., Yücel, M., Madison, A.S., Moore, T.S., Nees, H.A., ... Fisher, C.R. 2012. Chemistry, temperature, and faunal distributions at diffuse-flow hydrothermal vents: Comparison of two geologically distinct ridge systems. Oceanography. 25(1):234-45. <http://dx.doi.org/10.5670/oceanog.2012.22>.
- Pan**, Y., & Seyfried, W.E., Jr. 2008. Experimental and theoretical constraints on pH measurements with an iridium oxide electrode in aqueous fluids from 25 to 175°C and 25 MPa. J Solution Chem. 37(8):1051-62. <http://dx.doi.org/10.1007/s10953-008-9293-z>.
- Pester**, N.J., Butterfield, D.A., Foustaoukos, D.I., Roe, K., Ding, K., Shank, T.M., & Seyfried, W.E., Jr. 2008. The chemistry of diffuse-flow vent fluids on the Galapagos Rift (86°W): Temporal variability and subseafloor phase equilibria controls. In: Magma to

- Microbe: Modeling Hydrothermal Processes at Oceanic Spreading Centers, eds. Lowell, R.P., Seewald, J., Metaxas, A., & Perfit, M.R., pp. 123-44. Washington, DC: American Geophysical Union.
- Prien**, R.D. 2007. The future of chemical *in situ* sensors. Mar Chem. 107(3):422-32. <http://dx.doi.org/doi:10.1016/j.marchem.2007.01.014>.
- Reimers**, C.E. 2007. Applications of micro-electrodes to problems in chemical oceanography. Chem Rev. 107(2):590-600. <http://dx.doi.org/10.1021/cr050363n>.
- Sarrazin**, J., Juniper, S.K., Massoth, G., & Legendre, P. 1999. Physical and chemical factors influencing species distributions on hydrothermal sulfide edifices of the Juan de Fuca Ridge. Northeast Pacific. Mar Ecol-Prog Ser. 190:89-112. <http://dx.doi.org/10.3354/meps190089>.
- Shank**, T.M., Fornari, D.J., Von Damm, K.L., Lilley, M.D., Haymon, R.M., & Lutz, R.A. 1998. Temporal and spatial patterns of biological community development at nascent deep-sea hydrothermal vents (9°50'N, East Pacific Rise). Deep-Sea Res Pt II. 45:465-515. [http://dx.doi.org/10.1016/S0967-0645\(97\)00089-1](http://dx.doi.org/10.1016/S0967-0645(97)00089-1).
- Tan**, C., Jin, Bo, Ding, K., Seyfried, W.E., Jr., & Chen, Y. 2010. A long-term *in situ* calibration system for chemistry analysis of seawater. J Zhejiang Univ-Sc A. 11(9):701-8. <http://dx.doi.org/10.1631/jzus.A0900643>
- Tan**, C., Ding, K., Jin, B., Seyfried, W.E., Jr., & Chen, Y. 2012. Development of an *in situ* pH calibrator in deep sea environments. IEEE-ASME T Mech. 17(1):8-15. <http://dx.doi.org/10.1109/TMECH.2011.2168419>.
- Tan**, C., Ding, K., & Seyfried, W.E., Jr. 2014. *In situ* pH measurement and real-time calibration: applications to ocean observatories at deep sea vents. Sea Technol. 55(6): 41-4.
- Von Damm**, K.L. 1995. Controls on the chemistry and temporal variability of seafloor hydrothermal fluids. In: Seafloor hydrothermal Systems: Physical, Chemical, Biological and Geological Interactions, eds. Humphris, S.E., Zierenberg, R.A., Mullineaux, L.S., & Thomson, R.E., pp. 222-47. Washington, DC: American Geophysical Union. <http://dx.doi.org/10.1029/gm091p0222>.
- Von Damm**, K.L., & Lilley, M.D. 2004. Diffuse flow hydrothermal fluids from 9°50'N East Pacific Rise: origin, evolution and biogeochemical controls. In: The Subseafloor Biosphere at Mid-Oceanic Ridges, eds. Wilcock, W.S.D., Cary, S.C., Delong, E.F., Kelly, D.S., & Baross, J.A., pp. 245-68. Washington, DC: American Geophysical Union.

Appendix A Supporting Information

TABLE A1

Simultaneous pH and temperature data recorded during two calibration cycles performed *in situ* in diffuse fluid issuing from the base of the Phoenix chimney structure, Ashes vent field, Axial Seamount, NE Pacific Ocean in July 2014. The *in situ* potential reading of each pH buffer was derived from the averaged recording for the last full minute of operation during each calibration cycle. Lab tests were used to correct the data for the effect of temperature, while much smaller pressure effects were corrected from available theoretical and empirical data. Thus, the influence of temperature and pressure on the slope was shown to be linear and result in a combined increase of $0.187 \text{ mV}\cdot\text{pH}^{-1}\cdot\text{^\circ C}^{-1}$. Although the pH 3.7 buffer solution was shown to be only slightly affected by temperature, the same was not the case for the pH 10.4 buffer. In any event, the measured slopes (E/pH) at 2.6 and 12°C were still within 90% of the theoretical value at each temperature.

Sample	pH _{in situ}	E (mV)	T (°C)	Measured slope (mV/pH)	Theoretical slope (mV/pH)
Buffer A	3.70	277 ± 0.3	2.6	-50.4	-54.7
Buffer B	11.20	-100.6 ± 0.4			
Buffer A	3.70	253.6 ± 0.5	12.0	-52.2	-56.6
Buffer B	10.87	-120.5 ± 2.0			

Micro-Modem for Short-Range Underwater Mobile Communication Systems

AUTHORS

Jun-Ho Jeon

Sung-Joon Park

Department of Electronic

Engineering, Gangneung-Wonju

National University

ABSTRACT

Recently, there has been great interest in short-range underwater communication for applications such as water pollution monitoring, fish farming, oceanographic data collection, and underwater tactical surveillance based on underwater sensor network systems. Because underwater wireless communication relies primarily on acoustics, the development of acoustic modems has been an important topic that needs to be addressed. Furthermore, for years, underwater biomimetic fish robots have been studied in the area of biomechanics for scientific use and reconnaissance missions. In this article, we describe an underwater mobile communication system where fish robots act as sensor nodes, which is different from the conventional concept of an underwater sensor network that is static. We describe the issues that need to be resolved to provide mobility to a node, and we develop a micro-modem to meet the requirements of a moving node. Experiments conducted with prototypes in both a lake and a river verify that the proposed system provides a new degree of freedom (mobility) and is a viable approach.

Keywords: underwater communication, underwater mobile sensor network, underwater robot, micro-modem

Introduction

For a considerable period of time, underwater communication systems have focused mainly on applications such as marine resource exploration, deep-sea probes, and large-sized underwater vehicles. As an enabling technology, research on long-distance underwater acoustic modems has been conducted by both academia and industry. Although acoustic waves are inherently resilient to attenuation in a water medium, a modem must emit a high signal power to achieve the designated working range.

Quite recently, the field of underwater wireless sensor networks (UWSNs) has emerged as a rapidly growing area of research as a result of its wide range of aquatic applications both in inland waters and in the littoral seas (e.g., water pollution monitoring, fish farming, oceanographic data collection, and underwater tactical surveillance) (Akyildiz et al., 2005). The increasing demand for short-range wireless connections between nodes has introduced a new challenge to the development of micro-modems, which have the properties of small size, low power consumption, and moderate data rate and coverage. The initial work on small-scale acoustic

modems, named CORAL (Pandya et al., 2005), spurred the research and development of micro-modems (Freitag et al., 2005; Lee et al., 2014), including the well-known micro-modem developed by the Woods Hole Oceanographic Institution.

The field of biomimetic fish robots, which are a type of underwater vehicle, is another interesting research area that attempts to make the best use of the laws of nature. Since a fish robot utilizing biomechanics was first introduced (Streitlien et al., 1996), many bio-inspired underwater robots have been investigated. The recently unveiled GhostSwimmer, developed by the U.S. Navy, is the newest water drone mimicking a tuna, which operates autonomously or with a tether in water depths ranging from 0.25 to 91 m. When operating independently, the fish robot must be periodically brought

to the surface to deliver the data it has gathered.

In this article, we propose the use of an underwater fish robot equipped with an acoustic communication module for efficient underwater mobile communication systems. If wireless communication support is added to a fish robot, it is possible to control the robot and to transfer the collected data in real time without the help of an umbilical cable or the use of periodic floatation, which are troublesome and time-consuming. Furthermore, unlike a static UWSN, the fish robot provides insight into a new research area, underwater mobile sensor networks using robotic fish as underwater sensor nodes. For this purpose, we first identify the immediate issues that need to be addressed in order to develop a micro-modem for underwater mobile devices. In particular, we

focus on the characteristics of a spherical transducer acting as a common endpoint of the transmitter and the receiver, the underwater channel based on a ray tracing model, and the requirements for the modem. Furthermore, we investigate a frame format and a symbol structure that are adequate for the data transfer requirements of the target system, and we develop a prototype of a micro-modem. In order to verify the functionality of the modem and the feasibility of the aggregated system prototype, experiments are conducted in a lake and river.

The remainder of this article is organized as follows: First, we briefly introduce the objectives and the operational scenarios of short-range underwater mobile communication systems. Next, we explain in detail the research challenges regarding the realization of micro-modems for use in underwater mobile communication systems and describe a design and implementation of a micro-modem conforming to requirements. Lastly, we present experimental results and give concluding remarks that include direction for further research.

Underwater Mobile Communication Systems Underwater Robot System

A prevalent assumption regarding small-sized underwater robots, such as underwater vehicles and fish robots, is that they either move autonomously in water or are controlled with a tether connected to a mother ship at the surface of the water body. This is because acoustic modems developed to date are typically too bulky to be mounted in underwater robots. If it were possible to transfer data wirelessly during operation, the effectiveness of the system would increase significantly. This is

our motivation to propose an underwater robot system where a robot contains an acoustic communication module as illustrated in Figure 1a. In the presented operational scenario, a robot sends the collected underwater data or is controlled in real time via an acoustic link. In the next section, the requirements of an acoustic modem for small-sized underwater robots are investigated in detail.

Underwater Mobile Sensor Network System

Figure 1b depicts a mobile system model that monitors underwater environments in real time. The system consists of a docking station and three bio-inspired fish robots. The docking station contains an acoustic modem to communicate with the fish robots underwater and a gateway that controls the radio frequency (RF) communication to terrestrial networks. It is also equipped with docking, drying, cleaning, and recharging modules for fish robots. In order to locate the robots, an ultra-short baseline (USBL) transducer is installed in the docking station. Furthermore, each fish robot is equipped with a thrust module, underwater sensors, a micro-modem, a USBL transponder, a global

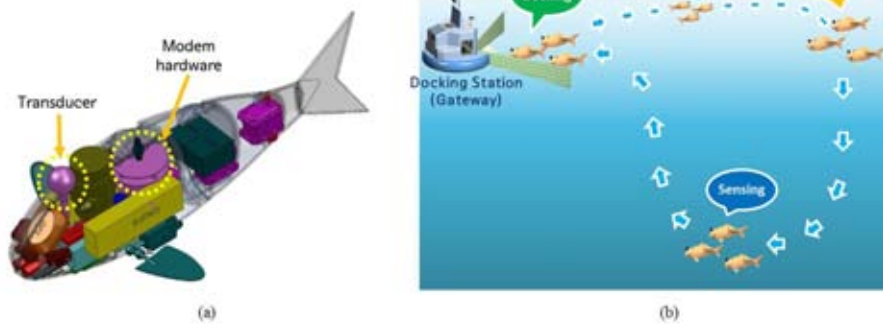
positioning system module, and battery packs.

The system operates as follows: Once a user located on shore gives a command for underwater monitoring, the command is delivered via an RF communication link to the gateway located in the docking station. Then, three robots navigate to a designated waypoint near the surface of the water. After arriving at the point, they submerge deeply in the water, sense environmental data, and send the data through an acoustic communication channel. When the assigned mission is complete, the fish robots may return to the docking station for cleaning and recharging or they may navigate to another place in order to gather data according to a user's command.

The specific procedure of the acoustic communication between the docking station and the three fish robots is as follows: Whenever the docking station needs to transmit data to the fish robots or to receive data from the fish robots, it sends a broadcast message to synchronize the entities participating in the communication system. After the initial broadcasting period, four time slots are sequentially and exclusively dedicated to the gateway, the first fish robot, the second

FIGURE 1

Underwater mobile communication systems.



fish robot, and the third fish robot. In this manner, each entity sends control or monitoring data during its own time slot through a single acoustic channel.

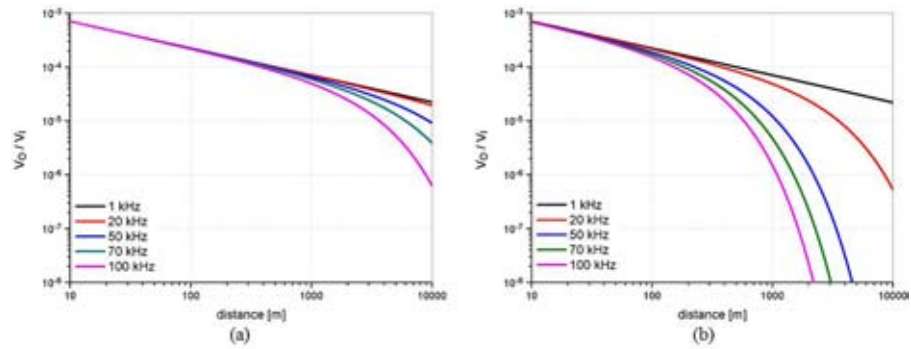
Research Challenges Transducer

The most critical problem in the development of a micro-modem for an underwater robot arises from the transducer that is used to convert electric signals into acoustic waves and vice versa. The two main properties required for a transducer to be adopted in a robot are omnidirectionality and tiny size. In order to support acoustic communication irrespective of the position and orientation of the robot, the use of a spherical transducer, which has an omnidirectional radiation pattern but presents a lower efficiency compared with directional transducers, is an indispensable option. Furthermore, the spherical transducer must be as small as possible, because a large transducer aperture is liable to disturb the natural movement of a robot because of the shape and weight of the transducer. As a result, because the resonant frequency of a transducer is inversely proportional to its size, we have no choice but to use a high-frequency carrier.

Figure 2 shows the ratio of the output voltage (V_O) of the transducer at the receiver to the input voltage (V_I) of the transducer at the transmitter as a function of carrier frequency and distance between the two transducers. For both subgraphs, cylindrical spreading (Kinsler et al., 1999), 10°C, pH 7, and -53 dB transducer loss for sounding and listening are assumed. Salinity is assumed to be 0 in Figure 2a and 35‰ in Figure 2b to reflect fresh water and seawater, respectively. From the results, it is obvious that the loss in signal strength increases significantly

FIGURE 2

Loss in signal strength with respect to distance and frequency in underwater channels. (Color version of figures are available online at: <http://www.ingentaconnect.com/content/mts/mts/2016/00000050/00000002>.)



with the increase of frequency as the distance exceeds approximately 1,000 m in fresh water and 100 m in seawater. In other words, the carrier frequency becomes a crucial factor of concern beyond 1,000 m in fresh water and 100 m in seawater under the given conditions. Therefore, if we assume that the underwater mobile communication systems described above are operated at a distance of several hundred meters in salty water, the acoustic wave emitted from a small-sized transducer having a high resonant frequency will experience a large loss as a result of absorption.

Underwater Channel

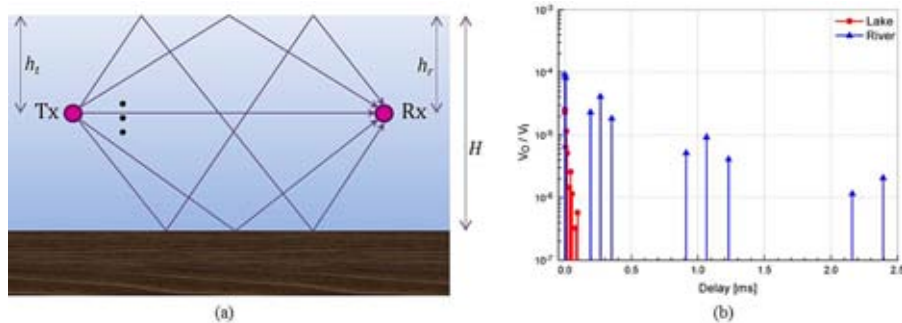
The ray tracing model is one of the widely used propagation models for underwater acoustic signals in which sound energy is considered as a set of propagating rays in a fluid with a constant sound speed. According to the ray tracing model, a received signal is represented as the superposition of multiple rays, as depicted in Figure 3a. The signal strength of each ray is affected by spreading and absorption in water, transducer loss, and reflection coefficients (Chitre, 2007). For example, the delay spreads under conditions modeling a salty lake and a river that will be further discussed in a later sec-

tion are provided in Figure 3b. Cylindrical spreading, a carrier frequency of 70 kHz, and the distance of 500 m are assumed for simulation. Reflection losses at the water surface and at the bottom are chosen to be 0.5 and 6.0 dB, respectively. The water depth H and the depths of transmitter and receiver, h_t and h_r , are set to 2 m, 0.5 m, and 0.5 m for the result in the lake, whereas they are set to 10 m, 1.5 m, and 1.5 m for the result in the river. The salinity in the lake is 35%, whereas that in the river is 0. In addition, only the paths within six reflections at the surface and the bottom are included in the results for simplicity. A key observation is that the delay of each path decreases as the ratio of the distance to the water depth increases. Since this ratio is relatively high in the lake, the delay spread becomes narrower when compared with the result made in the river. Thus, if the channel were sufficiently static, a data rate of a few kilobits per second could be achieved in the lake. It is also seen that the signal strength of the dominant path in the lake is much smaller than that in the river, owing to the increase of absorption by salinity as shown in Figure 2.

In addition to the static attenuation described above, an acoustic wave

FIGURE 3

Underwater channel modeled using ray tracing method.



traversing water suffers from ambient noise generated by aquatic organisms and natural phenomena in the water. Surface agitation by wind is another factor to consider because it makes the reflection of acoustic waves at the surface irregular. Thus, in a harsh environment where a channel is time-varying as a result of the complex combination of all natural and artificial causes, it is impractical to analyze a channel theoretically. More information on underwater acoustic channels for general purposes can be found in Stojanovic and Preisig (2009).

Modem Characteristics

In addition to the issues presented by the transducer and the underwater channel, many other challenging issues must be considered in the development of a micro-modem. One of them is modem size. Because the length of underwater robots can be on the order of tens of centimeters, the modem size should be as small as possible so that the modem can be contained in a robot. Furthermore, a fish robot having a streamlined shape and a couple of articulated joints restricts the modem size significantly as illustrated in Figure 1a. A communication protocol for data exchange in an underwater channel must also be designed. Because the data carried un-

derwater is normally short and bursty, a packet-based protocol is preferred because of its efficiency. On the other hand, the data rate and working range are not critical matters when considering the architecture and requirements of small-scale underwater mobile communication systems.

Micro-Modem

For efficient data transfer in an underwater channel, acoustic transmission technologies suitable for an application should be defined carefully. In this section, we present a simple protocol targeted for systems executing intermittent acoustic communication, such as an underwater environment monitoring system with biomimetic fish robots. Figure 4a shows a physical layer frame format designed for the support of packet-based

acoustic communication. The physical layer header consists of a preamble, a start-of-frame delimiter (SFD), and a frame length field; it is followed by data of variable length. Bearing in mind that underwater sensing data or robot control data are typically short in length, we allocate 255 bytes for the maximum length of data that corresponds to 1-byte frame length. Additional fields can be appended if required.

The symbol structure used to generate a modulated signal is illustrated in Figure 4b. Because the size of the micro-modem is highly restricted as a result of the small size of the fish robot, a binary modulation with non-coherent detection that requires a simple structure and low computational complexity is implemented. In order to mitigate the effect of intersymbol interference (ISI) caused by the delay spread in an underwater acoustic channel, the transmitting time (T) is followed by the guard time (T_G) for each symbol duration (T_S). Therefore, the sinusoidal carrier is generated during T and no signal is generated during T_G for the transmission of information bit “1,” whereas no signal is generated during the whole T_S for the transmission of information bit “0.”

Figure 5 is an actual image of the implemented modem hardware. For ease of loading into a fish robot, it is

FIGURE 4

Frame format and symbol structure.

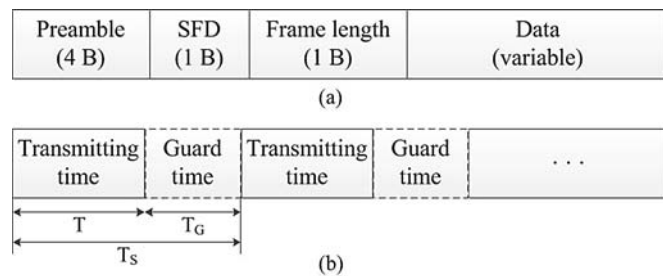


FIGURE 5

Micro-modem.



designed as a cylindrical shape that is assembled by stacking up three circular boards—a digital board, an analog transmission board, and an analog reception board. The digital board provides frame generation and recovery and controls the interface with analog boards and the other devices that act as upper layers. In the analog transmission board, a modulated signal is amplified up to 300 V peak-to-peak and then fed to a transducer. Analog signal processing for detection including amplification and bandpass filtering is performed in the analog reception board. For this application, a tiny spherical transducer having an omnidirectional radiation pattern whose resonant frequency and diameter are 70 kHz and 34 mm, respectively, is utilized. The transducer is directly connected to the modem hardware to complete a micro-modem. The main features of the developed micro-modem are summarized in Table 1.

Performance Evaluation

Gyeongpo Lake and the Han River were used as test sites for the outdoor experiments, as shown in Figure 6. Gyeongpo Lake, located in Gangneung, Republic of Korea, is 1.6 km wide and 0.7 km long and has a maximum depth of 2 m. Connected to the Pacific Ocean

TABLE 1

Specifications of micro-modem.

Feature	Description
MCU	STM32F103 (Cortex-M3)
Modem size ($\Phi \times H$)	70 × 40 mm
Transducer size (Φ)	34 mm
Resonant frequency	70 kHz
Transducer loss	-53 dB
Interface	UART, SPI, USB
Supplied voltage	14.8 V/29.6 V
Power consumption	8 W

through a small waterway, it contains many aquatic plants and marine life that form a colony. Normally, the flow of water is calm except for an occasional surface agitation caused by wind. The other site is a confluence point of two streams of the Han River near Seoul. The width and maximum depth of the river are approximately 500 and 10 m, respectively. As expected, the water becomes shallower as it approaches the riverbank. The flow velocity in the quiet state is approximately 1 knot. Small piers at the lakeside and the riverside are utilized as the main bases for the experiments.

In accordance with the amount of data that is gathered by and transferred to one fish robot at a time, 16 bytes are allocated to the data field in the frame

format for the experiments. According to the primary experiments, the output level of the transducer at the transmitter increases gradually and reaches a steady state after five cycles of a 70-kHz sinusoid. Thus, not only to ensure the normal operation of the transducer but also to maximize the avoidance of inter-symbol interference caused by multipaths, the transmitting time T is set to five cycles of a 70-kHz sinusoid. The rest of the symbol duration is entirely dedicated to the guard time. For example, when the data rates are 1 and 5 kbps, the ratio of T to T_S becomes 5/70 and 5/14, respectively.

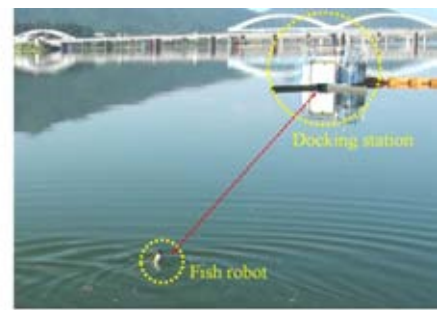
In order to examine the feasibility of the developed micro-modem, point-to-point communication tests were conducted. In the lake and river

FIGURE 6

Experimental environments.



(a)



(b)

experiments, a modem was placed at a pier and another modem was located at a boat. For the sake of convenience, transducers were submerged only at 0.5 and 1.5 m below the surface of the lake and the river, respectively. According to the experiments, acoustic communication was possible up to a data rate of 5 kbps in the lake and 1 kbps in the river at a distance of 500 m, as is expected to some extent from the ray tracing model shown in Figure 3b.

The system level prototype described in Figure 1b was deployed in the river for the integration tests. First, a functional test on the underwater acoustic communication system was performed using a surface gateway and three underwater nodes without fish robots to establish the integrity of the underwater communication network. After that, a communication test with the gateway and one fish robot equipped with the micro-modem was conducted to confirm reliable underwater acoustic communication for a moving object. Finally, a system level experiment conforming to the whole scenario explained in the previous section was executed.

Conclusions and Future Direction

In this article, we outlined the use of underwater mobile communication systems where biomimetic fish robots act as moving nodes. We determined that providing mobility for a small node gives rise to serious restrictions on the design of the acoustic modem, and we conducted a review of the underwater channel characteristics that relate to short-range acoustic communication. Based on these observations, we explored acoustic transmission techniques for the application of under-

water mobile communication systems and developed a prototype of a micro-modem. According to the modem level and system level experiments carried out in a lake and a river, the proposed system equipped with the micro-modem is a viable option.

Owing to the mobility of underwater mobile communication systems, service coverage could be enlarged or easily reconfigured with a small number of mobile nodes; this translates into system and cost efficiencies. Beyond the discussions presented in this article, it may be worthwhile to investigate methods to improve the performance of the micro-modem using high-speed integrated circuits dealing with advanced transmission and reception techniques. We believe that the discovery and deployment of new convergent systems utilizing underwater robots with embedded micro-modems are also challenging issues to be addressed.

Acknowledgment

The authors wish to thank Ocean Sensor Network System Technology Research Center at Gangneung-Wonju National University and Korea Institute of Industrial Technology for contributions to this article. This work was supported in part by Korea Research Council for Industrial Science and Technology (B551179-10-02-00, Development of Bio Mimetic Robot System) and in part by Mid-career Researcher Program through NRF grant funded by the MSIP (2014R1A2A2A01006205).

Corresponding Author:

Sung-Joon Park
Digital Communications Lab.
Department of Electronic Engineering,
Gangneung-Wonju National University

7 Jukheon-gil, Gangneung,
Gangwon 25457, Republic of Korea
Email: psj@ieee.org

References

- Akyildiz**, I.F., Pompili, D., & Melodia, T. 2005. Underwater acoustic sensor networks: research challenges. *Ad Hoc Netw.* 3(2): 257-79. <http://dx.doi.org/10.1016/j.adhoc.2005.01.004>.
- Chitre**, M. 2007. A high frequency warm shallow water acoustic communication channel model and measurements. *J Acoust Soc Am.* 122(5):2580-6. <http://dx.doi.org/10.1121/1.2782884>.
- Freitag**, L., Grund, M., Singh, S., Partan, J., Koski, P., & Ball, K. 2005. The WHOI micro-modem: an acoustic communications and navigation system for multiple platforms. In: *Proceedings of IEEE OCEANS*. Washington, DC: IEEE. <http://dx.doi.org/10.1109/oceans.2005.1639901>.
- Kinsler**, L.E., Frey, A.R., Coppens, A.B., & Sanders, J.V. 1999. *Fundamentals of Acoustics*. Hoboken, NJ: John Wiley & Sons. 548 pp.
- Lee**, W., Jeon, J.-H., & Park, S.-J. 2014. Micro-modem for short-range underwater communication systems. In: *Proceedings of MTS/IEEE OCEANS*. St. John's, Canada: IEEE. <http://dx.doi.org/10.1109/oceans.2014.7003208>.
- Pandya**, S., Engel, J., Chen, J., Fan, Z., & Liu, C. 2005. CORAL: miniature acoustic communication subsystem architecture for underwater wireless sensor networks. In: *Proceedings of IEEE Sensors*. Irvine, CA: IEEE. <http://dx.doi.org/10.1109/icsens.2005.1597661>.
- Stojanovic**, M., & Preisig, J. 2009. Underwater acoustic communication channels: propagation models and statistical characterization. *IEEE Communications Magazine.* 47(1):84-9. <http://dx.doi.org/10.1109/MCOM.2009.4752682>.
- Streitlien**, K., Triantafyllou, G.S., & Triantafyllou, M.S. 1996. Efficient foil propulsion through vortex control. *AIAA J.* 34(11): 2315-9. <http://dx.doi.org/10.2514/3.13396>.

Characteristics of Microstructure Turbulence Measurements With a Moored Instrument in the South China Sea

AUTHORS

Xin Luan

Xiuyan Liu

Hua Yang

Shuxin Wang

College of Information
Science and Engineering,
Ocean University of China

Guojia Hou

College of Information Engineering,
Qingdao University

Dalei Song

College of Engineering,
Ocean University of China

ABSTRACT

A newly designed autonomous instrument was evaluated for long-term ocean turbulence measurements in the South China Sea from October 19, 2013, to February 10, 2014 at 21°09.90'N, 117°42.03'E. A shear velocity time series was collected continuously for 115 days at a single depth of 250 m using two orthogonal shear probes (PNS06). The mechanical design of wings is developed for an observation platform to achieve characteristics of stability and flexibility of current direction tracking. The depth and pitch in comparison with ambient current speed are analyzed, and the results indicate that the platform has satisfied stability requirements for turbulence measurement. The comparison between the instrument heading and current direction shows that the instrument flexibly responds to variations of ambient currents. Throughout the observation period, 62% of the data sets is of significant correlation with correlation coefficients above 0.5, and 4% is of strong correlation. The shear velocity spectra correspond well to the theoretical Nasmyth spectrum, and the magnitude of dissipation rates estimated from shear is approximately $0(10^{-8}) \text{ W kg}^{-1}$. The moored instrument is functional as designed and provides a reliable observation platform for extended turbulent measurements.

Keywords: turbulence measurements, moored instrument, stability, flexibility, shear spectra

Introduction

Ocean turbulence plays an important role in improving our understanding of the effect of the turbulence mixing process on ocean circulation dynamics and significantly improving climate models. It also significantly impacts the research of ocean dynamics, energy exchanges, the marine ecological environment, and the distribution of suspended materials (Nikurashin & Ferrari, 2010). Ocean turbulence has received considerable attention in the last few decades and has become a popular subject in marine science research. Measurements of the turbulence mixing process are usually limited to surveys of short duration and incomplete and sporadic samples in time and space (Thorpe, 2005). Measurements of dissipation rates of turbulent kinetic energy (TKE) over extended

periods yield a valuable data set that provides quantitative assessments of dissipation rates and turbulent mixing level; the technologies for long-term measurements are therefore increasingly important.

Conventionally, ocean microstructure turbulence is measured by fast response thermistors or two orthogonal airfoil shear probes measuring horizontal or vertical shear components (Lueck et al., 2002). Use of a microstructure profiler with shear probes is a common method to measure shear velocity data. However, the traditional profilers, whether horizontal or vertical, require fairly intensive labor and highly trained personnel; it is there-

fore impossible to collect long-term time series due to financial and logistical constraints (Lueck et al., 1997). By altering ships and scientific personnel, the longest time series lasted 30 days and cost more than \$1 million with conventional profilers (Moum et al., 1995). Depending on the advantages of not requiring professional and technical personnel, the moored system makes it possible to take unattended turbulent observations. The earlier research of moored microstructure measurements was reported by Lueck et al. (1997). They used four shear probes and three pairs of Seabird sensors to measure shear and fast temperature in the dissipation range of the

wavenumber spectrum. This moored platform obtained a long time series of turbulence measurements at a reduced cost for personnel and ship time. Lueck and Huang (1999) deployed a moored instrument in a swift tidal channel by using shear probes and FP07 thermistors to measure shear velocity and temperature fluctuations; the profilers collected time series of ocean turbulence at a fixed depth for only 8 days. Song et al. (2013) designed the mooring turbulence observation instruments that implemented continuous observation at a fixed level in the Kiao-chow Bay for several days. By comparing shear probes with microstructure profiles MSS60, it was shown that the moored system was reliable to detect the microscale turbulence, but not for long-term series measurements. An autonomous instrument (Fer & Paskyabi, 2014) was located in a wave-affected layer. Only the velocity spectra in the dissipation subrange can be used for dissipation rate calculations; the shear spectra in the inertial subrange are severely contaminated by platform vibration, and the temperature gradient spectrum in the dissipation subrange is not satisfactorily resolved. While limited to a single depth, the measurement systems collected time series for 3 weeks continuously. The latest work reported by Lueck et al. (2015) was successfully deployed over a 2-week period in Islay Sound; the flow speed exceeded 3 m/s, and the depth of this channel was 53 m. These environmental conditions represented significant challenges for the design of the mooring measurements. In this article, we report on microstructure turbulence measurements at dissipation scales from a newly designed moored system in the South China Sea (SCS). It was deployed at an approximately 250-m depth in water

column and was less contaminated by wave orbital velocities and the interference of platform motion. The moored instrument has continuously collected data for 115 days with a giant storage capacity, which represents significant challenges for extended observations of turbulent dissipation.

The outline of this article is as follows. The sections of instruments and experiments mainly describe experimental equipment and environmental conditions, followed by the proposed method to normalize the measured data between the heading and current direction. Subsequently, the results and discussion mainly show the characteristics of the moored instrument including the stability, flexibility, and spectral analysis of the microstructure shear velocity data. The conclusion presents some additional measures to improve the mechanical design of the system.

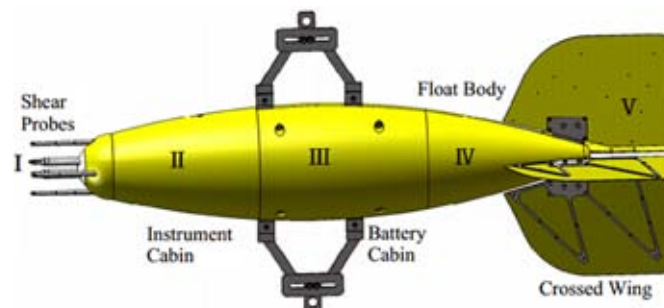
Instruments Mechanical Structure

The moored turbulence measuring instrument (MTMI; Figure 1) is an ocean turbulence measurement system designed to collect microstructure shear time series at a fixed level. The mechanical structure of the MTMI mainly includes five divisions: the nose

section, the instrument cabin, the battery cabin including rechargeable alkaline battery packs, the latter float body made of buoyancy materials, and the crossed wings. The nose section is a semicircular head, in which two orthogonal shear probes (PNS06; Wang et al., 2014) are mounted to measure fluctuations of cross-stream velocity ($\partial w / \partial x$, $\partial v / \partial x$) and hydrodynamic lift force induced by the ambient turbulent flow. Four guard rings are attached to protect the shear probes from being damaged during the experiments. The main circuit boards and attitude sensor (MTI) measured three-axis acceleration signals (A_x , A_y , A_z), and the motion behaviors of the instrument (heading, ψ ; pitch, θ ; and roll, ϕ) are installed in the instrument cabin. The MTMI is powered by battery packs, each rated for 40 Ah at 9-V DC, providing an estimated operating time of approximately 6 months. Balance weight is contained in the latter float body; the horizontal and vertical tails contained in the wings are used to maintain balance and control the direction of the main floating body under the sea. Particularly, the crossed wings make it possible for the MTMI to track variations of current direction and to maintain its position counter to the coming flow. The instrument is a low-drag buoy that can be used as the

FIGURE 1

Mechanical features of the MTMI.



upper buoyancy element or integrated at the desired depth in a mooring line. To obtain accurate turbulence signals, the platform should be stable under severe interference (termed anti-interference) and responds rapidly to changes of current direction. Therefore, the structure of the MTMI is designed to be streamlined to reduce resistance. The assembled MTMI weighs approximately 254.9 kg, with a net buoyancy of 12 kg in seawater. It has an overall length of 3.0 m and a maximum diameter of 50 cm. The maximum working depth of the whole MTMI is 4,000 m, which complies with requirements for working in the deep sea.

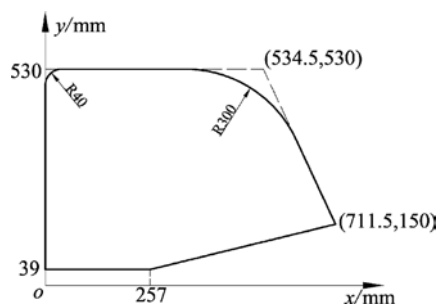
To permit the instrument heading to rotate in response to changes in current direction, the hydrodynamic torque of the wings' force must be larger than the heading force, which depends on the mechanical structures of the main body and the wings of the instrument. According to the requirements of fluid mechanics, the wings of the MTMI are designed to be cruciform, and two vertical and horizontal fins of the wings are separated in this experiment. The crossed fins at the rear provide the torque for rotation and stabilize the pitch motions. The area of countering flow for one fin is approximately $2.75 \times 10^5 \text{ mm}^2$ (Figure 2), and the torque of the wings has been programmed to force larger than the heading force. In short, the streamlined body and crossed wings contribute to improving the stabilization and flexibility of the platform.

Coordinate System

The MTMI system is a right-handed Cartesian coordinate system that has the following axes: x , which is along the major axis of the instrument and is positive pointing forward. The y axis

FIGURE 2

Size of each fin of the wings.



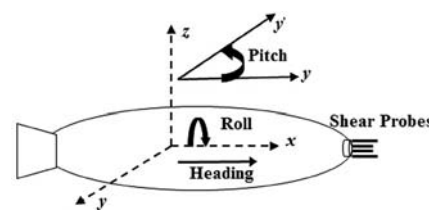
points to the port side of the instrument and is positive athwartship, and z is directed positive upward (Figure 3). Accordingly, the instrument heading (ψ , rotation around the z axis) is positive counterclockwise, ranging from -180° to 180° . Pitch (θ , rotation around the y axis) is positive when the nose is down, ranging from -90° to 90° , and roll (ϕ , rotation around the x axis) is positive when the instrument rolls port side up, ranging from -180° to 180° . For nonzero values of pitch and roll, the vertical axis is not aligned with the acceleration of gravity g . The MTI motion sensor mainly records the three-axis accelerations of the A_x , A_y , A_z , and these three acceleration signals also follow the above coordinate system.

Experiment Deployment

The moored instrument MTMI was deployed in the SCS on October

FIGURE 3

The right-handed Cartesian coordinate system of the instrument and rotation for pitch (θ), roll (ϕ), and heading (ψ).



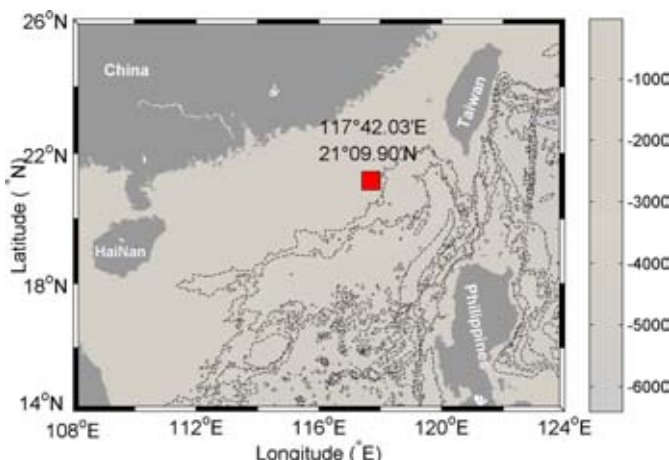
19, 2013, and recovered on February 10, 2014, at $21^\circ 09.90'N$, $117^\circ 42.03'E$ (Figure 4). It was anchored at a depth of approximately 250 m in the SCS; this method of deployment was similar to other moorings. First, the instrument was lowered into the deep water, followed by the flotation sphere. Subsequently, the remainder of mooring line was deposited under tension until the anchor had boarded the ship. During the experimental period, the instrument MTMI had already sampled 28.5 GB of turbulence shear voltage data for a continuous 115 days that yielded a valuable database for further research of the turbulent dissipation and evolution processes in the SCS.

The Mooring System

The whole mooring system used for long-term ocean turbulence observation can be divided into four subdivisions (Figure 5) based on their different uses. The Sea-Bird Electronics (SBE37SM-RS232) CTD sensor and the MTMI are attached in part I. The CTD system mainly records the water temperature, conductivity, and depth of the MTMI. The instrument MTMI is assembled for observing microstructure shear velocity fluctuations. To stabilize the observation platform, a turbulence instrument needs to be embedded in the streamlined floating body made of buoyant glass microsphere material. Part II contains the Doppler current meter (RCM 11) measuring the ambient current speed (cm/s) and current direction ($^\circ$) in the deep sea. Measurements are compensated for instrument tilt and referred to magnetic North by using an internal solid state compass. A microprocessor computes vector-averaged current speed and direction over the last sampling interval. An

FIGURE 4

Map showing the deployment region and the location of the MTMI at 21°09.90'N, 117°42.03'E (red square).



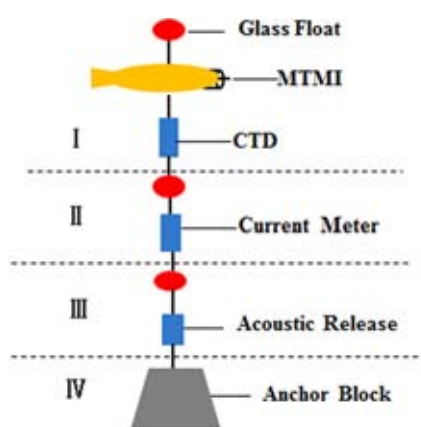
acoustic release in part III is utilized to recover the moored instrument MTMI. The last part is the anchor block, providing gravity for the whole system to make the instrument be in equilibrium. When the acoustic release receives instructions to release the anchor block, the system will float up driven by the buoyancy elements. The MTMI is located at a depth of approximately 250 m, and several groups of glass floats provide buoyancy, keeping the submerged

buoy straight together with the anchor at the bottom.

In a general diagram of the moored system (Figure 5), the whole system weighs 1636.13 kg including approximately 1,000 kg of gravity anchor. Its static buoyancy in water is 190.41 kg, and the mooring line is 300 m long. The type and layout of the instruments can be flexibly adjusted according to the actual situation. A variety of ocean instruments are hung in the submerged buoy, and the distributions of the equipment are ordered at a certain depth.

FIGURE 5

General diagram of the whole mooring system as deployed in the SCS.



Sampling

The battery packs are configured in cyclic sampling, which can supply enough power to allow the MTMI to operate at predetermined intervals. The duty cycle of the moored instrument is 3 min on and 12 min off. The sampling rate of shear sensor is set to 1,024 Hz, and the MTI sensor is set to 120 Hz, which is mounted by a right-handed coordinate. The sampling interval of RCM and the Sea-Bird CTD system is set to 60 s.

Data are recorded in 16 CompactFlash memory cards, with a capacity per card of 16 GB.

Methodology Data Normalization

According to the requirements of turbulence observations, platform motion features are analyzed by using the experimental data for turbulence detection; the instrument has been greatly improved after several tests in the coast. In the design of the moored turbulence observation instrument, the system balance and the rotation in response to changes in the direction of flow orientations are two significant parameters; thus, an effective analysis method is necessary to illustrate the rational design of the turbulence platform. Accordingly, the instrument heading is positive counterclockwise, ranging from -180° to 180° , but the samples of current direction acquired by RCM are positive clockwise, ranging between 0° and 360° . Due to their different sampling rates and ranges between the MTI motion sensor and the RCM, we need to normalize the two data arrays of the heading and current direction before processing and analyzing them. First, the values of the heading will be rotated 180° to normalize with the current direction in the same range of 0° – 360° .

Second, the sample rates of the heading signals will be changed by resampling them as averaged in 3-min segments in which there are more than 20,000 points. During the resampling process, an anti-aliasing or low-pass finite impulse response (FIR) filter is applied to compensate for the filter's delay; it provides an easy-to-use alternative method, relieving the user's need to supply a filter or compensate for the signal delay introduced

by filtering. Finally, a statistical average method is used to process the normalized data between heading and current direction. Actually, the average method is an arithmetic average, which has the advantage of simplicity and practicality in calculating average values. Although this method may result in some deviation between predicted values and the actual values, it does not affect long-term observations of tracking the current direction due to the large amount of heading data.

Correlation Analysis

The correlation analysis is a statistical method to describe statistical relationships between two or more random variables or observed data values. It can be interpreted as a correlation coefficient that illustrates a quantitative measure of some type of correlation and dependence. The variations of correlation coefficients are always between -1 and $+1$. If two variables are perfectly related in a positive linear sense, the correlation coefficient is equal to $+1$. On the contrary, a correlation coefficient of -1 indicates that two variables are perfectly related in a negative linear sense. When the coefficient is zero, it suggests that there is no linear relationship between the two variables. Different values of correlation coefficients indicate the different related levels between two variables (Cheng et al., 2006; Sandomirski, 2015). To develop the MTMI's flexibility to track the changes of current direction, canonical correlation analysis (CCA) is introduced to analyze the correlation between the current direction and heading. If the obtained data tend to co-occur in two arrays, they are highly correlated and tend to be combined into a single dimension in the new space. We can try to find projections of each representation separately

such that the projections are maximally correlated. The correlation coefficient ρ is given as in Equation (1).

$$\rho_{X,Y} = \text{corr}(X, Y) = \frac{\text{cov}(X, Y)}{\sigma_X \sigma_Y} \quad (1)$$

where X and Y are two variables in matrices or vectors of the same size. Conventionally, the absolute value of a correlation coefficient above 0.5 indicates that the related level between two variables is significant (Lai & Fyfe, 2012). Through the correlation analysis between heading and current direction, it is easy to deduce results about the flexibility of the MTMI to track the variation of current direction.

Results and Discussion

To evaluate the effectiveness of a moored turbulence observation platform, the stability of the instrument at a fixed depth; the angle of attack (AOA), interpreted as the attitude of pitch and roll (Moreau et al., 2005); and the flexibility of tracking current direction are crucial parameters that need to be estimated as accurately as possible for high quality of dissipation rates. In short, the accuracy of measured turbulence data is affected by the stability of the moored system, the platform motion behavior under appropriate environmental conditions, and the flexibility.

Stability of the Platform

The stability of the moored platform mainly includes the variation of depth and pitch with respect to current speed. Thus, the stability of the system is described and analyzed through measured data: depth and pitch, where depth data are acquired by the CTD system and pitch is measured by MTI sensor. Ideally, the

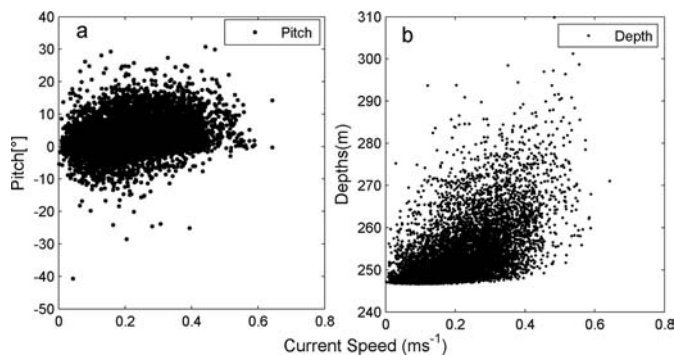
MTMI should be fixed at a point above the anchor. Actually, the instrument is forced by the buoyancy and tension from the mooring line. The evolution of depth and pitch with current speed will stabilize the MTMI. On the one hand, the pitch of the instrument is unaffected by the variations of current speed. With further increases in speed, the pitch ranges about $0^\circ \pm 15^\circ$ (Figure 6a, left). Statistics suggest that, for 85% of the data set throughout the whole observation period, the pitch reaches zero, which indicates that the orientation of the platform is nearly always stable for long-term turbulence measurements. On the other hand, the average depth of MTMI is about 247 m for zero flow. With the current speed increasing, the depth of the instrument ranges from 247 to 270 m (Figure 6b, right). The instrument is located at a fixed depth of approximately 250 m because the mooring line between the anchor and the main float body is extremely tight and the depth limitation of MTMI is determined by the quality of syntactic foam. In summary, the pitch is unaffected by current speed from large-scale time series, and the platform is always moored at an approximate depth of 250 m. The whole moored system has satisfied the measured requirements for stability with an appropriate design for turbulence observations.

Platform Behavior and Accelerations

The acceptable quality of turbulence measurements is limited to a small subset of environmental conditions—the flow speed, the AOA, and platform vibration accelerations. The time series of current speed measured by the RCM instrument during the time-extended deployment indicates that the environmental conditions

FIGURE 6

Large-scale time series of pitch and depth in comparison with current speed. (a) Time series of pitch with current throughout the whole observation period of 115 days. (b) The location of the moored instrument in SCS for 115 days is assessed by depth data measured by the CTD system and current speed measured by the RCM instrument.



ranging from 0.1 to 0.42 m/s is relatively stable. In addition, the average horizontal current speed past sensors is about 0.24 m/s (Figure 7a), which is sufficiently greater than an estimate of the turbulent velocity. A good estimate of the AOA time series felt by shear probes will allow for reliable calculation of dissipation rates (ε) of turbulent energy. When the AOA is smaller than $\pm 20^\circ$, the output of shear probes can respond linearly to cross-stream velocity fluctuations times the horizontal velocity U (Paskyabi & Fer, 2013). In this article, the AOA can be interpreted as the instrument behavior that is gauged by the variations of pitch and roll (Lueck & Huang, 1999). Time series of pitch and roll is roughly considered as constant with the average values of $\theta = 4.5^\circ$ and $\phi = 5.44^\circ$, respectively, in 6 days (Figure 7b). Throughout the long-term observation period, the variations of pitch and roll of the instrument are relatively at zero for large-scale turbulent measurements. The vibrations and accelerations measured by MTI sensor are the other parameters to describe the behavior of the platform and environmental forcing. When the accelerations are scaled by

current speed, the signals from the longitudinal (A_x) and athwartship (A_y) accelerations (Figure 7c) divided by the speed are always small compared with the shear probe signals.

The Flexibility of Tracking Flow

The alignment of the instrument with the ambient current direction is critical for successful turbulence measurements. We originally intended

to compare the instrument heading against the current direction reported by the RCM. The RCM is rigidly fixed to the instrument, and one axis is always parallel to the shaft of the shear probe, which allows for reliable estimates of turbulence. The ability of the moored instrument to track flow direction refers to the flexibility of the heading rotating in response to variation of flow orientations, which is used to describe the state of the measuring platform. The angle of approximately 180° between heading and current direction indicates that the instrument heading keeps counter to the state of aligning with the coming current direction; that is to say, the axis heading should always be parallel to the changes of current direction (Fer & Paskyabi, 2014; Lueck et al., 1997). Therefore, the flexibility of the MTI responding to the changes of current orientations depends on the instrument heading and the mean ambient current direction. From the perspective of Figure 8, the instrument heading is aligned with the ambient current di-

FIGURE 7

Time series of the attitude sensor and accelerations in January 13–18, 2014, in the SCS experiment. (a) Horizontal current speed measured by RCM. (b) Pitch and roll measured by MTI motion sensor. (c) The longitudinal (A_x) and athwartship (A_y) accelerations.

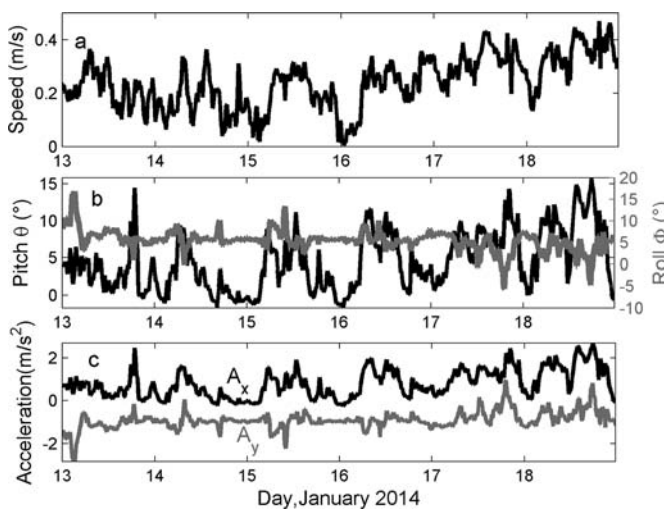
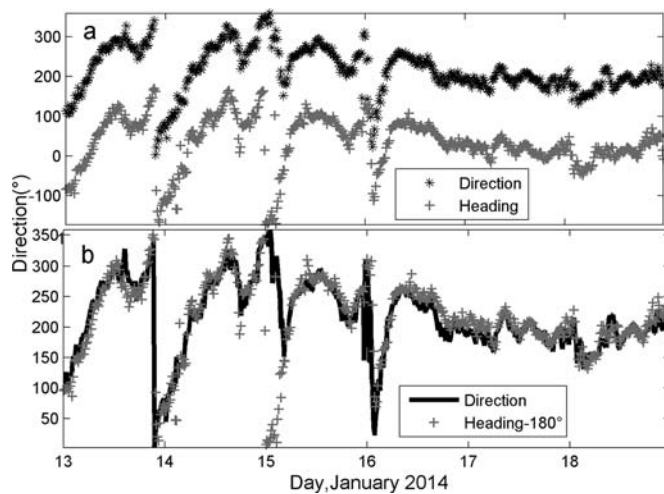


FIGURE 8

The flexibility of the heading rotating in response to variations of the current direction. (a) Current direction measured by RCM (black), and the instrument heading measured by MTI attitude sensor (gray). (b) Current direction (black) in comparison with the heading, which has been subtracted 180° (gray). The correlation coefficient between the heading and current direction is 0.66.



rection, opposing the incoming flow (Figure 8a). For comparison with current direction, the heading has been subtracted 180°, where the horizontal axis of time series is expressed in days and the vertical axis refers to the degree of direction. The black (solid) line is almost overlapped by the gray line (Figure 8b). The absolute difference is lower than 10°, satisfying the requirement of AOA (Fer & Paskyabi, 2014). In addition, the correlation coefficient between the heading and current direction is 0.66 suggesting that their similarity is 66%. The difference between the current direction and the axis of heading is small, which indicates that the moored instrument is applicable to measure ocean turbulence.

The MTMI has been deployed for a total of 115 days in the SCS from October 19, 2013, to February 10, 2014. In addition to some incomplete and sporadic data for 18 days, there are a total of 97 days with complete data samples. A large proportion of correlation coefficient is focused on the range

of 0.50–0.9, and the proportion of all the coefficients is shown in Table 1. For 62% of the data set, the correlation coefficient is above 0.5, indicating a significant correlation relationship between the heading and current direction, and 40% is of high correlation (Table 1). The larger correlation coefficients, the stronger the correlation between the measured heading and current direction will be. The results illustrate that the instrument heading of MTMI has a good flexibility in response to the changes of current direction. In short, under the given

mechanical design, the instruments can respond flexibly to the variations of current and consistently follow the current direction. Throughout the whole observation period, the correlation coefficients between heading and current direction are above 0.5 for 62% of the data set, which means that 62% of the turbulence data are effectively available for the research.

Spectra Analysis

The performance of the moored instrument for measuring turbulent shear velocity is gauged by examining samples of unprocessed data. Generally, wavenumber spectrum is a commonly used method to evaluate the characteristics of turbulence. The shear spectra $\Phi(f)$ in frequency domain are converted into the wavenumber domain by using the Taylor's frozen turbulence hypothesis, where $\Phi(k) = U\Phi(f)$ and $k = f/U$; U is the mean flow velocity. The dissipation rate of the TKE is calculated by integrating the wave number spectrum for assuming isotropic turbulence (Voulgaris & Trowbridge, 1998).

$$\begin{aligned} \varepsilon_i &= 7.5\nu \overline{\left(\frac{\partial u_i}{\partial z}\right)^2} \\ &= 7.5\nu \int_{k_0}^{k_c} \psi_i(k) dk \quad [m^2 s^{-3}] \end{aligned} \quad (2)$$

TABLE 1

The proportion of correlation coefficients and the corresponding degree of correlation between the instrument heading and current direction in 97 days.

Correlation Coefficients (-)	Proportion (%)	Degree of Correlation (-)
0–0.3	19	Weak positive correlation
0.3–0.5	19	Low correlation
0.5–0.7	22	Significant correlation
0.7–0.9	36	High correlation
0.9–1.0	4	Strong correlation

where $\psi_i(k)$ is the shear spectrum measured by shear probe 1 ($i = 1$) and shear probe 2 ($i = 2$), ν ($\nu \approx 1.64 \times 10^{-6} \text{ m}^2 \text{ s}^{-1}$) is the kinematic molecular viscosity as a function of the local water temperature, k denotes the wavenumber, and the overbar denotes a spatial average. The k_0 is the lower integration limit, and the k_c is the Kolmogorov wave number, where $k_c = (\varepsilon/\nu^3)^{1/4}$. The empirical model for the turbulence spectrum determined by Nasmyth (1970) is utilized to set the lower and upper integration limits of the spectrum (Oakey, 1982; Zhang & Moum, 2010). The acceptable measurements of dissipation rate are obtained directly by using the shear probes.

In the wavenumber domain, the variance of the shear resides mainly at wavenumbers between 1 and 100 cycles per meter (cpm; wavelength of 0.01 to 1 m). The noise signals are mainly induced by turbulence eddies, and the phenomenon of a Karman vortex street excludes the disturbance of gravity waves. When the moored instrument is located in the deep ocean to observe turbulence, viscous fluids flow through the bluff body, and the phenomenon of a Karman vortex street is generated behind a circular cylinder in the water

flow field. In short, this phenomenon is indirectly caused by interaction of the mean flow with the cable, and results in vibration signals. The acceleration-coherent vibration can be removed from the shear signals with the technique deduced by Goodman et al. (2006). The rate of dissipation has decreased approximately two times for the mean flow velocity $U = 0.25 \text{ m s}^{-1}$. Both the raw shear spectra (Figure 9, Sh1 and Sh2) and the cleaned spectra (Figure 9, Sh1-clean and Sh2-clean) conform well to the theoretical Nasmyth spectrum in shape and level. The peak of noisy signals in the shear spectra at approximately 24 cpm induced by the Karman vortex street is partly removed using a coherent noise removal algorithm, further proving that the platform is stable for measuring turbulence.

Conclusions

The MTMI was successfully deployed at a depth of approximately 250 m in the SCS. It was demonstrated that effective turbulence data can be measured and collected using the MTMI developed by OUC at a fixed depth for a long-term observation. The results show that 85% of

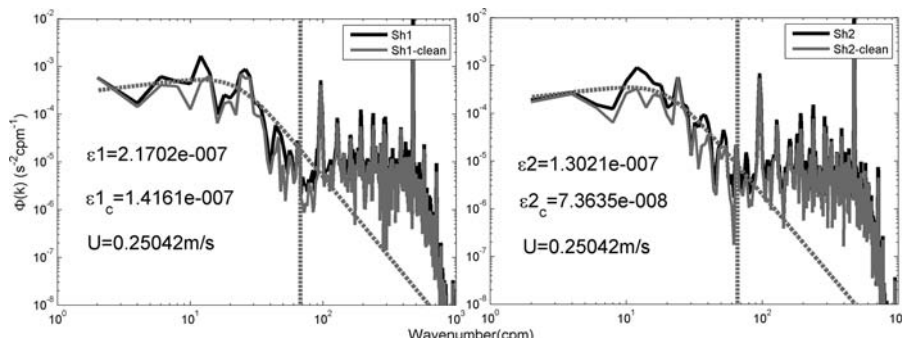
the pitch is unaffected by variations of the current speed from the large-scale time series. For the whole observation period, 62% of the correlation coefficients is over 0.5, demonstrating the significant correlation between heading and current direction. With the given mechanical design, the instrument always keeps a counterflow state and can respond flexibly to the changes of current direction. The magnitude of dissipation rates of TKE estimated from the shear probes is approximately $O(10^{-8}) \text{ W kg}^{-1}$ at a known mean flow speed $U = 0.25 \text{ m/s}$, and the power spectrum curves match closely with the empirical Nasmyth spectrum. The newly designed instrument MTMI has proven to be an effective platform for long-term measurements of microstructure turbulence. In addition, to further improve the stability and flexibility of moored system, the design of the wings needs to be improved in some aspects, such as altering the materials or increasing the area of the wings.

Acknowledgments

This research was financially supported by the National High Technology Research and Development Program of China ("863" Program) under Grant No. 2012AA090901 and Grant No. 2014AA093404, the National Nature Science Foundation under Grant No. 61203070, and the Nature Science Foundation of Shandong Province under Grant No. ZR2012DQ011. We especially thank chief scientist Ji-Wei Tian and professor Z. Daniel Deng for their guidance. We would also like to thank the Ocean University of China for the platform of the vessel *Dong Fang Hong 2* and the entire research and development team for their help with this experiment.

FIGURE 9

Shear spectra of dissipation rates (ε) for 4-s-long segment, where x axis is expressed in wavenumber domain and the y axis is the power density spectrum (PSD). The black and gray lines are the raw shear data and cleaned data of shear probes 1 and 2, the dotted curves are the Nasmyth spectrum, and the vertical dashed line is the Kolmogorov cutoff wavenumber of the integration.



Corresponding Author:

Dalei Song
College of Engineering,
Ocean University of China
Email: songdalei@ouc.edu.cn

References

- Cheng**, Q.M., Jing, L.H., & Panahi, A. 2006. Principal component analysis with optimum order sample correlation coefficient for image enhancement. *Int J Remote Sens.* 27(16):3387-401. <http://dx.doi.org/10.1080/01431160600606882>.
- Fer**, I., & Paskyabi, M.B. 2014. Autonomous ocean turbulence measurements using shear probes on a moored instrument. *J Atmos Ocean Tech.* 31(2):474-90. <http://dx.doi.org/10.1175/JTECH-D-13-00096.1>.
- Goodman**, L., Levine, E.R., & Lueck, R.G. 2006. On measuring the terms of the turbulent kinetic energy budget from an AUV. *J Atmos Ocean Tech.* 23(7):977-90. <http://dx.doi.org/10.1175/JTECH1889.1>.
- Lai**, P.L., & Fyfe, C. 2012. Kernel and nonlinear canonical correlation analysis. *Int J Neural Syst.* 10(5):365-77. <http://dx.doi.org/10.1142/S012906570000034X>.
- Lueck**, R., & Huang, D. 1999. Dissipation measurement with a moored instrument in a swift tidal channel. *J Atmos Ocean Tech.* 16(11):1499-505. [http://dx.doi.org/10.1175/1520-0426\(1999\)016<1499:DMWAMI>2.0.CO;2](http://dx.doi.org/10.1175/1520-0426(1999)016<1499:DMWAMI>2.0.CO;2).
- Lueck**, R., Wolk, F., Hancyck, J., & Black, K. 2015. Hub-height time series measurements of velocity and dissipation of turbulence kinetic energy in a tidal channel. In: Conference of Current, Waves, Turbulence Measurement Workshop (CWTM). Petersburg, FL: IEEE. <http://dx.doi.org/10.1109/CWTM.2015.7098143>.
- Lueck**, R.G., Huang, D., Newman, D., & Box, J. 1997. Turbulence measurement with a moored instrument. *J Atmos Ocean Tech.* 14(1):143-61. [http://dx.doi.org/10.1175/1520-0426\(1997\)014<0143:TMWAMI>2.0.CO;2](http://dx.doi.org/10.1175/1520-0426(1997)014<0143:TMWAMI>2.0.CO;2).
- Lueck**, R.G., Wolk, F., & Yamazaki, H. 2002. Oceanic velocity microstructure measurements in the 20th century. *J Oceanogr.* 58(1):153-74. <http://dx.doi.org/10.1023/A:1015837020019>.
- Moum**, J.N., Gregg, M.C., Lien, R.C., & Carr, M.E. 1995. Comparison of turbulence kinetic energy dissipation rate estimates from two ocean microstructure profiles. *J Atmos Ocean Tech.* 12:346-66. [http://dx.doi.org/10.1175/1520-0426\(1995\)012<0346:COTKED>2.0.CO;2](http://dx.doi.org/10.1175/1520-0426(1995)012<0346:COTKED>2.0.CO;2).
- Moreau**, S., Roger, M., & Jurdic, V. 2005. Effect of angle of attack and airfoil shape on turbulence-interaction noise. In : 11th AIAA/CEAS Aeroacoustics Conference. pp.1-20. Monterey, CA: Airfoil Noise. <http://dx.doi.org/10.2514/6.2005-2973>.
- Nasmyth**, P.W. 1970. Oceanic turbulence. Ph.D. thesis. Department of Physics, University of British Columbia. 69 pp.
- Nikurashin**, M., & Ferrari, R. 2010. Radiation and dissipation of internal waves generated by geostrophic motions impinging on small-scale topography: Application to the Southern ocean. *J Phys Oceanogr.* 40(5):1055-74. <http://dx.doi.org/10.1175/2010JPO4315.1>.
- Oakey**, N.S. 1982. Determination of the rate of dissipation of turbulent energy from simultaneous temperature and velocity shear microstructure measurements. *J Phys Oceanogr.* 12(3):256-71. [http://dx.doi.org/10.1175/1520-0485\(1982\)012<0256:DOTROD>2.0.CO;2](http://dx.doi.org/10.1175/1520-0485(1982)012<0256:DOTROD>2.0.CO;2).
- Paskyabi**, M.B., & Fer, I. 2013. Turbulence measurements in shallow water from a subsurface moored moving platform. *Energy Procedia.* 35(9):307-16. <http://dx.doi.org/10.1016/j.egypro.2013.07.183>.
- Sandomirski**, S.G. 2015. Effect of measurement accuracy and range of variation of a physical quantity on the correlation coefficient. *Meas Tech.* 57(10):1113-20. <http://dx.doi.org/10.1007/s11018-015-0588-3>.
- Song**, D.L., Sun, J.J., Xue, B., Jiang, Q.L., & Wu, B.W. 2013. Mooring system of ocean turbulence observation based on submerged buoy. *China Ocean Eng.* 27(3):369-78. <http://dx.doi.org/10.1016/j.egypro.2013.07.183>.
- Thorpe**, S.A. 2005. The Turbulent Ocean. Cambridge, UK: Cambridge University Press. <http://dx.doi.org/10.1017/CBO9780511819933>.
- Voulgaris**, G., & Trowbridge, J.H. 1998. Evaluation of the Acoustic Doppler Velocimeter (ADV) for turbulence measurements. *J Atmos Ocean Tech.* 15(15):272-89. [http://dx.doi.org/10.1175/1520-0426\(1998\)015<0272:EOTADV>2.0.CO;2](http://dx.doi.org/10.1175/1520-0426(1998)015<0272:EOTADV>2.0.CO;2).
- Wang**, Y.F., Luan, X., Han, L., Yang, H., Wang, S.X., & Hou, G.J. 2014. A de-noising algorithm of turbulence signal based on maximum likelihood. *Mar Technol Soc J.* 48(6):42-51. <http://dx.doi.org/10.4031/MTSJ.48.6.1>.
- Zhang**, Y.W., & Moum, J.N. 2010. Inertial-convective subrange estimates of thermal variance dissipation rate from moored temperature measurements. *J Atmos Ocean Tech.* 27(11):1950-9. <http://dx.doi.org/10.1175/2010JTECHO746.1>.

Study and Design of a Heat Dissipation System in a Junction Box for Chinese Experimental Ocean Observatory Network

AUTHORS

Dejun Li

Jun Wang

Jianshe Feng

Canjun Yang

Yanhui Chen

State Key Laboratory of Fluid Power and Mechatronic Systems,
Zhejiang University

ABSTRACT

Good heat dissipation is highly significant for long-term reliable functioning of a junction box (JB) for a cable ocean observatory network. An innovative heat dissipation system consisting of circumferentially equi-spaced chassis heat sinks and an adaptive elastic support structure is proposed based on the analysis of the cooling mechanism of the JB. A temperature field model of the JB is established. The parameters include seawater pressure, precision of machine workpieces, seawater flow rate, and thermal contact resistance. A 3D dynamic simulation of heat dissipation is conducted using the commercial software ANSYS to describe the temperature field inside the JB. The proposed heat dissipation system is applied and tested on a laboratory setup of the Experimental Underwater Observatory Network System of China. Experimental results agree well with the theoretical model and simulated results. The increase in maximum temperature in the JB is between 7°C and 10°C under different sea conditions.

Keywords: heat dissipation system, ocean observatory network, junction box, temperature field model, contact thermal resistance

Introduction

The ocean covers 70% of the earth's surface and extensively influences the environment. However, the nature of the ocean is poorly understood. Developing a deep understanding of the role of oceans and elucidating the complex physical, biological, chemical, and geological processes operating therein represented a major challenge in the early 21st century (Favali et al., 2015). Cabled ocean observatory networks have been installed to help meet the challenge. These networks provide abundant power and high bandwidth communications to remote-controlled sensors and scientific instruments which gather real-time data and imagery. Some relevant cabled ocean observatory networks have been developed and deployed around the world. North-East Pacific Time-series Undersea Networked Experiments (NEPTUNE) Canada, Monterey Accelerated Research System in America, Dense Ocean Network for Earthquake and Tsunamis in Japan, and European Seafloor Observatory Network in Europe can provide long-

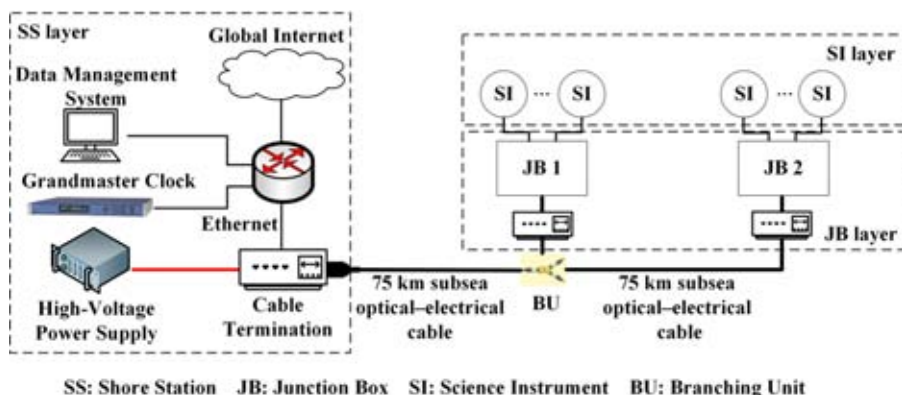
term, real-time, and continuous data (Chave et al., 2004; Priede et al., 2004; Howe et al., 2006; Barnes & Tunnicliffe, 2008; Kawaguchi et al., 2008; Aguzzi et al., 2011). A similar network, the Experimental Seafloor Observatory Network System, has been developed and will be deployed in the South China Sea in the near future. This network is the first attempt at building a regional cabled observatory network in China. The structure of the cabled ocean observatory network, which consists of a shore station (SS) layer, junction box (JB) layer, and terminal science instrument (SI) layer, is shown in Figure 1. Backbone and water-tight cables are used to connect the different layers.

The JB is the intermediate processing unit between the SS and SIs on

the seabed. This layer is responsible for power conversion, communication transmission, and time synchronization. Long-term working reliability of the JB is essential to the normal operation of the entire observatory network under the extreme environment of the deep sea (Chen et al., 2012). In this study, the JB is divided into two sections, namely, power conversion and control cavities. The power conversion vessel is mainly used to realize power conversion and distribution for the whole underwater network. Power consumed by heat dissipation of each power conversion vessel, which is limited by the power conversion efficiency, reaches hundreds of watts at full load operation. Electronic components and instruments generally need a comparatively large and ventilated environment

FIGURE 1

The structure of the cabled ocean observatory network. (Color version of figures are available online at: <http://www.ingentaconnect.com/content/mts/mts/2016/00000050/00000002>.)



for effective heat dissipation. However, the submarine JB is usually designed as a sealed cylindrical cavity. Compact structure and small space occupancy is preferred because of deep-sea working conditions and layout requirements. Therefore, traditional terrestrial heat dissipation technologies cannot be applied in the JB because of the restrictive circumstances. A proper and innovative heat dissipation scheme is designed for the submarine JB through comprehensive heat transfer analysis to meet the demands for a highly reliable and long-term operation.

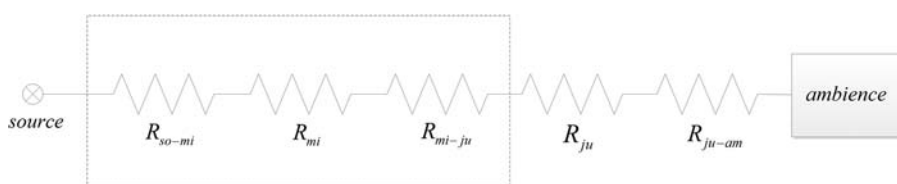
The paper includes six sections. Heat dissipation mechanism and structural design of the JB is presented in Heat Dissipation Mechanism and Structural Design of the JB. Model for the Thermal Conduction of the JB addresses the thermal conduction of the JB model, which mainly includes the mathematical model of the temperature field, calculation model for contact thermal resistance, and computation of the convective heat transfer coefficient. Software simulation analysis is presented in Software Simulation Analysis. Experimental results are shown and analyzed in Experimental Results. Conclusion concludes the study.

retically the fastest means to dissipate heat. However, this scheme is difficult to implement and cannot guarantee system reliability. A good heat transfer medium between heat sources and the interior cylinder wall of a vessel with high thermal conductivity is designed. Thus, an effective heat dissipation scheme for the JB is realized.

The heat dissipation pathway from the internal distribution heat source of the JB to the external seawater is as follows: heat source → interlayer heat transfer medium → cylinder wall of the JB → seawater. Figure 2 shows the thermal resistance network of the designed pathway. R_{mi} and R_{ju} are the thermal resistances of the interlayer heat transfer medium and cylinder wall of the JB, respectively. R_{so-mi} represents the contact thermal resistance between the heat source and the interlayer heat transfer medium. R_{mi-ju} depicts the contact thermal resistance between the interlayer heat transfer medium and the interior cylinder wall of the JB. R_{ju-am} shows the contact thermal resistance between the exterior wall and seawater. R_{so-mi} , R_{mi-ju} , and R_{mi} are related to the thermal conductivity coefficient of the interlayer heat transfer medium. In the “Observatorio Submarino Expandible” (OBSEA) JB (del Río et al., 2013), air is used as the primary medium for heat transfer from the electronic components to the interior wall. R_{so-mi} , R_{mi-ju} , and R_{mi} represent the heat resistance of the natural convection between air and heat sources, between air and the interior wall of the vessel, and the heat resistance of air itself, respectively. The JB of NEPTUNE uses metal, which has considerably higher thermal conductivity than air, as the interlayer heat transfer medium and obtains good heat dissipation effect. The electronic components are mounted onto a chassis (i.e., an inverted T-shaped

FIGURE 2

Heat dissipation pathway of the JB.



structure made of aluminum) for heat dissipation. However, the heat transfer pathway of the T-shaped structure is relatively long, and all the electronic components mounted onto the same structure centralize heat sources at a high local temperature (Woodroffe et al., 2008).

In the proposed design, four circumferentially equi-spaced aluminum chassis heat sinks that coupled well with the interior cylinder wall of the JB are designed to disperse heat. Figure 3 shows the structure of the JB with part of the heat sinks and the internal electronic components. Power converters and other heat sources are fixed onto the heat sinks. High-precision mechanical processing of the heat sink curved base can match properly with the interior cylinder wall of the vessel and allow vertical heat transfer between heat sources and seawater. Microdeformation occurs when the JB is deployed on the seabed at a water depth of 2,000 m. The maximum deformations on the radial and axial directions are approximately

0.225 and 0.732 mm, respectively, according to the finite element analysis. The deformation patterns of the vessel are shown in Figure 4. Therefore, an adaptive elastic support structure is designed to push the heat sinks that are securely attached onto the interior wall of the vessel. The supporting structure can enable the heat sinks to adapt to wall deformation by flexing the springs. This design increases the cooling area of the power converters, shortens the cooling path, and enlarges the available space. Furthermore, compared with the oil immersion heat dissipation method, the proposed method avoids the risks of oil immersion of the electronic components and oil expansion when the oil is heated during the heat transfer process.

Model for the Thermal Conduction of the JB

Figure 5 shows the heat dissipation process of the JB, in which the power converters initially dissipate heat through the chassis heat sinks. The high machining accuracy of the contact surfaces and the high heat conductivity of the aluminum chassis heat sinks make the contact thermal resistance R_{so-mi} sufficiently small, and thus, it can be disregarded. The thermal resistance of the middle-layer medium (chassis heat sinks), R_{mi} , significantly decreases because of the direct vertical heat dissipation path from which the heat sources move outward. Contact thermal resistance R_{mi-ju} between the curved base and the interior wall of the vessel is affected by machining accuracy and normal pressure. Therefore, increasing machining accuracy and spring length can reduce R_{mi-ju} . The values of the thermal resistance of the titanium wall of the vessel R_{ju} and the heat resistance R_{ju-am} between the exterior wall and seawater are fixed. The proposed design can optimize the dissipation performance of the JB.

FIGURE 4

The deformation patterns of the vessel.

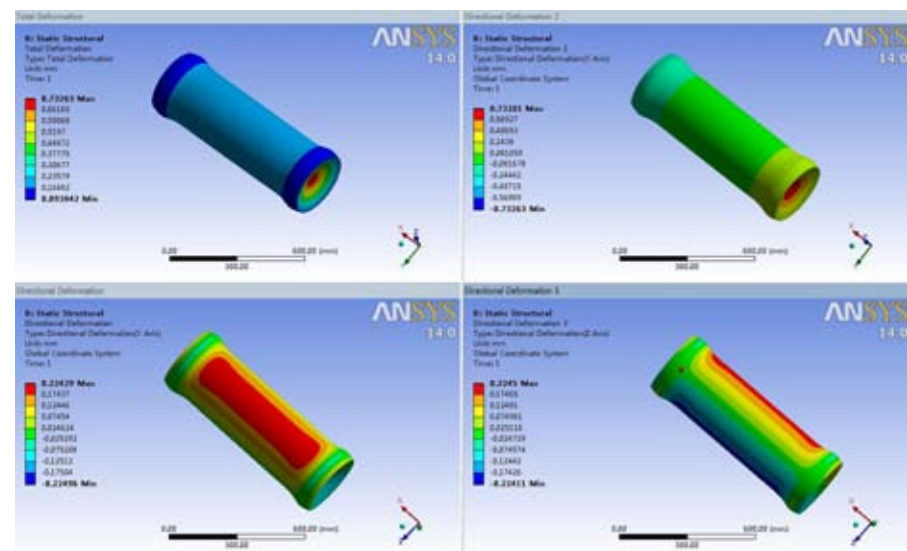


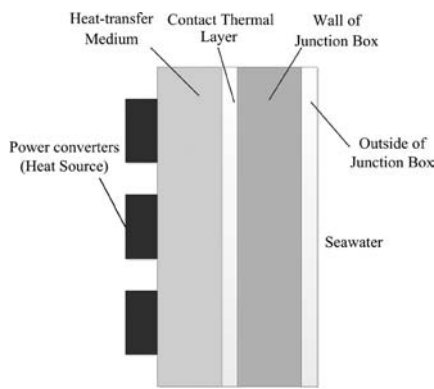
FIGURE 3

Structure of the JB.



FIGURE 5

Heat dissipation of the JB.



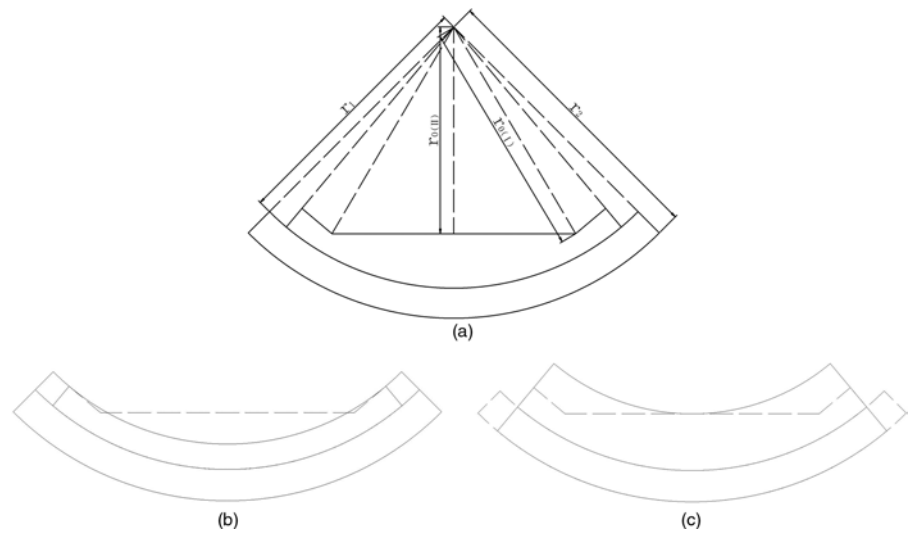
Mathematical Model of the Temperature Field of the JB

Establishing an accurate model for the temperature field is difficult because of the complex structure of the JB. The geometry of the 1/4 cross section of the JB is depicted in Figure 6(a). The squeeze method is adopted to simplify the structure of the JB into two 2D models that consist of multilayer cylinder walls (Figures 6(b) and 6(c)).

The cooling condition of the actual structure is obviously worse than that of the structure depicted in Figure 6(b) but better than that of the structure depicted in Figure 6(c). As shown in Figure 6(b), the heat sinks are evenly distributed on the interior wall of the cylinder and the thickness of the chassis heat sink is decreased. These characteristics reduce thermal resistance. By contrast, Figure 6(c) shows that heat sinks are unevenly distributed on the interior wall of the cylinder and that the thickness of the chassis heat sink is increased. These characteristics enhance thermal resistance. The temperature field models for the cross section in both structures are established according to the heat conduction differential equations and boundary conditions. Thus, the temperature range of the actual structure is determined.

FIGURE 6

(a) The geometry of 1/4 cross section of the JB. (b) 1/4 cross section of simplified model I. (c) 1/4 cross section of simplified model II.



The heat conduction differential equation of the cylindrical coordinate system is as follows (Kays et al., 2012):

$$\rho c \frac{\partial T}{\partial \tau} = \frac{1}{r} \frac{\partial}{\partial r} \left(kr \frac{\partial T}{\partial r} \right) + \frac{1}{r^2} \frac{\partial}{\partial \varphi} \left(k \frac{\partial T}{\partial \varphi} \right) + \frac{\partial}{\partial z} \left(k \frac{\partial T}{\partial z} \right) + \dot{\Phi} \quad (1)$$

The temperature field of the JB is in a steady state, so $\rho c \frac{\partial T}{\partial \tau} = 0$. The heat source has a steady conduction, and the heat power density is $\dot{\Phi} = 0$. The problem is simplified to 1D heat conduction along the radial direction when the symmetry of the structure is considered. The simplified heat conduction differential equation can be written as follows:

$$\frac{d}{dr} \left(r \frac{dT}{dr} \right) = 0 \quad (2)$$

The analytical solution is as follows:

$$T = \begin{cases} C_1 \ln r + C_3 (r_0 < r < r_{1-}) \\ C_2 \ln r + C_4 (r_{1+} < r < r_2) \end{cases} \quad (3)$$

where C_1 , C_2 , C_3 , and C_4 are all constants.

The boundary conditions are as follows:

$$\Phi = -\lambda_1 2\pi r_1 l \frac{dT}{dr} \Big|_{r=r_{1-}} \quad (4)$$

$$\Phi = -\lambda_2 2\pi r_1 l \frac{dT}{dr} \Big|_{r=r_{1+}} \quad (5)$$

$$T(r_{1-}) - T(r_{1+}) = R_{mi-ju}\Phi \quad (6)$$

$$\Phi = hA[T(r_2) - T_\infty] \quad (7)$$

The constants in Eq. (3) are written as follows:

$$C_1 = \frac{-\Phi}{2\pi\lambda_1 l}, C_2 = \frac{-\Phi}{2\pi\lambda_2 l}, C_3 = \frac{\Phi \ln r_1}{2\pi\lambda_1 l} + \frac{\Phi \ln (r_2/r_1)}{2\pi\lambda_2 l} + \frac{\Phi}{2\pi r_2 l h} + R_{mi-ju}\Phi + T_\infty,$$

$$C_4 = \frac{\Phi \ln r_2}{2\pi\lambda_2 l} + \frac{\Phi}{2\pi r_2 l h} + T_\infty$$

where λ_1 is the heat conductivity coefficient of aluminum, λ_2 is the heat conductivity coefficient of titanium, l is the length of the chassis heat sink, h is the convective heat transfer coefficient between the outside wall of the JB and seawater, T_∞ is the temperature of seawater, and R_{mi-ju} is the contact thermal resistance between the curved base of the chassis heat sink and interior wall of the vessel. The interface that between the curved base and the interior wall of the vessel cannot meet continuous conditions when deformation of the vessel happens in deep sea or influenced by the machining precision of the heat sinks and vessel. Therefore, the contact thermal resistance R_{mi-ju} is introduced. Φ , r_1 , r_2 , λ_1 , l , and T_∞ are all known. Hence, the exact temperature field models of two simplified structures can be established when R_{mi-ju} and h are obtained. The temperature range of the actual structure is also obtained.

Calculation Model for Contact Thermal Resistance R_{mi-ju}

Thermal contact conductance is indispensable for the heat dissipation of the JB. The heat transfer coefficient can be obtained via assembly tests. However, the obtained value will be conservative because surface pattern parameters and contact conditions vary considerably under diverse circumstances. An appropriate and effective established model can predict the contact heat resistance R_{mi-ju} of the JB. The possible minimum contact heat resistance can then be determined by analyzing the model.

The geometric structure of rough surfaces is random, and roughness features are identified at a large number of length scales in accordance with the Gaussian distribution model (Majumdar & Bhushan, 1990). A model is then established by implementing random simulations to analyze roughness features using the Monte Carlo method. A numerical model is developed to obtain the contact thermal resistance on the macroscopic scale according to the calculation of each single thermal resistance on the microscopic scale.

Machined surfaces have asperities that are isotropically and homogeneously distributed (Dyachenko et al., 1963). The surface model can be established under the assumption that the asperities are circular cones with equal apex angles that rest on a base plane (Leung et al., 1998). Two contact surfaces are equivalent to a rough surface and a smooth plane with a rigid contact (Hsieh, 1974). Char-

acteristic parameters of the equivalent rough surface are obtained as follows:

$$\sigma = \sqrt{\sigma_1^2 + \sigma_2^2} \quad (8)$$

$$m = \frac{1}{\frac{1}{m_1} + \frac{1}{m_2}} \quad (9)$$

$$H = \min \{H_1, H_2\} \quad (10)$$

where σ_1 and σ_2 are the roughness values of the two surfaces, m_1 and m_2 are the slopes of the circular cones, and H_1 and H_2 are the hardness values of the two surfaces.

A random number matrix is generated using Monte Carlo method to simulate the peaks of the rough surface distribution. The distances between the peaks and the contact plane under the applied pressure are described as follows:

$$\Delta_i = z_i - d \quad (11)$$

where Δ_i is the distance between the peaks of circular cones and the contact plane, z_i is the summit height of the circular cones measured from the base plane, and d is the distance between the contact plane and the base plane.

Figure 7 shows that Δ_i is only meaningful when it is positive, which implies the contact between the circular cone on the rough surface and the rigid plane. The following parameters are obtained when contact occurs:

$$r_i = \Delta_i/m \quad (12)$$

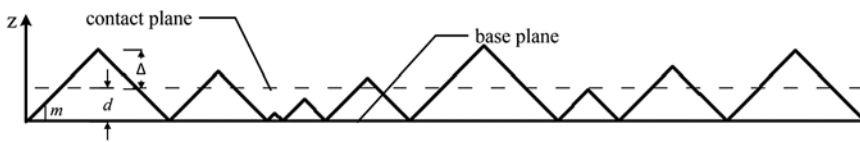
$$a_i = \pi r_i^2 \quad (13)$$

$$f_i = Ha_i \quad (14)$$

where r_i is the radius of the single contact area, a_i is the contact area,

FIGURE 7

Contact between the equivalent rough surface and the base plane.



and f_i is the applied pressure of the single contact area. The distribution of circular cones on the rough surface and characteristic parameters on the contact surface are obtained when the characteristic parameters σ and m of the rough surface are provided.

The contact thermal resistance R_i of each circular cone is obtained with the use of a disk model of a single point contact (Gibson, 1976). Figure 8 shows the disk model of the single point contact.

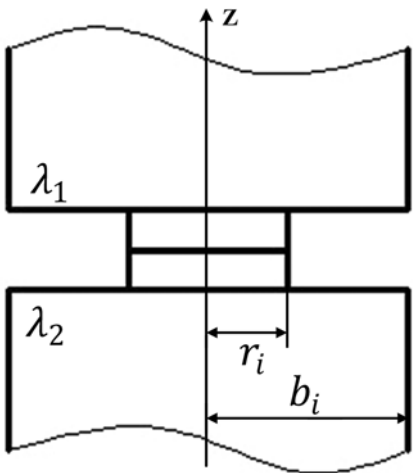
The single contact thermal resistance is obtained as follows:

$$R_i = (1 - r_i/b_i)^{1.5}/4r_i\lambda_s \quad (15)$$

where R_i is the single contact thermal resistance, r_i is the radius of the single contact area, and b_i is the radius of the single heat channel. λ_s is the equivalent

FIGURE 8

Disk model for a single point contact.



thermal conductivity, which satisfies the following equation:

$$1/\lambda_s = 1/\lambda_1 + 1/\lambda_2 \quad (16)$$

where λ_1 and λ_2 are the thermal conductivities of the two surfaces.

The total contact thermal resistance is the sum of the parallel connections of all single point thermal resistances. Therefore, the total contact thermal resistance is obtained as follows:

$$R_{mi-ju} = \frac{1}{\sum_1^N 1/R_i} \quad (17)$$

Figure 9 shows that the prediction of the contact thermal resistance by

the present computation method considerably agrees better with the experimental data than those in the literature (Weilan, 1995). This finding confirms the effectiveness of the method. The curve clusters in Figure 10 shows the relationship between contact thermal resistance and the applied pressure under various circumstances. The materials of the two surfaces are aluminum and titanium, and the parameter σ varies from 0.025 to 50 μm . Surfaces with different surface roughness values are obtained through various machining processes. Differences in surface characteristics are also observed. The specific relationships among surface roughness values, machining processes, and surface characteristics are presented in Table 1. Heat transfer efficiency is also related to the machining tolerance between the interior wall of the vessel and the curved base of the heat sink. Improving machining tolerance can result in better contact and fitting, which will increase heat transfer efficiency.

The effects of the characteristic parameters, applied pressure, and heat

FIGURE 9

Comparison of the computing model with the experimental results.

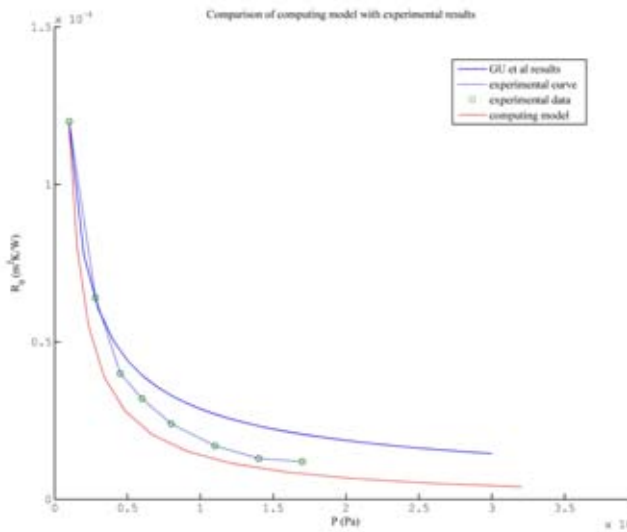
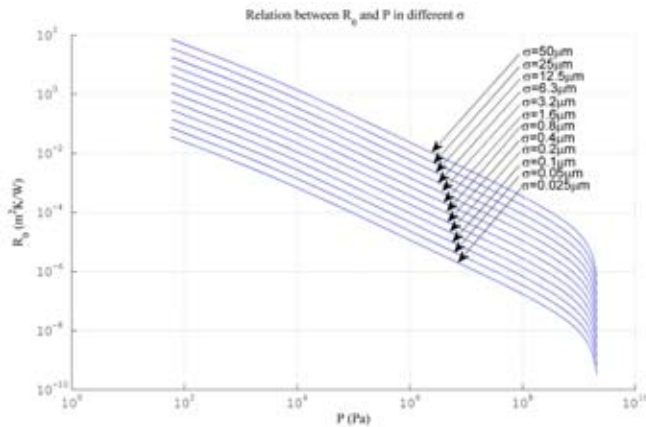


FIGURE 10

Relationship between contact thermal resistance and applied pressure.



conductivity of the rough surfaces on contact thermal resistance are quantitatively analyzed. The method enables the determination of the least possible contact heat resistance in the JB. The contact thermal resistance R_{mi-ju} obtained in real situations of the JB is 6×10^{-3} K/W.

Computation of the Convective Heat Transfer Coefficient h

The flow velocity of seawater in coastal areas in South China Sea is approximately 2 m/s and almost negligible at a water depth of 2,000 m (Yu, 2010). Either forced or natural convection therefore occurs between the exterior wall of the JB and seawater depending on the surrounding environment.

The convection heat transfer coefficient h between the exterior wall and seawater is obtained iteratively. The Grashof number G_r is used as the criterion to determine the heat transfer condition in natural convection and is given as follows:

$$Gr = \frac{g\alpha_v \Delta t l^3}{v^2} \quad (18)$$

where g is the gravitational acceleration, α_v is the expansion coefficient of seawater, Δt is the temperature difference between the exterior wall of the JB and seawater, l is the length of the JB, and v is the viscosity of seawater.

The intensity of the natural convection heat transfer for a horizontal sealed cylinder is determined through

the Nusselt number Nu_m , which is given as follows:

$$Nu_m = C(GrPr)_m^n \quad (19)$$

where C and n are parameters provided by the experiments and Pr is the Prandtl number of seawater.

The convective heat transfer coefficient h is obtained through the Nusselt number Nu_m , as follows:

$$h = Nu \frac{\lambda}{d} \quad (20)$$

Heat power q is given as follows:

$$q' = hA\Delta t = h\pi dL\Delta t \quad (21)$$

The calculated convective heat transfer coefficient h is inaccurate if a large difference between the real heat power q and the calculated heat power q' exists. Then, Δt is modified to recalculate h . This recycled process ends when an appropriate h is obtained.

Finally, we obtain the convective heat transfer coefficient h_1 in natural convection as $383 \text{ W}/(\text{m}^2 \text{ K})$ and the convective heat transfer coefficient h_2 in forced convection as $3874 \text{ W}/(\text{m}^2 \text{ K})$ when the flow velocity of seawater is 2 m/s. The corresponding convective heat transfer coefficient is between h_1

TABLE 1

Relationships between surface roughness values and various machining processes.

Surface Roughness Values	Machining Processes	Surface Characteristics
$\sigma = 50, 25$	rough turning, rough planning, rough milling, etc.	obvious tool mark
$\sigma = 12.5, 6.3, 3.2$	finish turning, finish milling, rolling, etc.	tool mark is faintly visible
$\sigma = 1.6, 0.8, 0.4$	finish grinding, end milling, etc.	processing traces is invisible, processing direction is faintly recognizable
$\sigma = 0.2, 0.1$	supergrinding, polishing, etc.	dim glossy surface
$\sigma = 0.05, 0.025$	superfinish	bright or mirror glossy surface

and b_2 when the seawater flow condition is between the two cases.

Software Simulation Analysis

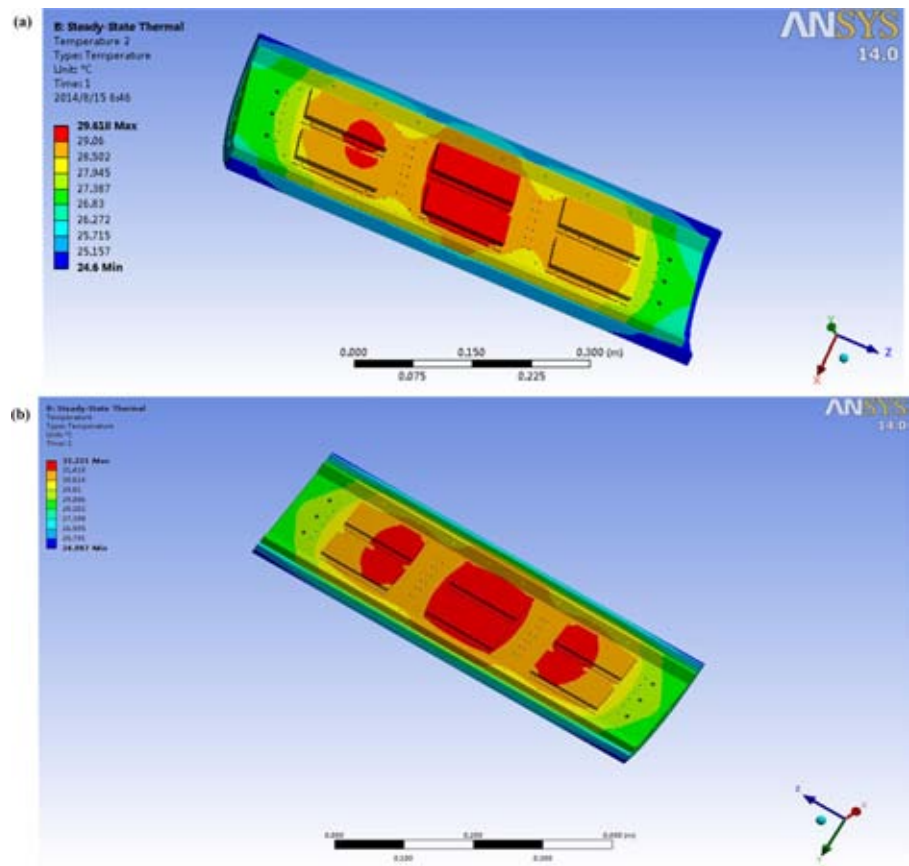
The models of parameters $R_{mi\text{-}ju}$ and h have been previously established, so all parameters needed in the model of the temperature range of the JB are obtained. The temperature fields of the JB under different seawater flow rates are established according to the temperature range model of the actual structure of the JB. The length, external diameter, inner diameter, and wall thickness of the vessel are 876, 310, 278, and 16 mm, respectively. The total heat generated inside the vessel is 1,188 W.

Finite element models of the temperature field in the JB were built in the following extreme cases to verify model accuracy: (1) seawater was almost still, and heat convection between the exterior wall of the JB and seawater was purely natural convection; and (2) the velocity of seawater was 2 m/s, which is the maximum flow rate in the South China Sea. The 3D model for the JB was established using ANSYS software. Vessel deformation caused by external water pressure could reduce heat transfer efficiency; hence, pressure load was added in the software simulation by an equivalent way. Finally, heat sources, boundary conditions, contact types, and physical property parameters were set to calculate the temperature field based on a practical situation. Figure 11 shows the contours of the temperature distribution of the vessel in different environments: Figure 11(a) is simulated at 1 atm, and Figure 11(b) is simulated under 20 MPa pressure.

The models for the temperature range of the JB are established when the convection heat transfer coefficient

FIGURE 11

Contours of temperature distribution in the JB.



is equal to b_1 or b_2 . The curves in Figure 12 show the relationship between the temperature model and the simulation results of the JB. In Figures 12(a) and 12(b), the JB is under 1 atm, and $h = b_1$ and $h = b_2$, respectively. In Figures 12(c) and 12(d), the JB is under a pressure of 20 MPa, and $h = b_1$ and $h = b_2$, respectively.

Figure 12 shows that the simulated temperature is within a narrow range defined by the two temperature models. A sudden change in temperature is observed in all the figures. The existence of contact thermal resistance $R_{mi\text{-}ju}$ causes discontinuity in temperature distribution. The following conclusions are drawn after comparing the figures: the internal temperature of the vessel and the contact thermal resistance be-

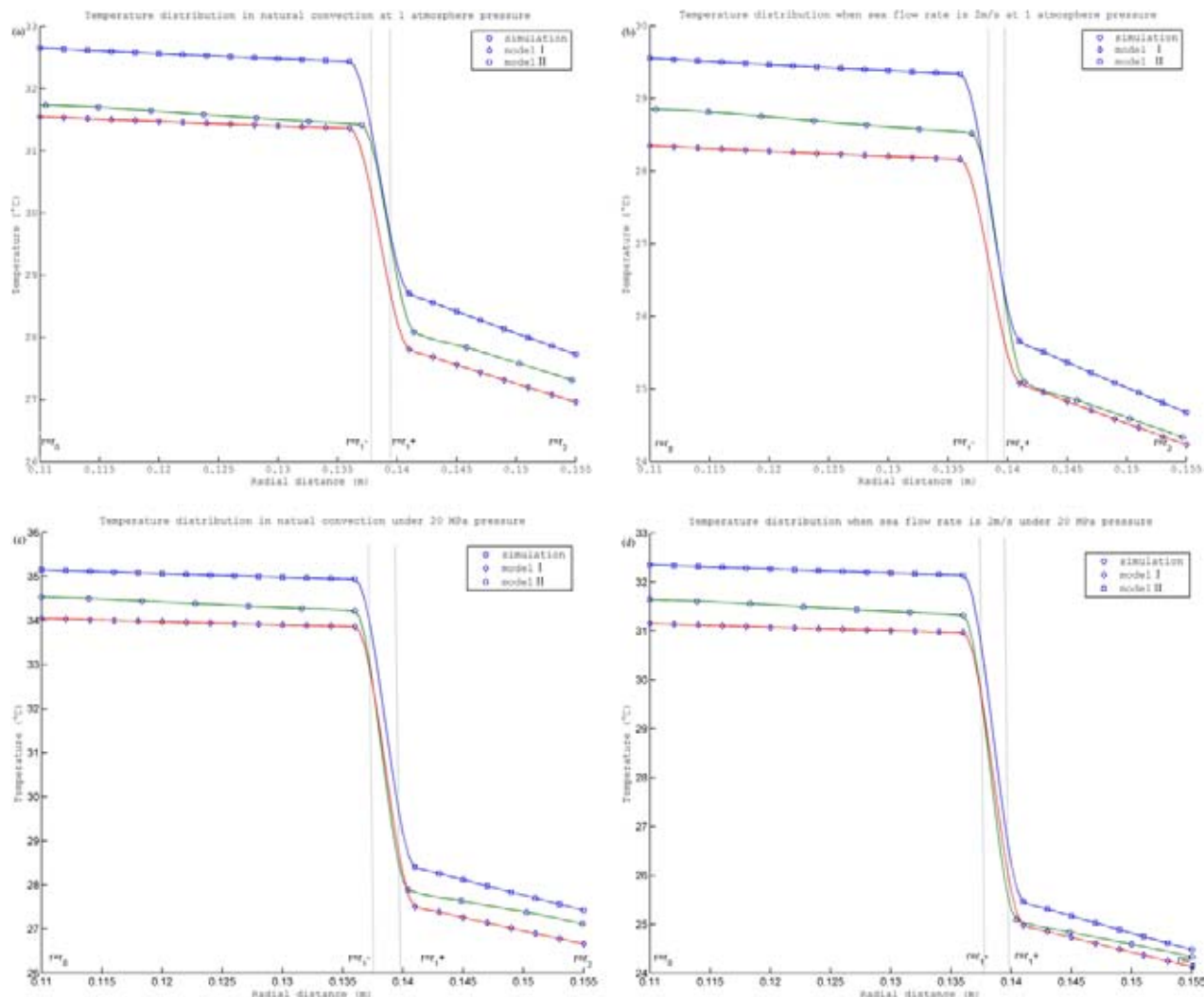
tween heat sink curved bases and the interior cylinder wall increase, the heat transfer efficiency of the system is reduced, and the cooling performance deteriorates when the vessel is deformed by external water pressure under the situation in which the convective heat transfer coefficient h is the same value. Thus, contact thermal resistance is essential, particularly when good heat dissipation performance is required. Therefore, the effect of contact thermal resistance should be considered in designing the JB and should be reduced to improve the heat dissipation effect.

Experimental Results

A series of laboratory experiments was conducted in a water tank and a

FIGURE 12

Temperature inside the JB at different radial distances: (a) $h = h_1$ at 1 atm; (b) $h = h_2$ at 1 atm; (c) $h = h_1$ under 20 MPa pressure; (d) $h = h_2$ under 20 MPa pressure.



sealed pressure case to verify the theoretical model for the temperature field and validate the heat dissipation performance of the JB. The JB and the related instruments were placed in a water tank and a sealed pressure case filled with simulated seawater, respectively, as shown in Figure 13. Six temperature sensors were installed to monitor the temperature at different positions in the JB. Temperature was obtained through the data acquisition module of the lower computer in real time and transmitted by Ethernet to an upper

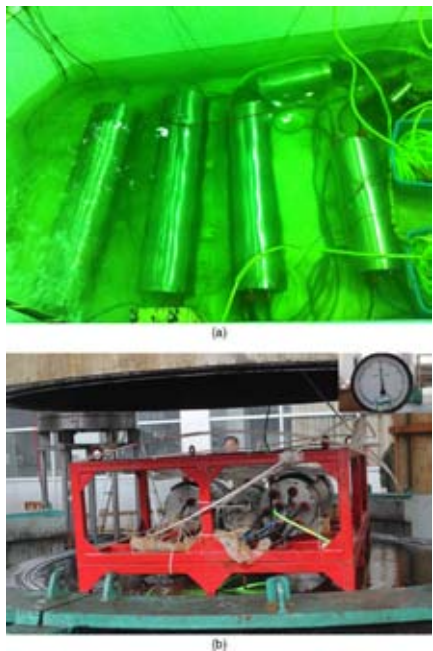
computer. The computer communication interface and monitoring software shown as Figure 14 was designed to monitor data changes, display historical curves, and control the switches of the multichannel power output.

The temperature of the simulated seawater was 24°C during the course of the experiments, and its velocity was 0 m/s. Therefore, natural convection heat transfer was observed between the exterior wall of the JB and the simulated seawater. The power consumption of the external loads

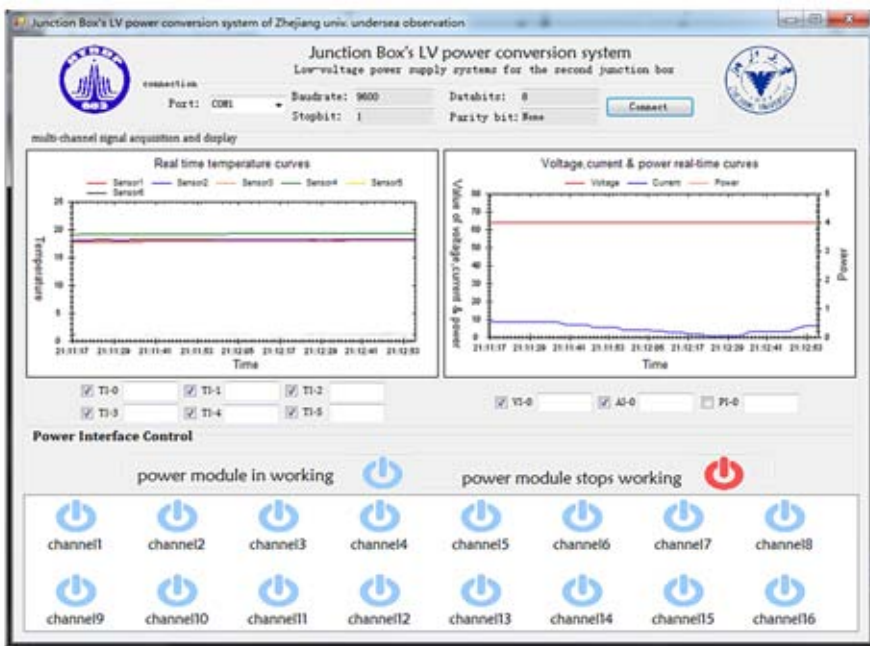
reached the maximum capacity that could be supplied by the power channels. The temperature monitored inside the JB gradually increased as the JB started working and eventually stabilized after approximately 2 h. In the water tank test, the heat source temperature remained at 33.4°C, which was assumed as the highest temperature inside the JB. The temperature of the outside surface of the heat sink remained at 32.1°C, whereas the temperature of the interior wall of the JB remained at 29.6°C. In the sealed

FIGURE 13

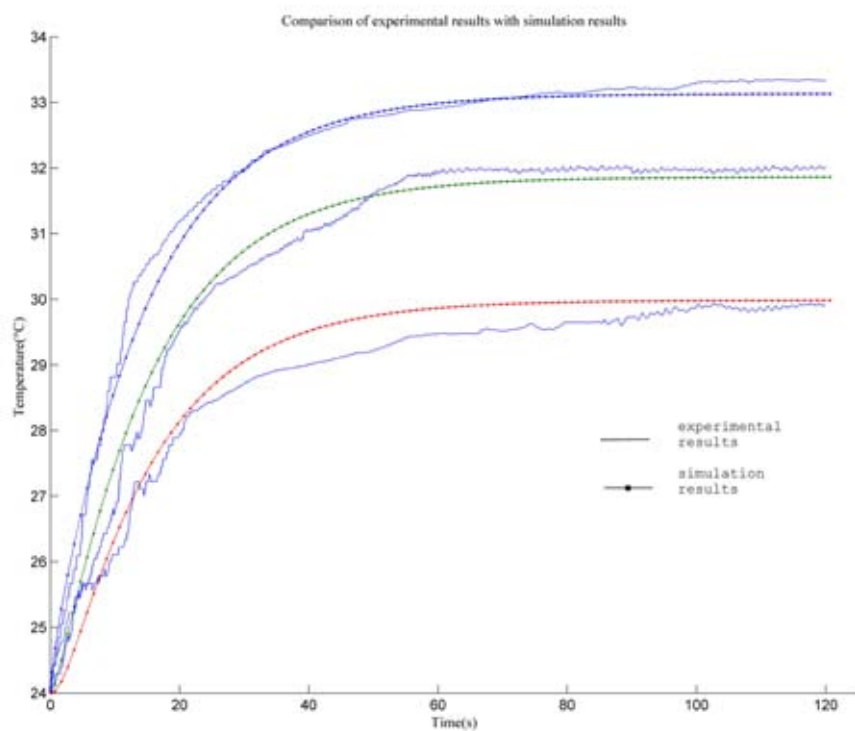
(a) Experiments in a water tank. (b) Experiments in a sealed pressure case.

**FIGURE 14**

Human machine interface of the JB.

**FIGURE 15**

Comparison of the experimental and simulated results at 1 atm.



pressure case test, the corresponding temperatures in the aforementioned positions are 34.8°C, 33.4°C, and 30.8°C. Figure 15 depicts the comparisons of the time series of the temperature data obtained from the experiments and the dynamic simulation results from ANSYS in three different positions at 1 atm during the experiments and the simulations. The experimental results agree well with the simulated results in each position when the external pressure of the vessel is 1 atm. However, the experimental temperatures are slightly higher than the simulated values when a water pressure of 20 MPa is loaded onto the outside surfaces of the JB. We believe that the effects of the internal radiation and convection of the vessel, which are disregarded in the software simulation but actually exist during the tests, reduce the actual temperature.

Superiority of the structure is verified by experimental results, simulation

results, and theoretical model analysis. The heat dissipation structure demonstrates good performance. The temperature increases by 10°C when the JB is fully loaded and exhibits a natural convection heat transfer with seawater. However, the temperature increase by 7°C when the JB is fully loaded and exhibits a forced convection heat transfer with seawater in which the seawater velocity is 2 m/s. The good agreement among the temperature field model, simulated results, and experimental data indicates the accuracy of the theoretical model and simulation analysis.

The electronic components and instruments are highly reliable in cool environments, so the reliability of the entire system of the JB is guaranteed. Seawater flow velocity varies between stationary to 2 m/s considering the changes in sea conditions. Convection heat transfer coefficient can exhibit the

corresponding changes between h_1 and h_2 . The theoretical model and simulation results in Figure 16 show that the maximum temperature of the JB in different sea conditions is obtained.

Conclusion

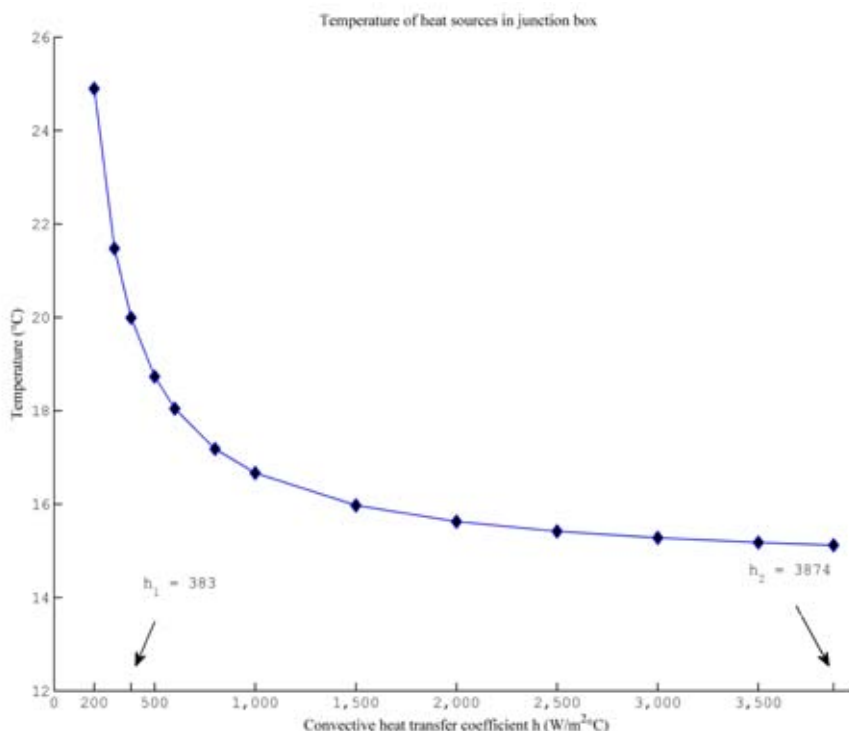
The heat dissipation mechanism of the JB is established by analyzing its thermal resistance network according to current studies on cooling methods for submarine equipment and the structures of OBSEA and NEPTUNE JB. The internal structure inside the JB consisting of circumferentially equi-spaced chassis heat sinks and an adaptive elastic support structure is designed. The structure demonstrates excellent heat dissipation performance.

The discontinuous model of the temperature range of the JB is established. The model comprehensively

considers the deep-sea ambient pressure, machining precision of the workpieces, flow rate of seawater, and thermal contact resistances between the curved base of the heat sinks and the interior wall of the JB. Structural parameters are analyzed to evaluate their effects on heat dissipation in the JB and optimize the structure. 3D dynamic simulations of heat dissipation were conducted to describe the temperature field in the JB under different ambient pressures. Water tank tests and sealed pressure case tests of the JB connected to the laboratory setup of the Experimental Underwater Observatory Network System of China were run continuously for 120 and 24 h, respectively. Experimental data curves are consistent with the computed results of the theoretical model and simulated results. The maximum temperature increase inside the JB is between 7°C and 10°C based on the different sea conditions in South China Sea. The findings also validate the excellent heat dissipation performance in the JB. We believe that the structure designed in the present work is reasonable and has high thermal reliability. This work proposes a design to guarantee long-term reliable operation of a cabled ocean observatory network.

FIGURE 16

Maximum temperature of heat sources in the JB at different sea conditions.



Acknowledgments

This work was supported by The National High Technology Research and Development Program of China (Grants 2012AA09A402 and 2012AA09A408) and was supported by the National Natural Science Foundation of China under Grant 51409229, by the Science Fund for Creative Research Groups of the National Natural Science Foundation of China under Grant 51221004, and by the Zhejiang Provincial Natural Science Foundation of China under Grant LQ14E070002.

Corresponding Author:

Canjun Yang

State Key Laboratory of Fluid Power and Mechatronic Systems, Zhejiang University Hangzhou 310027, China
Email: ycj@zju.edu.cn

References

- Aguazzi**, J., M  nuel, A., Condal, F., Guillen, F., Nogueras, M., del Rio, J., ... Palanques, A. 2011. The new seafloor observatory (OBSEA) for remote and long-term coastal ecosystem monitoring. *Sensors.* 11(6):5850-72. <http://dx.doi.org/10.3390/s110605850>.
- Barnes**, C.R., & Tunnicliffe, V. 2008. Building the World's First Multi-node Cabled Ocean Observatories (NEPTUNE Canada and VENUS, Canada): Science, Realities, Challenges and Opportunities. In: Proceedings of MTS/IEEE Kobe Techno-Ocean, Oceans 2008. pp.1213-20. Kobe: IEEE.
- Chave**, A.D., Waterworth, G., Maffei, A.R., & Massion, G. 2004. Cabled ocean observatory systems. *Mar Technol Soc J.* 38(2):30-43. <http://dx.doi.org/10.4031/002533204787522785>.
- Chen**, Y.H., Yang, C.J., Li, D.J., & Jin, B. 2012. Design and application of a junction box for cabled ocean observatories. *Mar Technol Soc J.* 46(3):50-63. <http://dx.doi.org/10.4031/MTSJ.46.3.4>.
- del R  o**, J., Aguzzi, J., Costa, C., Menesatti, P., Sbragaglia, V., Nogueras, M., ... Manuel, A. 2013. A new colorimetrically-calibrated automated video-imaging protocol for day-night fish counting at the OBSEA coastal cabled observatory. *Sensors.* 13(11): 14740-53. <http://dx.doi.org/10.3390/s131114740>.
- Dyachenko**, P.E., Tolkacheva, N.N., Andreev, G.A., & Karpova, T.M. 1963. The Actual Contact Area between Touching Surface. Moscow: Acad Sca. Press.
- Favali**, P., Beranzoli, L., & Santis, A.D. 2015. Seafloor Observatories: A new vision of the Earth from the Abyss. UK: Chichester. 669 pp.
- Gibson**, R.D. 1976. The contact resistance for a semi-infinite cylinder in a vacuum. *Appl Energ.* 2(1):57-65. [http://dx.doi.org/10.1016/0306-2619\(76\)90039-8](http://dx.doi.org/10.1016/0306-2619(76)90039-8).
- Howe**, B.M., Chan, T., Sharkawi, M.E., Kenney, M., Kolve, S., Liu, C.C., ... Siani, C. 2006. Power System for the MARS Ocean Cabled Observatory. Available from http://www.interactiveoceans.washington.edu/file-s/howe_mars_power_ssc06.pdf.
- Hsieh**, C.K. 1974. A Critical Evaluation of Surface Geometrical Parameters for a Nominally Flat Surface Model. *J Tribol.* 96(4):638-9. <http://dx.doi.org/10.1115/1.3452512>.
- Kawaguchi**, K., Kaneda, Y., & Araki, E. 2008. The DONET: A real-time seafloor research infrastructure for the precise earthquake and tsunami monitoring. In: Proceedings of Oceans 2008. pp. 1-4. Kobe: IEEE. <http://dx.doi.org/10.1109/oceanskobe.2008.4530918>.
- Kays**, W.M., Crawford, M.E., & Weigand, B. 2012. Convective heat and mass transfer, 4th ed. New York: Tata McGraw-Hill Education. 576 pp.
- Leung**, M., Hsieh, C.K., & Goswami, D.Y. 1998. Prediction of thermal contact conductance in vacuum by statistical mechanics. *J Heat Trans.* 120(1):51-7. <http://dx.doi.org/10.1115/1.2830064>.
- Majumdar**, A., & Bhushan, B. 1990. Role of fractal geometry in roughness characterization and contact mechanics of surfaces. *J Tribol.* 112(2):205-16. <http://dx.doi.org/10.1115/1.2920243>.
- McDonald**, G., & Naiman, M. 2002. Heat-transfer advances for submerged oceanographic systems. In: Proceedings of Oceans 2002. pp. 2045-9. Mississippi: IEEE. <http://dx.doi.org/10.1109/oceans.2002.1191946>.
- Petitt**, R.A., Jr., Bowen, A., Elder, R., Howland, J., & Naiman, M. 2004. Power system for the new Jason ROV. In: Proceedings of Oceans 2004. pp. 1727-31. Kobe: IEEE. <http://dx.doi.org/10.1109/oceans.2004.1406385>.
- Priede**, I.G., Solan, M., Mienert, J., Person, R., Weering, T., Pfannkuche, O., ... Klages, M. 2004. ESONET-European Sea Floor Obser-
- vatory Network. In: Proceedings of Oceans 2004. pp. 2155-63. Kobe: IEEE. <http://dx.doi.org/10.1109/oceans.2004.1406479>.
- Weilan**, G. 1995. A Method for Calculation of Contact Heat Resistance between Two Contacting Surfaces. *J Aerospace Power.* 3:233-6.
- Woodroffe**, A.M., Pridie, S.W., & Druce, G. 2008. The NEPTUNE Canada Junction Box-Interfacing science instruments to sub-sea cabled observatories. In: Proceedings of Oceans 2008. pp. 1-5. Kobe: IEEE. <http://dx.doi.org/10.1109/oceanskobe.2008.4531021>.
- Yu**, X.H. 2010. The Research and Implementation of Heat Dissipation System for Seafloor Junction Box. Master thesis, Zhejiang University. 59 pp.

Study of a Novel Underwater Cable With Whole Cable Monitoring

AUTHORS

Jiawang Chen
Chunying Xu
Ying Chen
Ocean College, Zhejiang University

Jian Ji
Institute of Zhejiang Marine Development Research

Dongxu Yan
Ocean College, Zhejiang University

Introduction

Underwater cable connections are key pieces of equipment in topside and subsea facilities for electro-hydraulic control channel underwater production units, which provide underwater communications, power, and pulling forces to marine equipment, marine drag systems, and mooring systems (Szyrowski et al., 2013a, 2013b). However, underwater cables must operate under rough marine conditions, and at the seafloor, they are exposed to flow scouring, making them apt to bend or warp, which could result in underwater device failure. Moreover, excessive bending, or even breakage, presents a hazard for rescuing personnel and environmental damage. A succession of cable damaging events that disrupted system performance can be noted in Talling et al. (2013) and Carter et al. (2014, 2012). As a result of the multiple functions that cables must serve, in addition to the dynamic underwater environment in which they are installed and operated, their stability and reliability for underwater systems are of utmost importance.

ABSTRACT

This paper describes a novel concept for detecting and tracking underwater cables that differs from common detection methods, including visual, acoustic and magnetic detection, which are based on a survey platform, such as remotely operated vehicles and autonomous underwater vehicles, and have high costs and require long-time monitoring. The proposed detection method can be performed in locations that are difficult to observe using cameras without the use of magnetic fields. The concept relies on low-cost flex sensors that provide underwater, real-time, whole cable detection. Building off of this concept, a detection system and an error analysis system were incorporated, which includes the characteristics of the flex sensors, the mounting structure for the flex sensors, and the underwater cable as well as the 2-D cable bend model and a water tank test. The detected data set, which was rendered on an observation monitor, provided visual feedback regarding any bending or warping problems. To evaluate the detection accuracy, mean absolute error and similarity analyses were performed using the observational data and sensor data obtained from the water tank test. The results of these analyses showed strong agreement between the fitted curve to the detected data and the observational curve, indicating acceptable error. These results demonstrate the feasibility of the proposed system for effective underwater cable detection. Thus, the results of this investigation clearly reveal the potential of the novel sensing technique for practical underwater cable detection and monitoring applications. However, the 2-D cable bending detection model is not suitable for 3-D bending or torsion, which will be considered in future research.

Keywords: underwater cable detection, 2-D cable bend model, flex sensor

A common method to reduce the risk of failure is frequent detection and preventative maintenance. There are three main common methods of underwater power and telecommunication cable detection and tracking: visual tracking, acoustic detection, and magnetic detection (Szyrowski et al., 2013a, 2013b; El-Fakdi & Carreras, 2013).

Common visual-based systems for underwater cable detection on survey platforms typically rely on remotely operated vehicles (ROVs) or autonomous underwater vehicles (AUVs) equipped with mounted video cameras

(Kuhn et al., 2013; Ortiz et al., 2011; Jordán et al., 2011; Ortiz & Antich, 2014; Lee et al., 2012; Sakagami et al., 2013). The vision detection process includes cable location search and tracking. Cable search is the early work of underwater cable detection that is performed to find the cable position. Cable tracking is the process of moving along the cable while performing the necessary measurements (Bagnitsky et al., 2011).

Underwater visual detection has a critical limitation: in most cases, there is little or no ambient light, resulting

in poor visibility. To solve this limitation, light sources are required to illuminate the underwater cable. However, images of underwater objects illuminated by a light source contain blurring from the spatial attenuation of higher frequencies and backscatter from the more predominant lower frequencies (Szyrowski et al., 2013a). Ortiz et al. (2011) identified underwater image characteristics, including blurring, low contrast, nonuniform illumination and instability caused by the motion of the vehicle, thereby increasing the complexity of detection. The clarity of images directly affects detection judgment because detection is based on distinguishing the cable from the surrounding environment. Moreover, when a cable has rested on the seabed for a long period of time, detection is increasingly difficult due to the rocks and sediment that cover it. Wirth et al. (2008) and Ortiz et al. (2011) adopted a probabilistic approach based on particle filters which handle the ambiguities, and they concluded that the approach is suitable for online cable detection.

Inzartsev & Pavlin (2008) noted that visual detection alone was not sufficient for underwater cable detection because video imaging does not provide consistently reliable data for cable recognition.

Acoustic methods are able to penetrate the seabed, enabling the detection of buried utilities (Szyrowski et al., 2013a). Zhou et al. (2015) showed how sonar detection is based on the reflected sonar signal of a submarine cable, which includes a sonar shallow profile. Capus et al. (2010) measured the impact of different seabed types on the cable detection ability and concluded that the rougher the sediment, the higher the reverberation level. The grazing angle (which is the angle at

which a sonar pulse meets and moves across the seabed) plays a critical role in determining the reverberation noise level. For rough sediments, a lower grazing angle provides better results, and vice versa. Brown et al. (2011) concluded that detection was also affected by the cable curvature, tank wall returns, ambient noise sources, and disturbances in the sediment surface from an experiment in a water tank.

Improving postdetection filtering and noise suppression are useful methods to minimize these issues (Capus et al., 2010). Mandhouj et al. (2012) noted that most methods reducing the noise apply different filtering and are often classified in two categories: methods acting in the spatial domain and those acting in the transformed domain. Isaacs and Goroshin (2010) noted that the classical approach to cable detection in sonar imagery is low-pass filtering, followed by edge detection and the application of the Hough transform. In addition, Villar et al. (2014) indicated that the efficiency of online image processing from acoustic data is also a key issue for acoustic. These data should be processed in an efficient time so that the detection system is able to detect and recognize a predefined target.

Acoustic detection cannot be used for underwater cables in shallow water, especially those in coastal regions. Interfacing reverberations from the air/sea and sea/bottom interfaces and complex seafloor topographical profiles present a difficult acoustic environment. Moreover, man-made refuse or structures in coastal regions may cause a high false alarm rate when using the acoustic sensor alone (Pei et al., 2010).

Magnetic detection is an effective method for underwater buried target detection and can augment acoustic

means of detection, effectively reducing the number of false alarms (Pei et al., 2010). Wang et al. (2011) described cable detection using magnetic field technology that was based on two basic principles: an electric current can produce a magnetic field (electromagnetism) and a changing magnetic field within a coil of wire induces a voltage across the ends of the coil (electromagnetic induction). Induction coils are based on Faraday's induction law. Szyrowski et al. (2013b) noted that two types of approaches could be found in practical applications of magnetic detection. The first method is the active magnetic detection method, which relies on a submarine cable conductor operating at a specific AC signal, allowing for the detection of the parameters of the surrounding electromagnetic signals. This method often requires onshore access to the cable, and the attenuation is large and is thus not suitable for long-distance submarine cable detection (Zhou et al., 2009). The second method employs passive magnetic detection, which relies on the physical magnetic properties of the submarine cable, does not require the signal of the submarine cable to be strengthened, and is suitable for the detection of complex waters (Zhou et al., 2015).

Underwater cable projects often use a variety of detection equipment and technologies. Data from visual, acoustic, and magnetic sensors are often processed together. However, all of the methods described herein are based on survey devices, such as ROVs or AUVs, which are high cost and cannot detect the whole cable in real time (El-Fakdi & Carreras, 2013). The limitations demonstrate that there is still a great need for a method that can detect underwater cables with real time and low cost.

To address this need, this paper describes a novel method of using flex sensors to measure the bending angles of underwater cables that prevent accidents caused by cable bending, warping, or breaking at a lower cost than most state-of-the-art methods.

To detect the bend state, different sensors have been investigated: a conductive ink-based flex sensor, a novel skin curvature sensor (Kanisus et al., 2004), an elastomer film embedded with a micro-channel of a conductive liquid (Majidi et al., 2011), strain sensors (Lorusso et al., 2005), and capacitive or magnetic devices (Fahn & Sun, 2010). In this study, the conductive ink-based flex sensors (Spectra Symbol Inc.) are adopted because they are flexible, light-weight, and extremely low-cost sensors that can be applied to measure the bend state of objects and have been used for data gloves, medical devices, and so on (Saggio et al., 2009a, 2009b; Saggio, 2014).

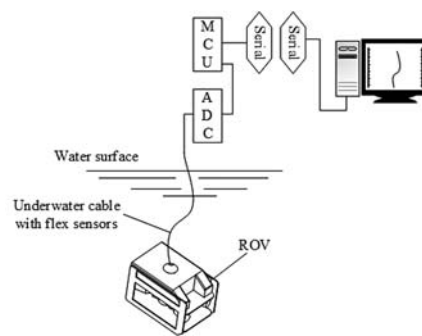
The rest of this paper is organized as follows. First, the concept of underwater cable detection based on flex sensors is proposed. Second, the characteristics of flex sensors are discussed. Third, on the basis of the flex sensors, the mounting structure between flex sensors and underwater cables is presented. Fourth, a 2-D visual bending model is established to provide guidelines for the system performance. Last, a water tank experiment with error analysis is performed to demonstrate the feasibility of the approach.

A Novel Concept for Underwater Cable Detection

The detection system is illustrated in Figure 1 and uses an ROV's umbilical cable as an example. Flex sensors (Spectra Symbol Inc.) were arranged

FIGURE 1

System diagram: detection system using an ROV's umbilical cable as an example.



to sense the underwater flexible cable bend angles. Data acquired from the sensors are conditioned and sent to a computer via a serial port controlled by MCU (stm32), which has three 12-Bit ADCs, 112 fast I/O ports, and provides an interface to the computer. The MCU reads all of the sensor angles at a rate of 100 Hz and communicates with the computer via a RS-232C serial interface at speeds of 9,600 baud. The resulting signals were used to build a 2-D computer bend model including position and bend. The real-time image displays the deformation of the underwater cable, providing the underwater cable working state, and gives the user a visual feedback.

Characteristics of the Flex Sensors

This paper adopted the light-weight and flexible 4.5-inch Spectra Symbol Flex sensors, as shown in Figure 2.

FIGURE 2

Spectra Symbol Flex sensor: length: 4.5 inches, height: ≤ 0.43 mm (0.017 inch), life cycle: > 1 million.



The flex sensor is a unipolar device, that is, the resistance increases as the flex angle increases in one direction and decreases or is unchanged when bent in the other direction.

To obtain the characteristics of the flex sensors, a proper measurement setup was made (Figure 3). The flex sensor was attached to the hinge wings, which mounted on the stepper motor axis. One wing of the hinge was fixed to the central axis. The other one rotated with the motor. The bending angle was controlled by the motor, and the resistive response of the sensor was read by a digital multimeter.

The sensor was moved from 0° to 90° by increments of 10°. The relationship between the bend angle and the resistance of the flex sensor is shown in Figure 4.

Figure 4 shows that the relationship between resistance and bend angle of the flex sensor has a nearly linear behavior only after approximately 30° and some degree of nonlinearity between 0 and 30°. According to the characteristics of the flex sensor, the sampling circuit of each flex sensor can be seen in Figure 5.

The output signal V_{out} according to Eq. 1:

$$V_{out} = \frac{V_{cc} * R}{R_f + R} \quad (1)$$

wherein R is the resistance value of flex sensor and R_f is the reference resistance that the value is constant. According to Saggio (2014), in order to assure output

FIGURE 3

Diagram of measurement setup for the sensor's characterization.

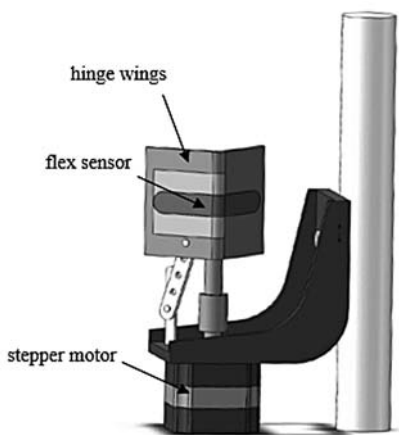


FIGURE 4

The characterization of a flex sensor: resistance vs. bending angle.

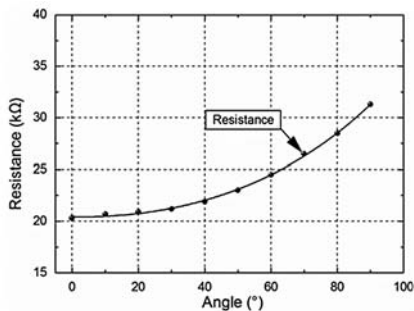
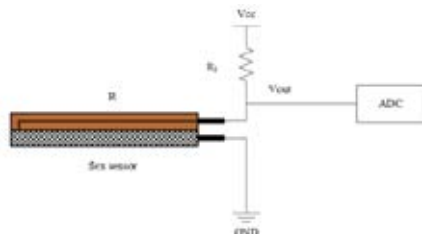


FIGURE 5

The sampling circuit of flex sensor.



signal V_{out} with the largest dynamic, the value of R_f could be obtained by Eq.2:

$$R_f = \sqrt{R_{max} * R_{min}} \quad (2)$$

wherein R_{max} and R_{min} are provided by the flex sensor under maximum and flat, respectively.

According to the sampling circuit, the relationship between the bend angle and computer sampling value can be obtained, as shown in Figure 6. Based on the relationship, the computer gets the AD sampling value from the sampling circuit and converts it to a bend angle.

Flex Sensors and Underwater Cable Mounting Structure

To sense shape effectively, several flex sensors should be employed. In this paper, an experimental underwater cable was divided into five equal segments. Each segment had two flex sensors placed along the axial symmetric to provide bidirectional bend detection because the flex sensors are unipolar, that is, one flex sensor had a negative response with respect to the other (Figure 7). One end of each sensor is fixed on the tube, while the other end can slide freely along the

tube (longitudinal direction) when the underwater cable bends, but movement in any other direction was restricted.

2-D Bend Model of an Underwater Cable

The bend angles of each underwater cable segment were obtained from flex sensor data. The length of each underwater cable segment is short, allowing it to be modeled as a circular arc without twist. In particular, the length of each cable segment is equal to the sensor length, such that the bend angle of the sensor represents the cable segment bend angle. The flex sensors were numbered according to the position along the underwater flexible cable for building model, as shown in Figure 7. For example, sensor #12 represents the second flex sensor of the first cable segment.

The underwater cable bend direction must be determined for each cable segment. Because the flex sensors were defined relative to a 0 degree

FIGURE 6

The relationship between the bend angle and sampling value.

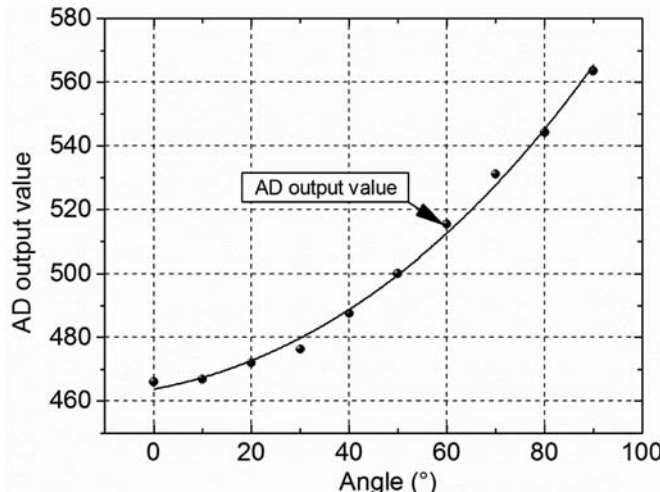
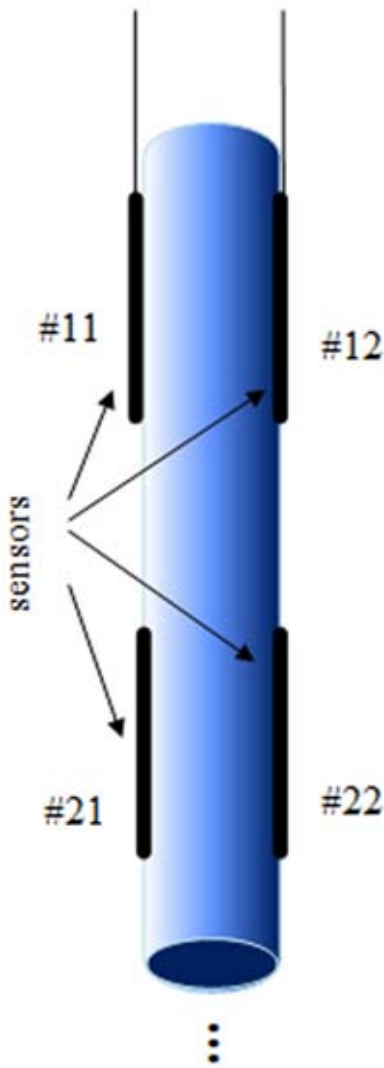


FIGURE 7

The flex sensors and underwater flexible cable mounting structure.



bend, the resistance increases (positive) as the flex angle increases in the calibrated direction (an inward bend in Figure 2) and is negative or unchanged when bent in the opposite direction. If the signs of both sensors in the same segment are opposite, then the positive sign of sensor data is regarded as the bend direction of the cable. Otherwise the sensor data are regarded as invalid.

Assuming that the underwater flexible cable was divided into n segments, each with an equal arc length s , from

the arc length formula, each segment arc radius (R_1, R_2, \dots, R_n) can be determined. Figure 8 shows the diagram of the cable shape reconstruction for 2-D bends.

The first segment start point l_1 is known and fixed. Assuming that the direction of the first segment arc radius is the same as the direction of unit vector t , the center of first arc O_1 is:

$$\begin{bmatrix} O_{1,x} \\ O_{1,y} \end{bmatrix} = \begin{bmatrix} l_{1,x} \\ l_{1,y} \end{bmatrix} \pm R_1 \cdot t \quad (3)$$

where '+' corresponds to a concave arc and '-' corresponds to a convex arc.

When the arc segment is concave, the first segment end point is obtained by

$$\begin{bmatrix} l_{i+1,x} \\ l_{i+1,y} \end{bmatrix} = \begin{bmatrix} O_{i,x} \\ O_{i,y} \end{bmatrix} + R_i \begin{bmatrix} \cos(\theta_i + W) \\ \sin(\theta_i + W) \end{bmatrix} \\ = \begin{bmatrix} O_{i,x} \\ O_{i,y} \end{bmatrix} + \frac{s}{\theta_i} \begin{bmatrix} \cos(\theta_i + W) \\ \sin(\theta_i + W) \end{bmatrix} \quad (4)$$

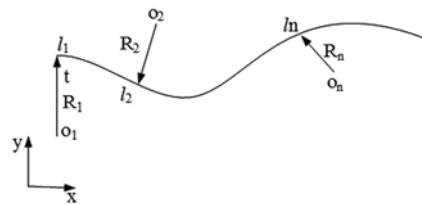
wherein w is determined by

$$w = \sum_{j=1}^{i-1} \theta_j \quad (5)$$

where θ_j is positive for a convex arc and negative for a concave arc.

FIGURE 8

Diagram of the cable shape reconstruction for 2-D bends: O_1, O_2, \dots, O_n are the centers of each cable segment; l_1, l_2, \dots, l_n represent the start point of cable segment; R_1, R_2, \dots, R_n are the radii; and t is the radius unit vector of the first segment.



The arc center is obtained according to the tangent slope and is equal between the segments junction:

$$\begin{bmatrix} O_{i,x} \\ O_{i,y} \end{bmatrix} = \begin{bmatrix} l_{i,x} \\ l_{i,y} \end{bmatrix} \pm \frac{R_i}{R_{i-1}} \begin{bmatrix} l_{i,x} - O_{i-1,x} \\ l_{i,y} - O_{i-1,y} \end{bmatrix} \quad (6)$$

When the concavity or convexity of $i-1$ is the same as that of the i segment, Eq. 6 is '-' and is otherwise '+'.

Via Eq. 3 through Eq. 6, the 2-D bend shape of the underwater cable is determined.

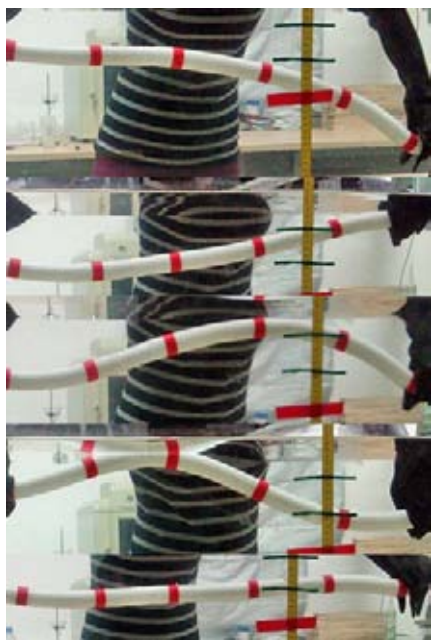
Water Tank Test and Errors Analysis

To evaluate the detection system proposed in this paper, a series of tests were performed in a tank measuring $1.5 \text{ m} \times 80 \text{ cm} \times 40 \text{ cm}$. The tank was equipped with a tape rule for unified coordinate systems of physical rubber and model curve. The cable was constructed from crylonitrile-butadiene rubber that was 25 cm in diameter and 65 cm in length. The rubber was divided into five segments; each segment had two flex sensors, as shown previously. The lengths of the cable segment and flex sensor were equal, such that the sensor bend angles represented the rubber segment bend, as previously discussed. The rubber with flex sensors was waterproof and enclosed in bellows for use in underwater environments. In this paper, five different bend positions were tested (Figure 9).

The differences between two curves consist of degree of similarity and magnitude of the errors. So a similarity comparison and mean absolute error were used for evaluating the differences between fitted curves to the detected data and the observational curves in this study. The similarity calculation made use of the cosine value

FIGURE 9

Five bend states of rubber in the tank.



of the vector angle model (Eq. 7), as it reflected the directional differences between two curves.

$$\text{sim}(X, Y) = \frac{\sum_{i=1}^n X_i Y_i}{\sqrt{\sum_{i=1}^n X_i^2} \sqrt{\sum_{i=1}^n Y_i^2}} \quad (7)$$

$\text{sim}(X, Y)$ is the similarity and X and Y represent two images: curves from the observed image and detected data, respectively. The mean absolute error was calculated according to Eq. 8. The mean absolute error does not exhibit the offset of the positive and negative values, better reflecting the errors. The same number of data points from the observational curves and the detected data was calculated.

$$\text{ava_error}(X, Y) = \frac{\sum_{i=1}^n |X_i - Y_i|}{n} \quad (8)$$

where n is the experimental number (505 in this study). The data of the

fitted curve of the observed image and the detected data must be normalized before calculation. Figure 9 shows the comparison between the measured data and the fitted curve of the physical picture.

The mean absolute error and similarity values between the detected data and the fitted curve of rubber are shown in Table 1.

From Figure 10 and Table 1, strong agreement is demonstrated between the detected data and the observational data. The error corresponding to the front part of the curve could be additive, resulting in larger cumulative errors for the end of the curve, thus making it important to improve the accuracy at the front of the curve.

There are three main reasons for the errors. First, the resistance and bend angle relationship of the flex sensor has a nonlinearity at small bend angles. Second, the data extracted from the physical picture results in larger errors in the error analysis. Third, the measurement errors related to small misalignments of the sensors are due to sensor instabilities when the cable moved.

Conclusions and Further Research

This paper described a novel method for underwater cable detection based

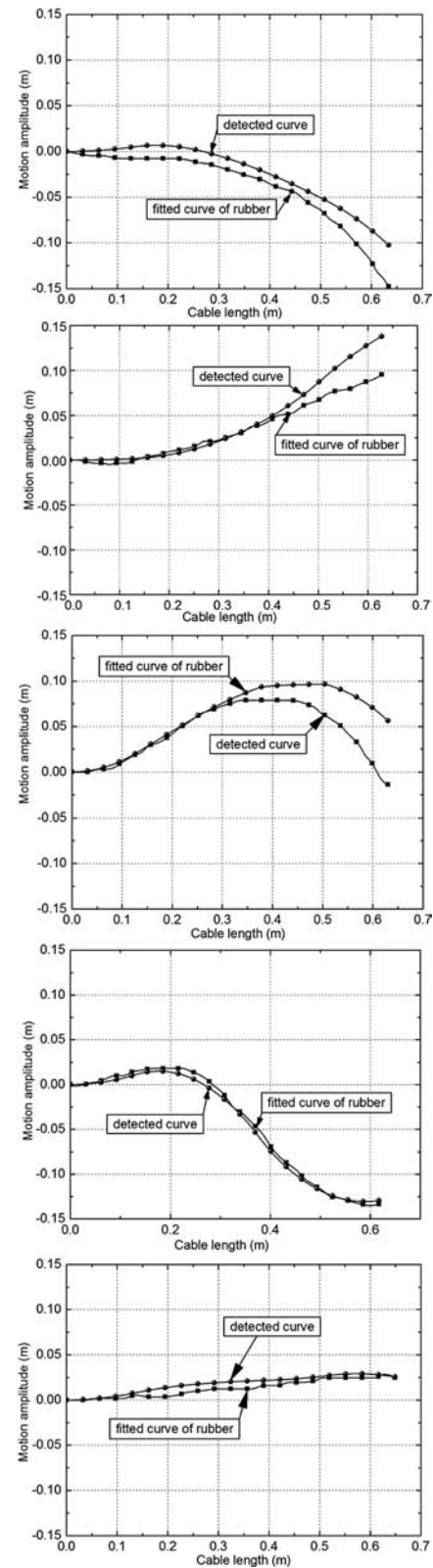
TABLE 1

The mean absolute error and similarity between the detected data and fitted curve of the rubber.

Position	Mean Absolute Error (cm)	Similarity
Down	1.4092	0.98485
Up	0.98389	0.99162
S1	1.6036	0.94422
S2	0.37699	0.99507
Flat	0.48044	0.97618

FIGURE 10

Comparison between the detected data and the fitted curve of rubber corresponding to Figure 9.



on flex sensors. Through real-time detection of underwater cable bend states, underwater accidents that result from underwater cable bending will be forecasted and prevented. Compared with common methods, the advantages of the proposed technique include the following: (1) The sensor is a separate device as well as the camera, but does not require another platform. (2) Flex sensors can be arranged along the whole cable to realize whole cable real-time detection with low cost. The number of the sensors depends on the user. The more sensors, the more accurate. (3) The novel detection methods for cables can be deployed in marine or terrestrial environments with poor visual conditions; for example, towlines, cables of anchor, and mooring system. A water tank experiment showed that the proposed system is feasible as it could accurately detect the underwater cable bending. Nevertheless, further research is still required—particularly for developing a 3-D model for underwater cable bending and torsion.

Acknowledgments

This study was funded by the Project (No. 51004085) supported by the National Science Foundation of China and the Program for Zhejiang Leading Team of S&T Innovation (No. 2010R50036). The authors thank the anonymous reviewers for their detailed and valuable comments, which strengthened this manuscript.

Corresponding Author:

Jiawang Chen
Ocean College, Zhejiang University,
Hangzhou 310058, China
Email: arwang@zju.edu.cn

References

- Bagnitsky**, A., Inzartsev, A., Pavin, A., Melman, S., & Morozov, M. 2011. Side scan sonar using for underwater cables & pipelines tracking by means of AUV. In Underwater Technology (UT), 2011 IEEE Symposium on and 2011 Workshop on Scientific Use of Submarine Cables and Related Technologies (SSC) (pp. 1-10). Tokyo, Japan: IEEE. <http://dx.doi.org/10.1109/ut.2011.5774119>.
- Brown**, K., Capus, C., Pailhas, Y., Petillot, Y., & Lane, D. 2011. The application of bio-inspired sonar to cable tracking on the sea-floor. EURASIP J Adv Sig Pr. 2011:484619. <http://dx.doi.org/10.1155/2011/484619>.
- Capus**, C., Pailhas, Y., Brown, K., & Lane, D. 2010. Detection of buried and partially buried objects using a bio-inspired wideband sonar. In: OCEANS 2010 IEEE, 24–27 May. Sydney: IEEE. 1-6. <http://dx.doi.org/10.1109/oceanssyd.2010.5603675>.
- Carter**, L., Gavey, R., Talling, P.J., & Liu, J.T. 2014. Insights into submarine geohazards from breaks in subsea telecommunication cables. Oceanography. 27(2):58-67. <http://dx.doi.org/10.5670/oceanog.2014.40>.
- Carter**, L., Milliman, J.D., Talling, P.J., Gavey, R., & Wynn, R.B. 2012. Near-synchronous and delayed initiation of long run-out submarine sediment flows from a record-breaking river flood, offshore Taiwan. Geophys Res Lett. 39(12):12603. <http://dx.doi.org/10.1029/2012GL051172>.
- El-Fakdi**, A., & Carreras, M. 2013. Two-step gradient-based reinforcement learning for underwater robotics behavior learning. Robot Auton Syst. 61(3):271-82.
- Fahn**, C.S., & Sun, H. (2010). Development of a fingertip glove equipped with magnetic tracking sensors. Sensors. 10(2):1119-40. <http://dx.doi.org/10.3390/s100201119>.
- Inzartsev**, A.V., & Pavin, A.M. 2008. AUV cable tracking system based on electromagnetic and video data. In: OCEANS 2008-MTS/IEEE Kobe Techno-Ocean (pp. 1-6). Kobe, Japan: IEEE. <http://dx.doi.org/10.1109/oceanskobe.2008.4531082>.
- Isaacs**, J.C., & Goroshin, R. 2010. Automated cable tracking in sonar imagery. In: OCEANS 2010, 20–23 Sept, Seattle, WA: IEEE. 1-7. <http://dx.doi.org/10.1109/oceans.2010.5664414>.
- Jordán**, M.A., Berger, C., & Bustamante, J.L. 2011. Design of a vision-based sensor of position and rate for the guidance of autonomous underwater vehicles. Sensors. 5:6.
- Kaniusas**, E., Pfutzner, H., Mehnen, L., Kosel, J., Varoneckas, G., Alonderis, A., ... Marquardt, B. 2004. Magnetoelastic skin curvature sensor for biomedical applications. In Sensors, 2004. Proceedings of IEEE (pp. 1484-1487). Vienna, Austria: IEEE.
- Kuhn**, V.N., Drews, P.L.J., Jr, Gomes, S.C.P., Cunha, M.A.B., & da Costa Botelho, S.S. 2013. Automatic control of a ROV for inspection of underwater structures using a low-cost sensing. J Braz Soc Mech Sci. 1-14.
- Lee**, D., Kim, G., Kim, D., Myung, H., & Choi, H.T. 2012. Vision-based object detection and tracking for autonomous navigation of underwater robots. Ocean Eng. 48:59-68. <http://dx.doi.org/10.1016/j.oceaneng.2012.04.006>.
- Lorusso**, F., Scilingo, E.P., Tesconi, M., Tognetti, A., & Rossi, D.D. 2005. Strain sensing fabric for hand posture and gesture monitoring. IEEE T Inf Technol B. 9(3):372-81.
- Majidi**, C., Kramer, R., & Wood, R.J. 2011. A non-differential elastomer curvature sensor for softer-than-skin electronics. Smart Mat St. 20(10):105017. <http://dx.doi.org/10.1088/0964-1726/20/10/105017>.
- Mandhouj**, I., Amiri, H., Maussang, F., & Solaiman, B. 2012. Sonar image processing for underwater object detection based on high resolution system. In: SIDOP 2012: 2nd Workshop on Signal and Document Processing (Vol. 845, pp. 5-10). CEUR Workshop Proceedings.
- Ortiz**, A., & Antich, J. 2014. Bayesian visual tracking for inspection of undersea power and telecommunication cables. J Marit Res. 6(2):83-94.

- Ortiz**, A., Antich, J., & Oliver, G. 2011. A particle filter-based approach for tracking undersea narrow telecommunication cables. *Mach Vision Appl.* 22(2):283-302. <http://dx.doi.org/10.1007/s00138-009-0199-6>.
- Pei**, Y.H., Yeo, H.G., Kang, X.Y., Pua, S.L., & Tan, J. 2010. Magnetic gradiometer on an AUV for buried object detection. In: OCEANS 2010 (pp. 1-8). Seattle, WA: IEEE. <http://dx.doi.org/10.1109/oceans.2010.5664272>.
- Sakagami**, N., Ishimaru, K., Kawamura, S., Shibata, M., Onishi, H., & Murakami, S. 2013. Development of an Underwater Robotic Inspection System using Mechanical Contact. *J Field Robot.* 30(4):624-40. <http://dx.doi.org/10.1002/rob.21463>.
- Saggio**, G. 2014. A novel array of flex sensors for a goniometric glove. *Sensor Actuat A-Phys.* 205:119-25. <http://dx.doi.org/10.1016/j.sna.2013.10.030>.
- Saggio**, G., Bisegna, P., Latessa, G., & Bocchetti, S. 2009a. Mechanical modeling of bend sensors exploited to measure human joint movements. In World of Wireless, Mobile and Multimedia Networks & Workshops, 2009. WoWMoM 2009. IEEE International Symposium on a (pp. 1-4). Kos: IEEE. <http://dx.doi.org/10.1109/wowmom.2009.5282407>.
- Saggio**, G., Bocchetti, S., Pinto, C.A., Orengo, G., & Giannini, F. 2009b. A novel application method for wearable bend sensors. In Applied Sciences in Biomedical and Communication Technologies, 2009. ISABEL 2009. 2nd International Symposium on (pp. 1-3). Bratislava: IEEE. <http://dx.doi.org/10.1109/isabel.2009.5373625>.
- Szyrowski**, T., Sharma, S. K., Sutton, R., & Kennedy, G. A. 2013a. Developments in subsea power and telecommunication cables detection: Part 1—Visual and hydroacoustic tracking. *Underwater Technol.* 31:123-32. <http://dx.doi.org/10.3723/ut.31.123>.
- Szyrowski**, T., Sharma, S.K., Sutton, R., & Kennedy, G.A. 2013b. Developments in subsea power and telecommunication cables detection: Part 2—Electromagnetic detection. *Underwater Technol.* 31:133-43. <http://dx.doi.org/10.3723/ut.31.133>.
- Talling**, P.J., Paull, C.K., & Piper, D.J. 2013. How are subaqueous sediment density flows triggered, what is their internal structure and how does it evolve? Direct observations from monitoring of active flows. *Earth-Sci Rev.* 125:244-87. <http://dx.doi.org/10.1016/j.earscirev.2013.07.005>.
- Villar**, S.A., Acosta, G.G., Sousa, A.L., & Rozenfeld, A. 2014. Evaluation of an efficient approach for target tracking from acoustic imagery for the perception system of an autonomous underwater vehicle. *Int J Adv Robot Syst.* 11:24.
- Wang**, P., Goddard, K., Lewin, P., & Swingler, S. 2011. Electromagnetic field application to Underground Power Cable Detection. In: 17th International Symposium on high voltage engineering. 22–26 August 2011, Hannover, Germany: Leibniz Universitat Hannover.
- Wirth**, S., Ortiz, A., Paulus, D., & Oliver, G. 2008. Using particle filters for autonomous underwater cable tracking. In: IFAC Workshop on Navigation, Guidance and Control of Underwater Vehicles. Killaloe, Ireland: International Federation of Automatic Control. 161-6.
- Zhou**, X., Wang, Y., & Zhou, Y. 2009. Research on modeling and experimentation on detecting buried depth of optical fiber submarine cables based on active detection technique. In: Electronic Measurement & Instruments, 2009. ICEMI'09 (pp. 1-91). Beijing, China: IEEE. <http://dx.doi.org/10.1109/ICEMI.2009.5274300>.
- Zhou**, X.J., Zhang, Y., Zuo, M.J., & Yuan, Z.D. 2015. Research on submarine cable detection technology based on information fusion. In: 2015 International Industrial Informatics and Computer Engineering Conference. Atlantis Press. <http://dx.doi.org/10.2991/iiicec-15.2015.121>.

Effect of Low Temperature and High Pressure on Deep-Sea Oil-Filled Brushless DC Motors

AUTHORS

Minjian Cai

Shijun Wu

Canjun Yang

State Key Laboratory of Fluid Power and Mechatronic Systems,
Zhejiang University

Introduction

With various instruments and undersea vehicles unveiling the mystery of thousands of meters under the sea, we can now gain a better understanding of the geology, topography, and benthos of the deep ocean. However, because of the complicated and extreme environment, it is still a challenge to design a reliable and efficient system for use in such an environment. For most deep-sea equipment, electric actuators play a vital role in accomplishing specific tasks such as adjusting a pan-tilt mechanism for camera orientation, displacement of a robot arm, and driving a pump in a fluid system. An efficient actuator not only contributes to prolonged battery life but also reduces heat dissipation and enhances reliability of the whole system.

Motors have been widely used in subsea applications because of their efficiency and versatility. Tan et al. (2010, 2012) have been using an oil-filled stepper motor to drive a micro-metering pump for underwater pH sensor calibration. Conventional DC motors are also widely used in undersea mechatronic systems because of their outstanding speed adjustment feature and large output torque.

ABSTRACT

The principle of electronic commutation makes brushless DC motors suitable for deep-sea application by sealing the motor in an oil-filled housing. However, if the oil-filled actuator is not designed properly, it will malfunction in the deep sea in spite of its excellent performance on land. In this paper, oil viscosity variations with pressure and temperature are reviewed because both factors vary with the operating depth, and a practical approach to estimate the viscous torque is advanced based on a viscous drag model of the selected motor and the properties of the oil. An experimental rig that can simulate the deep sea environment was developed, by which a series of experiments to study the motor efficiency and dynamic performance in different conditions were conducted. The values of viscous torque obtained in the experiments agreed well with our estimation. The low efficiency in the 2°C experimental group confirmed the influence of temperature, while the dramatic difference in the dynamic performance of the motor when filled with different oils verified the importance of analyzing the properties of the oil and of making a deliberate selection.

Keywords: deep sea, high pressure, low temperature, oil-filled motor, oil properties

Nomenclature

T_0	Normal temperature
P_0	Atmospheric pressure
μ	Dynamic viscosity
μ_0	Dynamic viscosity at given temperature T_0 and pressure P_0
ρ	Density
P	Pressure
T	Temperature
α	Pressure-viscosity coefficient
η	Kinetic viscosity
$\sqrt{T_a}$	Taylor number
M_v	Viscous drag moment
M_C	Viscous drag moment acting on cylinder flank
C_M	Moment coefficient
R_i	Rotor diameter
C	Air-gap clearance
L	Rotor length
B	Clearance between housing and end face of the motor
ω	Rotor angular velocity
R_e	Reynolds number
k	Coefficient relating to the motor geometry
P_{el}	Input electric power
P_{ir}	Iron power loss

P_{me}	Mechanical power
P_j	Joule power loss
R	Phase resistance
U	Input voltage
I	Input current

Krishfield et al. (2008) used a DC motor to drive the traction unit in ice-tethered profilers. The motor runs in air within the thick pressure case with its torque transferred via a magnetic coupler. Saegusa et al. (2006) employed a DC motor to drive a pump to adjust the sampling rate in their multibottle fluid sampler. Seewald et al. (2002) developed a gas-tight sampler for hydrothermal fluids that used a DC electric motor to actuate the sampler valve. In these two cases, motors are filled with oil to compensate for the ambient pressure so as to avoid the requirement of being housed in a thick-walled metallic pressure vessel, thus protecting them from high-pressure seawater and preventing fatal damage to the motor if even a small amount of seawater seeps in. Nevertheless, in an insulated oil environment, the oil film in the brushes will affect the commutation of the motor to some extent.

The brushless DC (BLDC) motor, more and more widely used due to its high reliability, efficiency, and control performance, has been used successfully in the design of thrusters and manipulators of underwater vehicles (Bhangu et al., 2005; Lewandowski et al., 2008). The electronic commutation of a BLDC motor eliminates the potential for poor electrical contacts, which makes it suitable for a variety of oceanic apparatus such as positioning systems of undersea laser spectrometers and underwater robotics (Kunz et al., 2008; Peng et al., 2014; White et al., 2005). However, oil-filled

motor-based drive systems cannot arbitrarily be designed because the oil properties change dramatically with the pressures and temperatures of the deep ocean. The viscous drag introduced by the cold and compressed oil affects the efficiency and load matching of the motor. Up to now, little is known about exactly how the deep sea environment affects oil-filled motors.

Viscous drag produced by the rotor may not be so obvious in ordinary environments, but it becomes significant when an oil-filled motor works in the cold deep sea if an unsuitable kind of insulating oil is used. Therefore, study of the viscous drag force in oil-filled motors is valuable for those working in the deep-sea engineering field. Some previous research has been carried out to minimize the impact of viscous drag on the motor rotor. Ahmed and Toliyat (2007) presented a design procedure for submersible motors and corroborated their design consideration of coupled-field analysis needs based on their simulation results. Zou et al. (2012) designed an oil-filled BLDC motor that takes into account the effect of high pressure. They analyzed the composition of the total loss and drew a comparison between the results for normal pressure and high pressure, which highlighted the need to consider the pressure effect. These studies provide useful information for oil-filled motor design; however, they have emphasized the need for comprehensive consideration of the relevant parameters but neglected some specific details such

as the properties of the oil and the important environmental factor, i.e., temperature.

In this paper, we analyzed the viscous drag torque of a BLDC motor in different compensating oils and studied the actual effects on it of temperature and pressure. A simplified analytical model to calculate the potential viscous moment is described in the Analysis and Modeling section, and the effects of both temperature and pressure on the insulating oil are discussed and taken into consideration. In the Experimental Setup and Method section, a simulation environment that was developed to provide different temperatures and pressures is described. A series of experiments under different conditions were carried out to study viscous drag loss and transient response of the motor. The results and discussion are presented in the Results and Discussion section.

Analysis and Modeling

Because the viscosity behavior of the compensating liquid under low temperatures and high pressures is one of the key motivations for this paper, before delving into this line of research, we would like to review some proposed theories on the viscosity properties of commonly used industrial oils. Based on this knowledge of the oil properties, a quantitative analytical model was created to estimate the initial viscous drag torque in actual deep sea environments.

Oil Viscosity

The concept that oils get thicker when the temperature drops or the pressure rises is well known, which means that, in the deep sea environment, an oil's viscosity will increase

markedly due to the degradation of both of these factors.

The general form for the pressure and temperature dependence of viscosity has been known for over half a century (Bair et al., 2001), and researchers have long focused on revealing the accurate relationship of viscosity, temperature, and pressure of assorted oils (Bair et al., 2001; Gold et al., 2001). A general method of predicting the oil viscosity is the Barus equation (Gold et al., 2001).

$$\mu = \mu_0 \exp(\alpha P). \quad (1)$$

where the temperature dependence can be described by

$$\mu_0 = Q \exp\left(\frac{G}{T + P}\right). \quad (2)$$

and the pressure-viscosity coefficient α is additionally taken into account by

$$\alpha(P, T) = \frac{1}{a_1 + a_2 T + (b_1 + b_2 T)P} \quad (3)$$

where Q , G , P , a_1 , a_2 , b_1 , and b_2 need to be determined separately by experimental data for each oil, and then the Barus equation can represent the fluid behavior in a wide pressure and temperature range. Some other simplified methods to calculate the viscosity of a specific fluid are usually adopted in engineering; however, for accuracy, we will use the above equation to obtain the oil viscosity at a specific condition.

A typical hydraulic oil viscosity variation versus temperature and pressure is illustrated in Figure 1. It shows that, with the pressure increase, the viscosity increases gradually, and with the drop in temperature, especially below 20°C, the viscosity could increase dramatically.

Usually, considering the general deep sea environment ($T \geq 0^\circ\text{C}$ and $P < 110 \text{ MPa}$), the viscosity of most oil is more sensitive to temperature than pressure. This implies that we should pay more attention to the temperature factor when dealing with an oil-filled actuator used in a cold environment. As for the oil-filled motor used at such conditions, it is necessary to take both temperature and pressure into consideration when evaluating the motor's actual output torque.

In the present work, two typical oils, namely hydraulic oil (a mineral oil) and silicone oil (a synthetic oil), were used in our experiments. Hydraulic oil usually has an antiwear property and good incompressibility, while silicone oil provides compatibility with other organic materials and hydrophobic property. The ISO viscosity grade (VG) of hydraulic oil is 22, which denotes that its dynamic viscosity is 22 mm²/s at 40°C and atmospheric pressure. Because it is hard to find two different kinds of oil with equal viscosity, the silicone oil we used is 50 cSt, which should have a viscosity

of 50 mm²/s at 25°C and atmospheric pressure. As a result, viscosities of the two oils were measured to be about 41 mPa·s and 47 mPa·s, respectively, at 25°C and atmospheric pressure.

The pressure and temperature dependence of the dynamic viscosity μ is derived from equations (1) and (3) as

$$\mu = \mu_0 \exp\left[\frac{P}{A_T + B_T P}\right] \quad (4)$$

where A_T and B_T are the temperature-dependent parameters shown in equation (3). Because our work focused on two typical temperatures, namely 25°C and 2°C, we obtained the corresponding values of A_T and B_T by experiments.

Some relevant properties of the oils concerned in our research are listed in Table 1.

Modeling of Viscous Drag Moment

Along with the experiments carried out in this work, a quantitative approach to determine the effective output torque was studied. The motor used in

FIGURE 1

Viscosity variation with temperature and pressure.

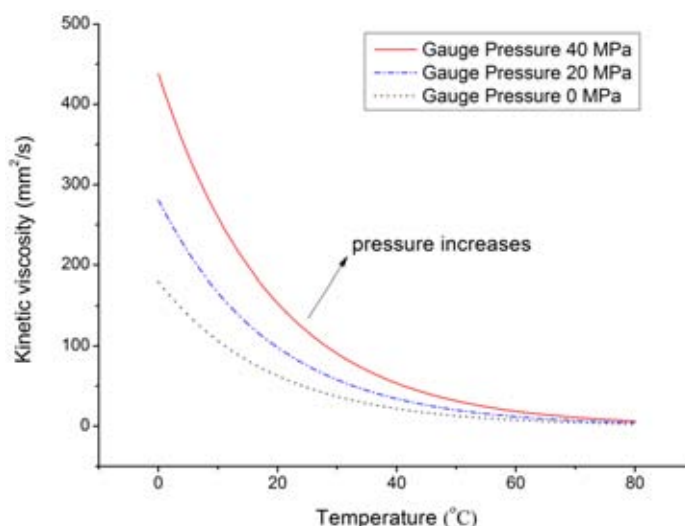


TABLE 1

Main characteristics.

Oil Type	μ_0 at 25°C	μ_0 at 2°C	α at 25°C	α at 2°C
	mPa s	mPa s	Pa ⁻¹	Pa ⁻¹
Hydraulic oil	41.6	140.3	$\frac{1}{(2.01e+07) + (5.1e-1)P}$	$\frac{1}{(4.49e+07) + (1.6e-02)P}$
Silicone oil	46.9	71.3	$\frac{1}{(1.15e+08) - (1.2e-01)P}$	$\frac{1}{(9.43e+07) + (2.8e-01)P}$

our research is shown in Figure 2a, and its main specifications and parameters are listed in Table 2. Because it is difficult to establish a precise model that takes into account detailed structures such as bearings and the hall sensor unit, a simplified model, i.e., a pair of coaxial cylinders filled with oil in the gap, was developed to study the viscous load of the oil-filled BLDC motor (Figure 2b).

As shown in Figure 2b, the viscous drag of the rotor consists of two parts: one produced by the flank of the rotor and the other produced by the end surface. Then, the fluid drag force acting on the rotor surfaces can be

calculated by identifying the flow state between the stator and rotor in advance, which can be determined by the aid of dimensionless Taylor number $\sqrt{T_a}$ introduced as

$$\sqrt{T_a} = \frac{R_i \omega C}{\eta} \sqrt{\frac{C}{R_i}} \quad (5)$$

where η is the kinetic viscosity of the fluid.

The flow pattern in the annulus region will make a transition from laminar flow to transition flow or turbulent flow when $\sqrt{T_a}$ is larger than 41.3, which leads to inapplicability of the modeling derivation if it is based on

the assumption of laminar flow (Deng, 2007; Qi et al., 2010). Bilgen and Boulos (1973) concluded a general relationship for the moment coefficient that is defined in equation (6) as a function of the geometry parameters and Reynolds number when the flow pattern varies.

$$C_M = M_C / (0.5 \pi \rho \omega^2 R_i^4 L) \quad (6)$$

$$R_e = \rho \omega R_i C / \mu \quad (7)$$

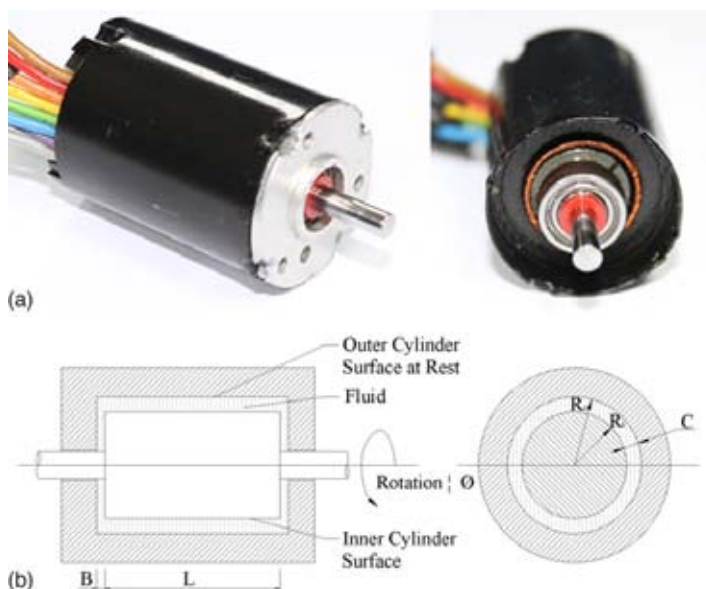
$$C_M = K(C/R_i)^n R_e^\beta \quad (8)$$

where M_C denotes the viscous drag moment exerted by the cylinder and constant K and exponents n and β can be determined by the flow regime.

In fact, for small motors, the Taylor number is usually below the critical value due to the small physical dimensions. In our case, the Taylor number was checked below the critical number for both oils (about 0.1 in silicone oil,

FIGURE 2

The BLDC motor (a) and its simplified model (b).

**TABLE 2**

Main specifications.

Specification	Value
Nominal power	12 W
Rated current	661 mA
Rated speed	7740 rpm
Rated torque	11.9 mN m
Phase resistance	12.4 ohm

giving a speed of 6,000 rpm). Hence, for Newtonian fluids whose viscous stresses are linearly proportional to strain rate, we can obtain the viscous load function as equation (9) with a basic knowledge of fluid mechanics by separating the rotor surface into the disk and flank (White, 2011).

$$M_v = \frac{\pi R_i^4 \mu \omega}{B} + \frac{4\pi R_i^3 L \mu \omega}{C} = k \mu \omega \quad (9)$$

where M_v denotes the viscous drag moment on the rotor and k is a constant related to the motor geometry. This function shows a linear relationship between viscous torque and the dynamic viscosity μ by regarding the rotor speed ω as constant. Substituting the corresponding viscosity dependence into equation (9), we can then obtain viscous moment correlation for hydraulic oil and silicone oil as

$$M_v = k \omega \mu_0 \exp \left[\frac{P}{A_T + B_T P} \right] \quad (10)$$

where the relevant parameters are listed in Table 1.

Consequently, once we obtain the geometry parameter k by measuring viscous moment in a known condition, we can use equation (10) to calculate the viscous torque in various environments given the actual working temperature and pressure values. In our study, the results for a velocity of 2,000 rpm are listed in Table 3.

We can see that the potential viscous load torque increases sharply when the temperature is low or the pressure is high if we fill the motor with hydraulic oil, and the low temperature seems to have the worst impact on the start-up process. The silicone oil, however, seems to have much less impact on the motor output.

TABLE 3

Calculated results of initial viscous moment at 2,000 rpm.

Condition	In Hydraulic Oil (mN m)	In Silicone Oil (mN m)
25°C and 0 MPa (tested)	17.32	20.21
25°C and 20 MPa	32.55	24.13
25°C and 40 MPa	43.63	29.04
25°C and 60 MPa	51.67	35.23
2°C and 0 MPa	58.29	26.59
2°C and 20 MPa	91.02	32.48
2°C and 40 MPa	142.59	38.85
2°C and 60 MPa	221.05	45.63

The torque calculated here is the viscous drag torque at the starting stage that neglects temperature rising.

Experimental Setup and Method

Experimental Setup

An experimental rig was designed to simulate the deep sea environment. The whole test rig consisted of three parts: a high-pressure reservoir, a temperature regulation module, and a control and data acquisition unit (Figure 3a). The main structural features of the test rig are presented in Figure 3b.

Pressure of up to 60 MPa in the test apparatus was supplied by a high-pressure test pump. The temperature regulation system mainly comprised a commercial recirculating cooler, a cooling jacket, and a special thermocouple that penetrated into the pressure reservoir. The cooler pumps recirculate water into the cooling jacket and receive it at the outlet, making the fast-flowing water transfer heat between the pressure reservoir and cooling water. By comparing the set temperature and the monitored temperature from thermocouple, the recirculating cooler finally regulated the inner water temperature in a closed-loop manner to an accuracy of $\pm 0.2^\circ\text{C}$.

The BLDC motor was encapsulated in an oil-filled vessel that was located in

the high-pressure reservoir. A rubber sleeve in the oil-filled vessel and two groups of holes distributed around the metallic housing (as shown in Figure 3b) ensured the pressure balance. The oil-filled vessel was filled carefully, and the motor was kept running long enough to remove all air bubbles in the motor. Two surface-mounted thermal resistors attached to the motor housing surface were used to measure the oil temperature, by which we could guarantee that the motor ran in the expected temperature condition.

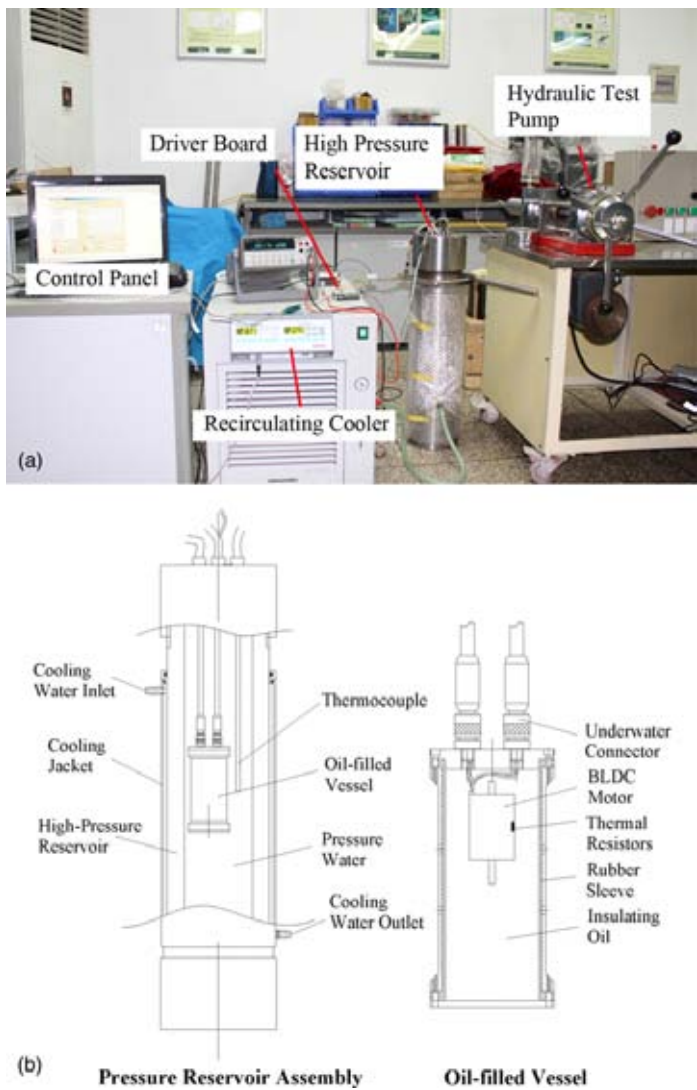
The motor and its driver were supplied by a 24-V regulated power supply. The motor speed was set by a virtual control panel on a PC, which also recorded the electric current and temperature values synchronously. Both of the current and temperature values acquired by the driver board were calibrated, apart from a few unavoidable measurement errors.

Method

To have an intuitive understanding of the viscous torque caused by the oil in a deep sea environment and to verify the estimated approach introduced above, the motor was set to operate

FIGURE 3

Experimental apparatus. (a) Low-temperature and high-pressure environment. (b) Inner schematic of the high-pressure reservoir.



in different conditions. The power of the motor without oil and load was first measured at room temperature (25°C) and atmospheric pressure. The vessel was then successively filled with two kinds of oils, and a constant temperature environment was provided. For each kind of oil, the experiments were divided into two groups: one at 25°C and the other at 2°C . Both experiments were undertaken in the same pressure series to study the influence of different depths.

According to the energy conservation principle, the input electrical power is converted into mechanical power P_{me} with associated joule power loss P_j and iron loss P_{ir} .

$$P_{\text{el}} = P_{\text{me}} + P_{\text{ir}} + P_j \quad (11)$$

Because the motor runs with no external load, the mechanical power P_{me} is replaced by P_v , which can be rewritten in detail as

$$UI = \omega M_v + P_{\text{ir}} + I^2 R. \quad (12)$$

The joule power loss depends on the winding R and input current, while mechanical power P_{me} is related to the angular velocity and torque exerted on the rotor. Previous literature has indicated that the iron loss becomes larger with deterioration of the magnetic property caused by mechanical stress (Fujisaki et al., 2007; Fujisaki & Satoh, 2004; Takahashi & Miyagi, 2011). However, from a different perspective, the iron loss increased by the compressive stress is relatively small (about 1 W/kg with a stress of 100 MPa and a flux density of 0.5 T) compared with the other terms (Takahashi & Miyagi, 2011). So we regarded the iron loss term as a constant (0.3 W) during experimental data processing. By subtracting P_{ir} and P_j , we could determine M_v , which indicates the viscous term.

As discussed in the Analysis and Modeling section, the viscous drag torque depends on the inner geometry of the motor, velocity, and oil viscosity. Because the viscosity is closely related to the temperature and the heat produced by the motor varies with the operating condition, the calculation of the real-time viscous drag torque is then complicated. To simplify the analysis, all viscous torque results from our calculation focused only on the starting stages, while the experimental results provided both initial and steady state data. The following assumptions were made in this study.

1. In the starting stage, the oil temperature stayed constant, and the oil temperature in the motor was regarded as uniform.
2. The influence of pressure and temperature on the motor's magnetic material was neglected compared with that of the compensating oil.

Results and Discussion

The viscous drag moment decreases as the motor temperature rises after start-up, and then it reaches a steady value when the motor is in thermal equilibrium. What we are concerned about is the initial viscous torque that influences motor's start-up performance and the steady viscous power loss that matters in the continuous operation. The following results of the experiments revealed the influence of both temperature and pressure on the oil-filled BLDC motor and highlighted the importance of analyzing the properties of compensating oil.

Start-Up Performance

The influence of pressure on the motor filled with two kinds of oil is shown in Figure 4. As predicted by the calculation, the viscous torque at the starting stage increased gradually in both cases as the pressure climbed. It is noteworthy that, when the motor was compensated in hydraulic oil, part of the difference between tested result and calculated value at

60 MPa is due to the power limitation of the motor. At this condition, the motor could not provide large enough torque to overcome the increased viscous drag moment if it were set to run at a faster speed, and it would have a problem at start-up if it were connected to an extra load. Benefiting from low sensitivity to pressure, the power margin of the motor in silicone oil was larger compared with that in hydraulic oil. Nevertheless, the problem still exists when the pressure continues to increase if we do not analyze the potential viscous load beforehand.

The viscous drag influenced by low temperature was so significant that the motor would actually not be able to run to the set speed immediately as in normal environment. As shown in Figure 5, the current data recorded in the first 2 min after giving the motor a step velocity signal confirm the existence of deterioration in the transient process.

From the current responses in the first 20 s, as shown in Figures 5a and

5b, we can see how the pressure and temperature (especially the temperature) deteriorate the motor's start-up performance. In the case of hydraulic oil at 2°C, as a result of the influence of low temperature on viscosity, the motor had almost reached the locked rotor current at the pressure of 20 MPa. The time of overcurrent lasted longer to allow the motor to overcome the heavy viscous torque after pressurizing to 60 MPa. The current stayed above its rated value for almost 1 min and then dropped below this value as the oil temperature rose. For all three low-temperature experiments, the motor consumed much more current than when it was running at room temperature, until the inner oil temperature reached a stable level. As can be foreseen, such overcurrent will easily cause damage to the electronic components and the motor windings, particularly in the intermittent operation mode.

The silicone oil fared better because of its low sensitivity to temperature. It could successfully start up even at 2°C and high pressure of up to 60 MPa. Moreover, the current curve shows that the initial viscous moment was much less than it could reduce the possibility of malfunction during start-up. However, the differences of the steady current values in the two cases are not that apparent.

Figure 5c shows the velocity and temperature details of the motor filled with hydraulic oil after it was started. It can be seen that the motor failed to accelerate immediately to its set speed due to the heavy viscous load and almost stalled. Benefiting from the heat produced by itself, the motor then slowly sped up to overcome the velocity-dependent viscous drag moment. This resulted in a rapid current decrease when the motor reached

FIGURE 4

Comparison between experimental and calculated results of viscous torque when compensated with hydraulic oil and silicone oil at room temperature.

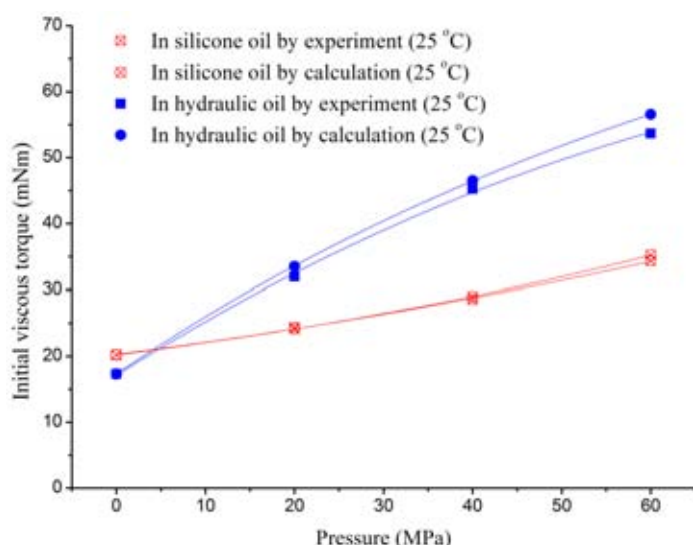
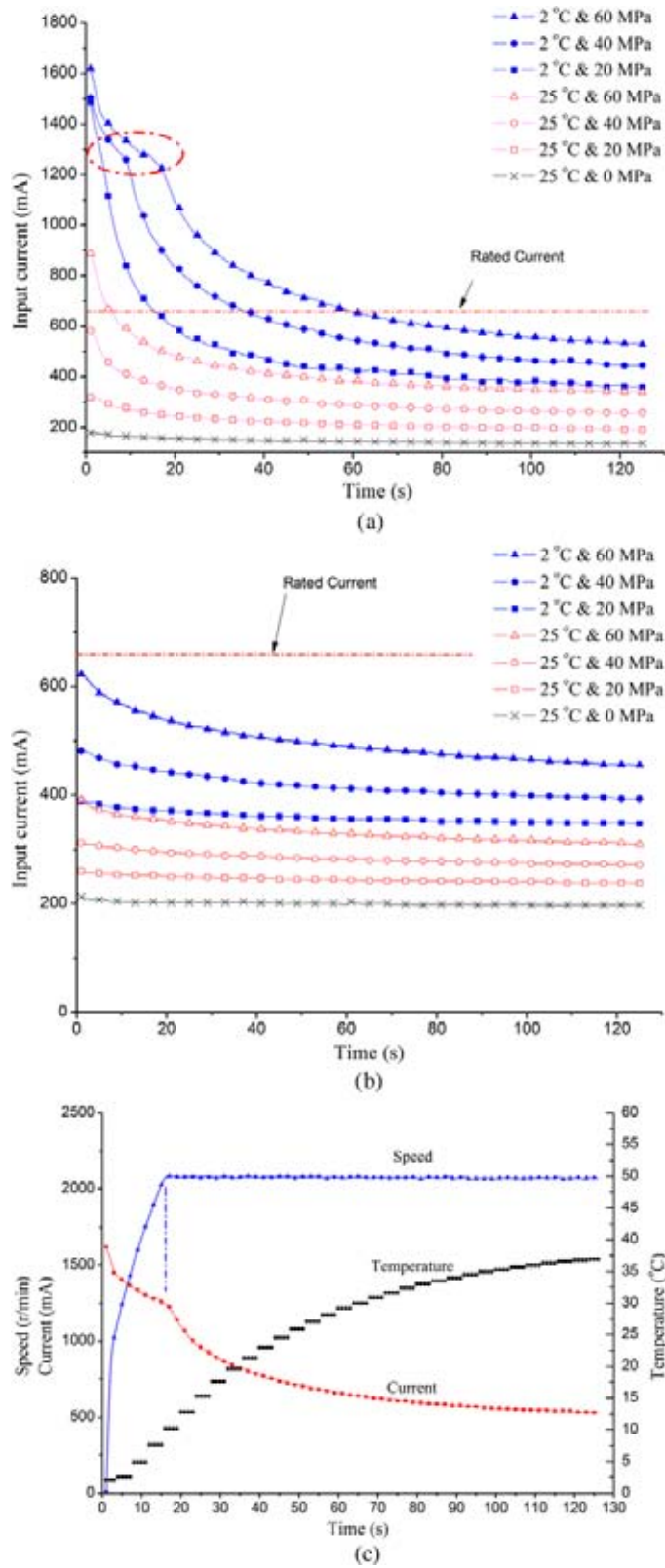


FIGURE 5

Current variation comparison between 25°C and 2°C when giving a step speed signal of 2,000 rpm.
 (a) Hydraulic oil. (b) Silicone oil. (c) Speed and current versus time when the motor was running in hydraulic oil at the experimental condition of 2°C and 60 MPa.



the set speed because the viscous moment did not increase anymore.

Viscous Power Loss

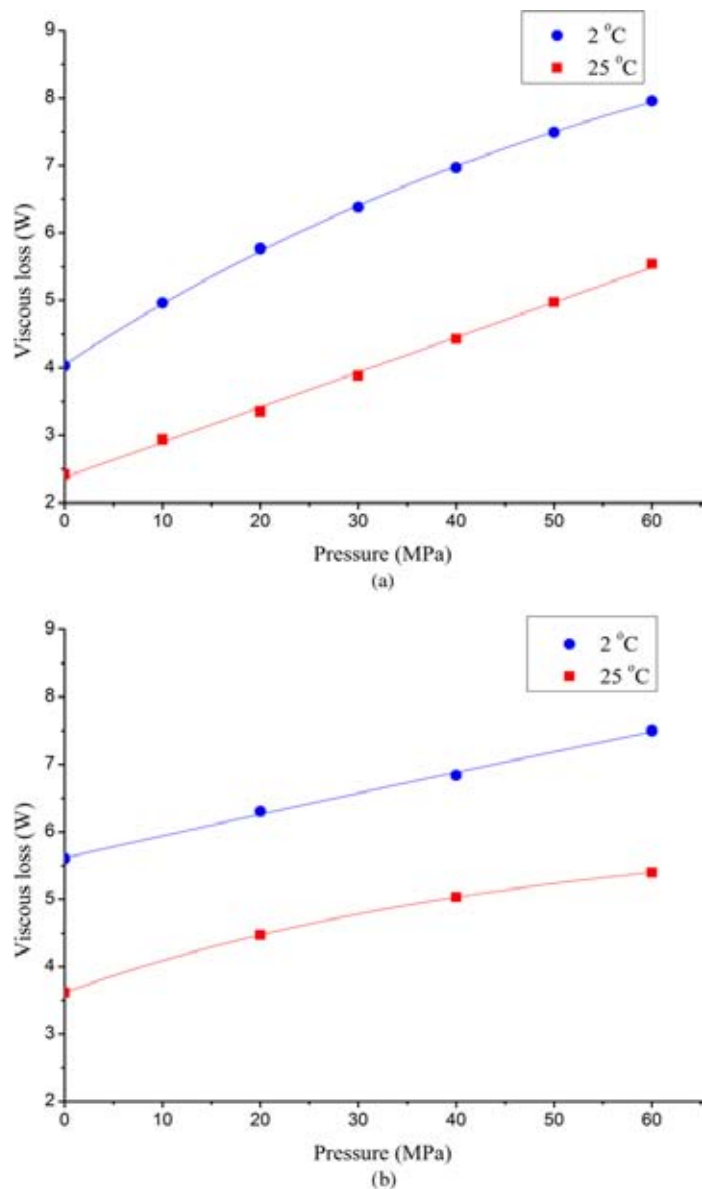
The results of the steady viscous power loss P_{me} are presented in Figure 6. According to equation (10), the steady viscous loss should increase exponentially with the pressure, but these data showed a linear trend. This can mainly be ascribed to the different final oil temperature, which offsets part of the loss. The significant differences between the results at 25°C and 2°C show that ambient temperature also had a remarkable impact on motor efficiency. Specifically, when the motor was filled with hydraulic oil, the loss in the low-temperature condition would increase by 70% and 57% at 40 and 60 MPa, respectively, compared with those measured at room temperature. Moreover, it has almost reached its rated power at 2°C and 60 MPa in this case. This indicates that the motor's speed will decrease or simply fail when driving a load. On the other hand, the steady power loss for the silicone oil case is only slightly lower. With the motor running, the rising temperature did not reduce distinct viscous torque as it did in hydraulic oil. The steady viscous loss was about 7.6 W at the worst condition. Consequently, the low temperature and high pressure directly led to a scarcity of the available output torque and a low efficiency.

Lower Viscosity Silicone Oil

To reduce power dissipation and prevent excessive overcurrent, one simple way is to replace the thick oil with a low-viscosity oil that has good fluidity, even in the deep sea environment. Because silicone oil has a wide range of viscosity options and its viscosity-temperature coefficient is low, we

FIGURE 6

Viscous power loss at different conditions when filled with (a) hydraulic oil and (b) silicone oil at a speed of 2,000 rpm.



used silicone oil of 5 cSt ($5 \text{ mm}^2/\text{s}$ at 25°C and atmospheric pressure) as a demonstrative case in our study. Table 4 shows the steady viscous power loss of the motor in the three cases.

In addition, by benefiting from the low viscosity at different conditions, the viscous moments in Figure 7 indicate a significant improvement in efficiency as well as a reduction in the

possibility of stalling. Thus, by analyzing the viscous drag model and the properties of different oils, we can determine how the oil-filled actuator will behave and eventually implement an efficient and reliable design.

Conclusion

In this paper, we investigated the influence of both the temperature

and pressure on an oil-filled BLDC motor by the viscous drag model and an experimental rig that can simulate the deep sea environment. Experiments validated that the pressure and temperature had a marked effect on the power loss and dynamic performance of the oil-filled motor.

Two typical types of oils (hydraulic oil and silicone oil) were used in our study. From the two groups of experiments, the steady power loss increased as the pressure climbed or temperature dropped. In addition, the temperature had a dramatic effect on the start-up performance if the motor is filled with hydraulic oil. When the ambient temperature was low (2°C), the viscosity of the hydraulic oil (ISO VG 22) increased sharply, which overloaded the motor, and the resulting overcurrent lasted until the temperature rose. The silicone oil performed much better because of its low temperature sensitivity. The results highlight the importance of analyzing the properties of compensating oil and indicate that the temperature and pressure should both be taken into consideration when using a compensating oil in the drive system designed for the deep sea.

In addition to the experimental work that was conducted, a semi-experimental method to calculate the potential starting torque was advanced, the results of which agreed well with the experimental results. By determining the viscous loss in an ordinary environment, we can then obtain the potential viscous torque using equation (10) at specified conditions. Although our test object in this study was a BLDC motor, the method can be applied to other rotating electrical machines.

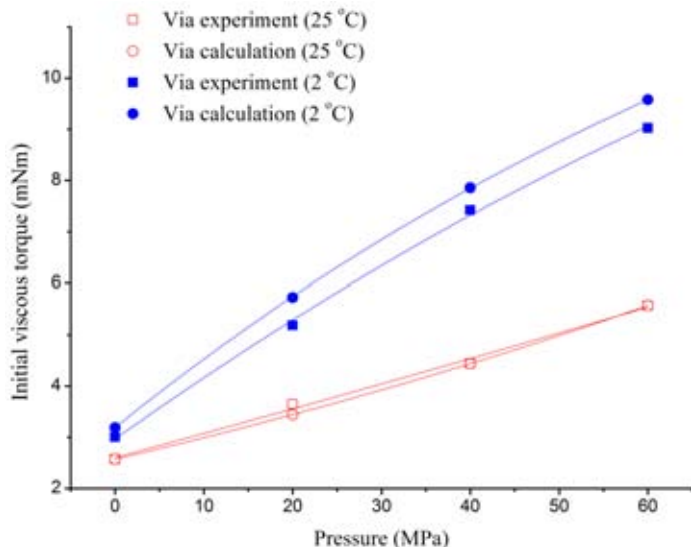
TABLE 4

Steady power loss comparison between three compensating oils at 2,000 rpm.

Experimental Condition	Viscous Loss for Hydraulic Oil (ISO VG 22) (W)	Viscous Loss for Silicone Oil (50 cSt) (W)	Viscous Loss for Silicone Oil (5 cSt) (W)
25°C and 0 MPa	2.47	3.62	0.43
25°C and 20 MPa	3.35	4.47	0.68
25°C and 40 MPa	4.43	5.03	0.83
25°C and 60 MPa	5.54	5.40	1.04
2°C and 20 MPa	5.77	6.30	0.95
2°C and 40 MPa	6.97	6.84	1.26
2°C and 60 MPa	7.96	7.50	1.61

FIGURE 7

Results of viscous torque tested at different conditions when compensated with silicone oil of 5 cSt (velocity = 2,000 rpm).



Acknowledgments

This work was supported by the National Natural Science Foundation of China and the Science Fund for Creative Research Groups of the National Natural Science Foundation of China (Nos. 41106081 and 51521064). The authors would like to thank H. Sun for his help in the design of the control panel and K. Li and G. Ma for their help during the experiments.

Corresponding Author:

Shijun Wu
State Key Laboratory of Fluid Power and Mechatronic Systems, Zhejiang University, Hangzhou 310027, China
Email: bluewater@zju.edu.cn

References

Ahmed, S., & Toliyat, H. 2007. Coupled field analysis needs in the design of submersible electric motors. In: Electric Ship

Technologies Symposium, 2007. ESTS'07. IEEE. pp. 231-7. Arlington, VA: IEEE.
<http://dx.doi.org/10.1109/estss.2007.372091>.

Bair, S., Jarzynski, J., & Winer, W.O. 2001. The temperature, pressure and time dependence of lubricant viscosity. Tribol Int. 34(7): 461-8. [http://dx.doi.org/10.1016/S0301-679X\(01\)00042-1](http://dx.doi.org/10.1016/S0301-679X(01)00042-1).

Bhangu, B.S., Snary, P., Bingham, C.M., & Stone, D.A. 2005. Sensorless control of deep-sea ROVs PMSMs excited by matrix converters. In: Power Electronics and Applications, 2005 European Conference on. pp. 1-8. Dresden, Germany: IEEE. <http://dx.doi.org/10.1109/epc.2005.219602>.

Bilgen, E., & Boulos, R. 1973. Functional dependence of torque coefficient of coaxial cylinders on gap width and Reynolds numbers. J Fluid Eng-T ASME. 95(1):122-6. <http://dx.doi.org/10.1115/1.3446944>.

Deng, D. 2007. A numerical and experimental investigation of Taylor flow instabilities in narrow gaps and their relationship to turbulent flow in bearings. Ph.D. thesis, Akron University, 305 pp.

Fujisaki, K., Hirayama, R., Kawachi, T., Satou, S., Kaidou, C., Yabumoto, M., & Kubota, T. 2007. Motor core iron loss analysis evaluating shrink fitting and stamping by finite-element method. IEEE T Magn. 43(5): 1950-4. <http://dx.doi.org/10.1109/TMAG.2006.877041>.

- Fujisaki**, K., & Satoh, S. 2004. Numerical calculations of electromagnetic fields in silicon steel under mechanical stress. *IEEE T Magn.* 40(4):1820-5. <http://dx.doi.org/10.1109/TMAG.2004.830509>.
- Gold**, P.W., Schmidt, A., Dicke, H., Loos, J., & Assmann, C. 2001. Viscosity-pressure-temperature behaviour of mineral and synthetic oils. *J Syn Lubr.* 18(1):51-79. <http://dx.doi.org/10.1002/jsl.3000180105>.
- Kunz**, C., Murphy, C., Camilli, R., Singh, H., Bailey, J., Eustice, R., ... Sohn, R. 2008. Deep sea underwater robotic exploration in the ice-covered arctic ocean with AUVs. In: Intelligent Robots and Systems, 2008. IROS 2008. IEEE/RSJ International Conference on. pp. 3654-60. Nice, MN: IEEE. <http://dx.doi.org/10.1109/iros.2008.4651097>.
- Krishfield**, R., Toole, J., Proshutinsky, A., & Timmermans, M.L. 2008. Automated ice-tethered profilers for seawater observations under pack ice in all seasons. *J Atmos Ocean Tech.* 25(11):2091-105. <http://dx.doi.org/10.1175/2008JTECHO587.1>.
- Lewandowski**, C., Akin, D., Dillow, B., Limparis, N., Carignan, C., Singh, H., & Sohn, R. 2008. Development of a deep-sea robotic manipulator for autonomous sampling and retrieval. In: 2008 IEEE/OES Autonomous Underwater Vehicles. pp. 14-9. Woods Hole, MA: IEEE. <http://dx.doi.org/10.1109/auv.2008.5290533>.
- Peng**, S., Yang, C., Fan, S., Zhang, S., Wang, P., & Chen, Y. 2014. Hybrid underwater glider for underwater docking: Modeling and performance evaluation. *Mar Technol Soc J.* 48(6):112-24. <http://dx.doi.org/10.4031/MTSJ.48.6.5>.
- Qi**, W., Zhou, J., & Li, J. 2010. Numerical calculation of viscous drag loss of oil-filled BLDC motor for underwater applications. In: 2010 International Conference on Electrical Machines and Systems (ICEMS). pp. 1739-42. Incheon, Korea: IEEE.
- Saegusa**, S., Tsunogai, U., Nakagawa, F., & Kaneko, S. 2006. Development of a multi-bottle gas-tight fluid sampler WHATS II for Japanese submersibles/ROVs. *Geofluids.* 6(3):234-40. <http://dx.doi.org/10.1111/j.1468-8123.2006.00143.x>.
- Seewald**, J.S., Doherty, K.W., Hammar, T.R., & Liberatore, S.P. 2002. A new gas-tight isobaric sampler for hydrothermal fluids. *Deep-Sea Res Pt I.* 49(1):189-96. [http://dx.doi.org/10.1016/S0967-0637\(01\)00046-2](http://dx.doi.org/10.1016/S0967-0637(01)00046-2).
- Takahashi**, N., & Miyagi, D. 2011. Effect of stress on iron loss of motor core. In: Electric Machines & Drives Conference (IEMDC), 2011 IEEE International. pp. 469-74. Niagara Falls, ON: IEEE. <http://dx.doi.org/10.1109/IEMDC.2011.5994642>.
- Tan**, C., Ding, K., Jin, B., Seyfried, W.E., Jr, & Chen, Y. 2012. Development of an in situ pH calibrator in deep sea environments. *IEEE-ASME T Mech.* 17(1):8-15. <http://dx.doi.org/10.1109/TMECH.2011.2168419>.
- Tan**, C.Y., Jin, B., Ding, K., Seyfried, W.E., Jr, & Chen, Y. 2010. A long-term in situ calibration system for chemistry analysis of seawater. *J Zhejiang Univ-Sc A.* 11(9):01-708. <http://dx.doi.org/10.1631/jzus.A0900643>.
- White**, F.M. 2011. Fluid Mechanics. New York: McGraw-Hill, 896 pp.
- White**, S.N., Kirkwood, W., Sherman, A., Brown, M., Henthorn, R., Salamy, K., ... Brewer, P.G. 2005. Development and deployment of a precision underwater positioning system for in situ laser Raman spectroscopy in the deep ocean. *Deep-Sea Res Pt I.* 52(12):2376-89. <http://dx.doi.org/10.1016/j.dsr.2005.09.002>.
- Zou**, J., Qi, W., Xu, Y., Xu, F., Li, Y., & Li, J. 2012. Design of deep sea oil-filled brushless DC motors considering the high pressure effect. *IEEE T Magn.* 48(11):4220-3. <http://dx.doi.org/10.1109/TMAG.2012.2204731>.

UPCOMING MTS JOURNAL ISSUES

May/June 2016

Impacts of Data Collected and Lessons Learned from Ocean Observing Systems Worldwide

Guest editors: Donna M. Kocak, Vembu Subramanian, Ian Walsh, Mairi Best, & Joshua Henson

July/August 2016

Research Initiatives in Europe: Cooperation for Blue Growth

Guest editors: Andrea Caiti, Giuseppe Casalino, & Andrea Trucco

September/October 2016

Bio-inspiration for Marine Technologies

Guest editor: Jason D. Geder

November/December 2016

Military Activities: Preserving the Legacy, Evaluating Threats and Mitigating Impacts

Guest editors: Geoff Carton & Lisa Symons

Manuscripts due June 20, 2016

CALL FOR PAPERS

The *MTS Journal* includes technical papers, notes and commentaries of general interest in most issues.

Contact Managing Editor

Amy Morgante

(morganteditorial@verizon.net)

if you have material you would like considered.

Specifications for submitting a manuscript are on the MTS website under the Publications menu.

www.mtsociety.org

E-mail:

morganteditorial@verizon.net

Or visit our homepage at

www.mtsociety.org



Opportunity runs deep™

Check the Society website for future *Journal* topics.
www.mtsociety.org

STATEMENT OF OWNERSHIP

Statement of Ownership, Management, and Circulation (Required by 39 U.S.C. 3685)

1. Publication Title: Marine Technology Society Journal
2. Publication Number: 0025-3324
3. Filing Date: 3/18/16
4. Issue Frequency: Bi-monthly
5. Number of Issues Published Annually: 6
6. Annual Subscription Price: \$155 Domestic; \$250 Foreign
- 7-8. Complete Mailing Address of Known Office of Publication and Headquarters or General Business Office of Publisher (Not printer): Marine Technology Society, 1100 H Street NW, LL-100, Washington, DC 20005
9. Publisher: Marine Technology Society, 1100 H Street NW, LL-100, Washington, DC 20005; Editor: Anni Vuorenkoski Dalgleish, MTS, 1100 H Street NW, LL-100, Washington, DC 20005; Managing Editor: Amy Morgante, 1100 H Street NW, LL-100, Washington, DC 20005
10. Owner: Marine Technology Society, 1100 H Street NW, LL-100, Washington, DC 20005
11. Known Bondholders, Mortgagees, and Other Security Holders Owning or Holding 1 Percent or More of Total Amount of Bonds, Mortgages, or Other Securities: None
12. Tax Status: Has Not Changed During Preceding 12 Months
13. Publication Title: Marine Technology Society Journal
14. Issue Date for Circulation Data Below: SEPT/OCT 2015

15. Extent and Nature of Circulation	Average No. Copies Each Issue During Preceding 12 Months	No. Copies of Single Issue Published Nearest to Filing Date	d. Free or Nominal Rate Distribution (By Mail and Outside the Mail)	
a. Total Number of Copies (Net Press Run)	500	480	1. Outside-country as Stated on Form 3541	0 0
b. Paid Circulation (By Mail and Outside the Mail)			2. In-Country as Stated on Form 3541	0 0
1. Mailed Outside-Country Paid Subscriptions Stated on PS Form 3541 (include paid distribution above normal rate, advertiser's proof copies, and exchange copies)	450	420	3. Other Classes Mailed Through the USPS	0 0
2. Mailed In-County Paid Subscriptions Stated On form 3541 (include advertiser's proof and exchange copies)	0	0	4. Free Distribution Outside the Mail	25 0
3. Sales Through Dealers and Carriers, Street Vendors, Counter Sales, and Other Non-USPS Distribution	0	0	e. Total Free or Nominal Rate Distribution (Sum of 15d)	25 15
4. Paid Distribution by Other Classes of Mail Through the USPS	50	10	f. Total Distribution (Sum of 15c and 15e)	525 445
c. Total Paid Distribution (sum of 15b, (1), (2), (3) and (4))	500	430	g. Copies not Distributed	25 35
			h. Total (sum of 15f and g)	550 480
			i. Percent Paid (15c divided by 15f times 100)	95.2% 96.6%
			16. Electronic Copy Circulation	
			a. Paid Electronic Copies	65 54
			b. Total Paid Print Copies (Line 15c) + Paid Electronic Copies (Line 16a)	565 484
			c. Total Print Distribution (Line 15f) + Paid Electronic Copies (Line 16a)	590 499
			d. Percent Paid (Both Print & Electronic Copies) (16b divided by 16c times 100)	95.7% 97.0%
			17. Publication Statement of Ownership will be printed in the Vol. 50, No. 2 issue of this publication, MAR/APRIL 2016.	
			I certify that 50% of all my distributed copies (electronic and print) are paid above a nominal price. I certify that the statements above made by me are correct and complete.	
				Amy Morgante

Marine Technology Society Membership Application and MTS Journal Subscription Request



- Yes, I want to become a member of the Marine Technology Society.
- I wish to purchase a subscription to the print version of the MTS Journal. (MTS Journal online is a free member benefit.)
- I'm not ready to join at the present time, but I would like to receive news and information from MTS. Please keep my name on your mailing list. (Please fill in member information section and return to MTS.)

MEMBER INFORMATION *(Please fill in the address where MTS publications and correspondence should be sent.)*

Name: _____ Company (if applicable): _____
Title: _____ Email: _____
Phone: _____ FAX: _____
Address: _____

MEMBERSHIP CATEGORIES

- MEMBER: \$75** Any person with active professional interest in the marine field or a closely related field. Includes the online version of the Journal.
- ASSOCIATE: \$75** Any person with an interest in the marine field and supporting MTS objectives. Includes the online version of the Journal.
- STUDENT: \$25** Must be a high school Senior, full-time undergraduate, or graduate student. Includes the online version of the Journal.
- PATRON:** Any person supporting MTS objectives by contributing \$100 or more annually. (Contribution above \$75 dues is tax deductible.) Includes the online version of the Journal.
- EMERITUS: \$40** Any person who is retired from active professional interest in the marine field. Includes the online version of the Journal.
- LIFE: \$1000** One-time payment. Includes both the online version of the Journal and the paper copy of the Journal.
- CORPORATE Fortune 500: \$2000** Any corporation endorsing the objectives, policies and activities of MTS. May appoint 16 representatives to the Society, who have the same rights and privileges as Members. Includes the online version of the Journal for each representative. The main contact receives a subscription to the paper copy of the Journal.
- CORPORATE Non-Fortune 500: \$1000** Any corporation endorsing the objectives, policies and activities of MTS. May appoint 11 representatives to the Society, who have the same rights and privileges as Members. Includes the online version of the Journal for each representative. The main contact receives a subscription to the paper copy of the Journal.
- BUSINESS: \$550** Any business firm whose gross annual income is less than \$4 million endorsing the objectives, policies and activities of MTS. May appoint six representatives to the Society, who have the same rights and privileges as Members. Includes the online version of the Journal for each representative. The main contact receives a subscription to the paper copy of the Journal.
- INSTITUTION: \$550** Any library, government unit or other qualified nonprofit organization endorsing the objectives, policies and activities of MTS. May appoint six representatives to the Society, who have the same rights and privileges as Members. Includes the online version of the Journal for each representative. The main contact receives a subscription to the paper copy of the Journal.

MTS JOURNAL PRINT VERSION SUBSCRIPTION *(Prices include shipping)*

Domestic Subscription

- Member Rate:\$38
- Non-Member Rate:\$155

Canadian/International Subscription

- Member Rate: \$55 Canadian/\$125 International
- Non-Member Rate: \$175 Canadian/\$250 International

NON-MEMBER AND LIBRARY SUBSCRIPTIONS TO MTS JOURNAL ONLINE

- Online only\$465
- Print and Online (worldwide)\$499

Marine Technology Society Membership Application (continued)

EDUCATIONAL INFORMATION

Please fill out the following information about yourself:

Check your highest level of education:

High School Diploma Associate (2 yr.) Degree Four Year Degree Graduate Degree Doctorate

Check all that apply: B.S. B.E. B.A. M.S. M.A. M.E. Ph.D. Sc.D.

Do you have a P.E. license? YES NO

BUSINESS/PROFESSIONAL INFORMATION

Name of current employer: _____

Your employer's primary line of business at your location: _____

If you don't work for an employer, please identify your business: _____

If military, rank: _____

Your principal job function/responsibilities:

Engineering Management
 Science Management
 Sales
 Marketing
 Administration
 Policy Making, Regulatory
 Public Affairs
 Engineering Design
 Mechanical Engineering
 Software Engineering
 Education/Teaching
 Legal
 Consulting
 Retired
 Other (please specify) _____

Your job title:

President/CEO/COO
 Owner/Partner
 VP, Senior Manager
 Project Manager,
Engineering
 Project Manager, Other
 Corporate VP, Engineering
 Engineering Director
 Chief/Senior Engineer
 Chief/Senior Scientist
 Project Manager
 Engineer
 Operations VP
 Scientist
 Other (please specify)

Check areas of interest:

Arctic Technology
 Buoy Technology
 Cables & Connectors
 Deepwater Field
Development
 Diving
 Dynamic Positioning
 Manned Underwater
Vehicles
 Marine Archaeology
 Marine Education
 Marine Geodetic
Information Systems
 Marine Law & Policy
 Marine Materials
 Marine Mineral Resources
 Marine Security
Moorings
 Ocean Economic Potential
 Ocean Exploration
 Ocean Observing Systems
 Ocean Pollution
 Oceanographic
Instrumentation
 Offshore Structures
 Physical Oceanography &
Meteorology
 Remote Sensing
 Remotely Operated Vehicles
 Renewable Energy
 Ropes & Tension Members
 Seafloor Engineering
 Underwater Imaging
 Unmanned Maritime
Vehicles
 Other (please specify)

Optional Information:

Male Female What is your age? Under 30 30-40 41-50 51-60 Over 60

MEMBERSHIP AND JOURNAL PAYMENT

Payment Method: Check Enclosed CK#_____ Master Card Visa Diners Club Am Ex

Make checks payable to the Marine Technology Society (U.S. funds only)

Card #: _____ Expiration Date: _____

CVV Number (Required): _____ (Visa, MasterCard and Discover Card — The three digit number is located to the right of the regular number on the back of the card. American Express Card — the four digit number is located on the front of the card in either the upper-left or upper-right side of the regular number.)

Signature: _____ Date: _____

TOTAL PAYMENT:

Membership: \$_____

Journal: \$_____

TOTAL: \$_____

Four easy ways to join!

Mail: Send application with check or credit card info to:
Marine Technology Society/1100 H Street NW, Suite LL-100/Washington, DC 20005

Fax: Fax application to: 202-347-4302 (credit card payments only)

Online: Apply online at www.mtsociety.org

Phone: Contact us at: 202-717-8705

Marine Technology Society Member Organizations

CORPORATE MEMBERS

ABCO Subsea, Houston, Texas
AMETEK Sea Connect Products, Inc., Westerly, Rhode Island
Bibby Subsea, Houston, Texas
BMT Scientific Marine Services Inc., Houston, Texas
C-MAR Group, Houston, Texas
Compass Publications, Inc., Arlington, Virginia
DeepSea Technologies, Inc., Houston, Texas
Deloitte & Touche, LLP, Houston, Texas
Delta SubSea, LLC, Montgomery, Texas
DNV GL, Houston, Texas
DOF Subsea USA, Inc., Houston, Texas
EMAS AMC, Houston, Texas
Fluor Offshore Solutions, Sugar Land, Texas
Forum Energy Technologies, Houston, Texas
Fugro Chance, Inc., Lafayette, Louisiana
Fugro Pelagos, Inc., San Diego, California
Fugro USA, Houston, Texas
Geospace Offshore Cables, Houston, Texas
GE Energy Power Conversion, Houston, Texas
Harris Corporation, Melbourne, Florida
Hydroid, LLC, Pocasset, Massachusetts
Innerspace Corporation, Covina, California
InterMoor, Inc., Houston, Texas
INTECSEA, Houston, Texas
Klein Marine Systems, Inc., Salem, New Hampshire
Kongsberg Maritime, Inc., Houston, Texas
L-3 MariPro, Goleta, California
Lockheed Martin Sippican, Marion, Massachusetts
MacArtney, Inc., Houston, Texas
Marine Cybernetics AS, Trondheim, Norway
Mitsui Engineering and Shipbuilding Co. Ltd., Tokyo, Japan
Oceaneering Advanced Technologies, Hanover, Maryland
Oceaneering International, Inc., Houston, Texas
OceanWorks International, Houston, Texas
Oil States Industries, Inc., Arlington, Texas
Phoenix International Holdings, Inc., Largo, Maryland
Quest Offshore Resources, Sugar Land, Texas
Saipem America Inc., Houston, Texas
SBM Offshore, Houston, Texas
Schilling Robotics, LLC, Davis, California
Schottel, Inc., Houma, Louisiana
SEACON, El Cajon, California
Sebastion AS, Ulsteinvik, Norway
SonTek/YSI Inc., San Diego, California
South Bay Cable Corp., Idyllwild, California
Southwest Electronic Energy Group, Stafford, Texas
Stress Engineering Services, Inc., Houston, Texas
Technip, Houston, Texas
Teledyne Marine Systems, North Falmouth, Massachusetts
Teledyne Oil & Gas, Daytona Beach, Florida
Teledyne RD Instruments, Inc., Poway, California
Universal Pegasus International, Houston, Texas
Vencore, Inc., Stennis Space Center, Mississippi
Wartsila Corporation, Houston, Texas
Whitefield Plastics, Houston, Texas
Wood Group Kenny, Inc., Houston, Texas
Wood Group Mustang, Houston, Texas

BUSINESS MEMBERS

Ashtead Technology Offshore, Inc., Houston, Texas
ASV, LLC, Broussard, Louisiana
Atlantis Deep Sea Ltd, Valleria, Malta
Baker Marine Solutions, Mandeville, Louisiana
Bastion Technologies, Inc., Houston, Texas
BioSonics, Inc., Seattle, Washington
Blade Offshore Services Ltd., Gosforth, Newcastle upon Tyne, UK
Braemar Engineering, Houston, Texas
CARIS, Alexandria, Virginia
C-LARs LLC, Bryan, Texas
DeepSea Power and Light, San Diego, California
Deepwater Rental and Supply, New Iberia, Louisiana
DPI Pte Ltd., Singapore
Energy Sales, Redmond, Washington
Falmat, Inc., San Marcos, California
GAMBiT Marine Solutions, Alexandria, Virginia
Global Marine Consultants and Surveyors, Ltd, Alexandria, West Dunbartonshire, UK
GMC Inc., Houston, Texas
GRI Simulations Inc., Mount Pearl, Newfoundland and Labrador, Canada
Horizon Marine, Inc., Marion, Massachusetts
INSPIRE Environmental, Newport, Rhode Island
Kongsberg Maritime Contros/Embient, Kiel, Germany
Laser Tools Co., Inc., Little Rock, Arkansas
Liquid Robotics, Sunnyvale, California
London Offshore Consultants, Inc., Houston, Texas
M3 Marine Expertise Pte Ltd., Singapore
Mactech Offshore, Inc., Broussard, Louisiana
Makai Ocean Engineering, Inc., Kailua, Hawaii
Maritime Assurance & Consulting Ltd., Aberdeen, United Kingdom
Mirage Subsea Inc., Houston, Texas
North Pacific Crane Company, Seattle, Washington
Offshore Analysis & Research Solutions (OARS), LLC, Austin, Texas
Poseidon Offshore Mining, Oslo, Norway
QPS, Portsmouth, New Hampshire
Remote Ocean Systems, Inc., San Diego, California
Rowe Technologies Inc., Poway, California
SeaLandAire Technologies, Inc., Jackson, Mississippi
Sonardyne, Inc., Houston, Texas
Soundnine, Inc., Redmond, WA
Sound Ocean Systems, Inc., Redmond, Washington
Stress Engineering Services, Inc., Houston, Texas
SURF Subsea, Inc., Magnolia, Texas
TALON Technical Sales, Inc., Houston, Texas
Technology Systems Corporation, Palm City, Florida
Teledyne SeaBotix, San Diego, California
Tension Member Technology, Huntington Beach, California
Triton Submarines LLC, Vero Beach, Florida
Ultra Deep, LLC, Houston, Texas
Unitech International, Houston, Texas
VideoRay, LLC, Pottstown, Pennsylvania

INSTITUTIONAL MEMBERS

City of St. John's, Newfoundland and Labrador, Canada
CLS America, Inc., Largo, Maryland
Consortium for Ocean Leadership, Washington, DC
Department of Business, Tourism, Culture and Rural Development, St. John's, Newfoundland and Labrador, Canada
Fundação Homem do Mar, Rio de Janeiro, Brazil
Harbor Branch Oceanographic Institute, Fort Pierce, Florida
International Seabed Authority, Kingston, Jamaica
Jeju Sea Grant Center, Jeju-City, South Korea
Marine Institute, Newfoundland and Labrador, Canada
Matthew Fontaine Maury Oceanographic Library, NAVOCEANO, Stennis Space Center, Mississippi
Monterey Bay Aquarium Research Institute, Moss Landing, California
Metanomy, Inc, 501(c)(3), Saint Petersburg, Florida
NOAA/PMEL, Seattle, Washington
OceanGate, Inc., Everett, Washington
Oregon State University College of Oceanic and Atmospheric Sciences, Corvallis, Oregon
Schmidt Ocean Institute, Lake Forest Park, Washington
Stockton University, Port Republic, New Jersey
University of Massachusetts–Dartmouth, New Bedford, Massachusetts

marine technology SOCIETY
1100 H Street NW, Suite LL-100
Washington, DC 20005

Postage for periodicals
is paid at Washington, DC
and additional mailing offices.

